

THREE-DIMENSIONAL COMPRESSIBLE LAMINAR BOUNDARY LAYERS
ON SHARP AND BLUNT CIRCULAR CONES AT ANGLE OF ATTACK

Final Report on Contract NAS1-11104
NASA Langley Research Center
Hampton, Virginia

**CASE FILE
COPY**

Prepared by
Zenon Popinski, Graduate Research Assistant
and
R.T. Davis, Professor and Head
Department of Aerospace Engineering
University of Cincinnati
Cincinnati, Ohio 45221

January 1973

ACKNOWLEDGEMENT

The authors wish to express thanks to Dr. Julius Harris of Langley Research Center for providing the inviscid data for the computations contained herein and also for his advice in many aspects of the computations.

ABSTRACT

A method for solving the three-dimensional compressible laminar boundary-layer equations for the case of a circular cone and a sphere-cone body at an angle of attack is presented. The governing equations are modified by a similarity type transformation and then transformed into a Crocco-type form. The resulting set of equations is solved simultaneously by an iterative method using an implicit finite difference scheme by means of an efficient algorithm for equations of tridiagonal form.

The effects of streamline swallowing on a sharp cone are included by introducing the true inviscid edge-conditions at the distance from the wall equal to the boundary-layer thickness. The validity of the approach was established by comparison of the computational results with similar results by other methods and with experimental data.

It was concluded that at sufficiently high Mach number and moderate to large angles of attack, the streamline swallowing effects on a sharp cone result in higher values of skin friction and heat transfer as compared with the classical results for constant entropy.

TABLE OF CONTENTS

	<u>Page</u>
LIST OF TABLES AND FIGURES.....	vi
NOMENCLATURE.....	ix
1. INTRODUCTION.....	1
2. THREE-DIMENSIONAL COMPRESSIBLE LAMINAR BOUNDARY-LAYER EQUATIONS.....	5
3. NUMERICAL METHOD OF SOLUTION.....	14
3.1 General Solution Technique.....	23
4. SOLUTIONS FOR SHARP CIRCULAR CONES AT ANGLE OF ATTACK WITH STREAMLINE SWALLOWING.....	25
4.1 The Geometry of the Problem.....	25
4.2 Conditions at the Outer Edge of the Boundary Layer.....	26
4.3 Non-Isentropic Conditions.....	27
4.4 Boundary Layer Thickness.....	28
4.5 Location of the Edge of the Boundary- Layer.....	29
4.6 Inviscid Data.....	30
4.7 Limitations of the Inviscid Flow Methods.	36
4.8 Difficulties at the Leeward Plane.....	38
4.9 Solution to the Problem.....	40
4.10 Results.....	41
4.11 Conclusions.....	47
5. SOLUTIONS FOR BLUNTED CONES AT ANGLE OF ATTACK.	49
5.1 The Geometry of the Problem.....	49
5.2 Flow About a Sphere-Cone.....	50
5.3 Method of Solution.....	52

	<u>Page</u>
5.4 Inviscid Data.....	53
5.5 Results.....	55
5.6 Conclusions.....	56
REFERENCES.....	58
APPENDIX A.....	A1
Coefficients A_i and B_i	A1
APPENDIX B.....	B1
B.1 Double Interpolation Subroutine.....	B1
B.2 Cubic Spline Subroutine.....	B2
APPENDIX C.....	C1
C.1 Conditions for Similarity at a Stagnation Point.....	C1
APPENDIX D.....	D1
D.1 Input and Output Quantities for the Computer Programs.....	D1
D.2 Input Quantities.....	D1
D.3 Output Quantities.....	D6
APPENDIX E.....	E1
Computer Program for a Sharp Circular Cone with Entropy Swallowing.....	E1
APPENDIX F.....	F1
Computer Program for a Blunted Circular Cone - Region I.....	F1
APPENDIX G.....	G1
Computer Program for a Blunted Circular Cone - Regions II-III.....	G1

LIST OF TABLES AND FIGURES

Table	Page
I Conditions of Computed Sharp Cone Cases.....	61
II Computed Sharp Cone Parameters at $\alpha = 0^\circ$	62

Figure	Page
1.1 Streamline Pattern About a Sharp Circular Cone.....	63
1.2 Streamline Swallowing on a Sphere-Cone at Zero Angle of Attack.....	64
1.3 Streamline Swallowing on a Sharp Cone at Angle of Attack.....	65
2.1 Coordinate System.....	66
3.1a Finite-Difference Scheme Used in the General Case.....	67
3.1b Finite-Difference Scheme Used in the Case of Similarity in the ξ -Direction.....	68
3.2 Integration Technique for Three-Dimensional Boundary-Layers.....	69
4.1 Geometry of the Circular Cone.....	70
4.2 Coordinate System for Conical Flow.....	71
4.3 Shock-Body Geometry for a Cone.....	72
4.4 Flow Variables for a Sharp Circular Cone for $M_\infty = 8$, $\phi_c = 10^\circ$, $\alpha = 12^\circ$	73
4.5 Comparison of Pressure Distribution on 10° Sharp Cone by Various Methods, $\alpha = 8^\circ$	74
4.6 Skin Friction Distribution on a Sharp Circular Cone.....	75
4.7 Heat Transfer Distribution on a Sharp Circular Cone.....	76

Figure		Page
4.8	Skin Friction Distribution on a Sharp Circular Cone.....	77
4.9	Heat Transfer Distribution on a Sharp Circular Cone.....	78
4.10	Skin Friction Distribution on a Sharp Circular Cone.....	79
4.11	Heat Transfer Distribution on a Sharp Circular Cone.....	80
4.12	Skin Friction Distribution on a Sharp Circular Cone.....	81
4.13	Heat Transfer Distribution on a Sharp Circular Cone.....	82
4.14	Heat Transfer Distribution on a Sharp Circular Cone.....	83
4.15	Skin Friction Distribution on a Sharp Circular Cone.....	84
4.16	Skin Friction Distribution on a Sharp Circular Cone.....	85
4.17	Heat Transfer Distribution on a Sharp Circular Cone.....	86
4.18	Heat Transfer Distribution on 10° Sharp Circular Cone at $\alpha = 8^\circ$	87
4.19	Heat Transfer Distribution on 10° Sharp Circular Cone at $\alpha = 12^\circ$	88
4.20	Circumferential Boundary-Layer Thickness Distribution on a Sharp Circular Cone.....	89
4.21	Streamwise Variation of the Boundary-Layer Thickness on a Sharp Circular Cone.....	90
4.22	Circumferential Entropy Distribution on a Sharp Circular Cone for the Case of Entropy Swallowing at a distance σ	91
4.23	Convergence of Computed Parameters After Transfer to Entropy Swallowing Scheme on a Sharp Circular Cone.....	92

Figure		Page
4.24	Circumferential Error Distribution Between Results from 2nd and 1st Sweep for a Sharp Circular Cone.....	93
5.1	Sphere-Cone Geometry.....	94
5.2	Spherical Coordinate System.....	95
5.3	Geometry for Regions I and II for a Sphere....	96
5.4	Geometrical Relations for a Sphere in Wind and Body Systems.....	97
5.5	Geometry for Inviscid Data Input for Region I and II for Sphere.....	98
5.6	Skin Friction, Heat Transfer and Flow Variables About a Sphere.....	99
5.7	Longitudinal Skin Friction Distribution in Meridian Planes for a Sphere Cone.....	100
5.8	Longitudinal Heat Transfer Distribution in Meridian Planes for a Sphere Cone.....	101
5.9	Skin Friction and Heat Transfer Distribution on a Sphere-Cone.....	102
5.10	Longitudinal Pressure and Velocity Distribution in Meridian Planes.....	103
5.11	Longitudinal Pressure Derivatives in Meridian Planes for a Sphere Cone.....	104
5.12	Longitudinal Velocity Derivative in Meridian Planes for a Sphere Cone.....	105
5.13	Circumferential Distribution of p_e , u , v and $\frac{\partial p_e}{\partial \eta}$, $\frac{\partial u}{\partial \eta}$ on a Sphere Cone.....	106

NOMENCLATURE

$\Lambda_1 - \Lambda_{19}$	Coefficients used in (2.18) through (2.21) defined by (A1) through (A19).
A'_n, B'_n, C'_n, D'_n	Coefficients in difference equation (3.09) defined by (3.10) through (3.13), (3.20) through (3.23), or (3.26) through (3.29).
$B_1 - B_{14}$	Coefficients in the governing equations (2.23) through (2.25) defined by (A20) through (A33).
C	Constant in Sutherland's viscosity law as stated in (2.26).
\bar{C}_v, \bar{C}_p	Specific heat at constant volume and constant pressure, respectively.
C_p	Dimensionless specific heat at constant pressure non-dimensionalized by $C_p = \frac{\bar{C}_p}{R}$.
C_{f_ξ}	Longitudinal skin friction coefficient defined by $C_{f_\xi} = \frac{\tau_{w\xi}}{\frac{1}{2} \rho_\infty \bar{u}_\infty^2}.$

C_{f_n}	Transverse skin friction coefficient defined by
	$C_{f_n} = \frac{\tau_{w_n}}{\frac{1}{2} \rho_\infty \bar{u}_\infty^2} .$
E'_n, F'_n	Coefficients in the recursion relation (3.30) defined by (3.31) and (3.32), respectively.
F	Non-dimensional longitudinal velocity as defined by (2.09).
G	Non-dimensional transverse velocity as defined by (2.10).
H	Non-dimensional normal velocity as defined by (2.12).
h_1, h_2	Surface scale factors in the \bar{s}_1 and \bar{s}_2 directions, respectively; non-dimensionalized by $h_1 = \frac{\bar{h}_1}{\bar{L}}$, $h_2 = \frac{\bar{h}_2}{\bar{L}}$.
h	Enthalpy
h_3	Transformed normal scale factor in the \bar{s}_3 direction as defined in (2.07).
K	Constant used in the pressure-density relation (4.24).
\bar{k}	Thermal conductivity.
\bar{L}	Reference length.

μ	Non-dimensional viscosity defined by (2.13).
s	Arc length as defined by (4.02) and (5.02).
M_∞	Free-stream Mach Number.
Pr	Prandtl Number defined to be $Pr = \frac{\bar{\mu} \bar{C}_p}{\bar{k}}$
p	Dimensionless pressure non-dimensionalized by $p = \frac{\bar{p}}{\bar{\rho}_\infty \bar{u}_\infty^2}$.
q	Dimensionless heat-transfer rate defined in (2.35) non-dimensionalized by $q = \frac{\bar{q}}{\bar{\rho}_\infty \bar{u}_\infty^3}$.
R	Gas constant.
Re	Reference Reynolds Number as defined by $Re = \frac{\bar{\rho}_\infty \bar{u}_\infty \bar{L}}{\bar{\mu}_r}$.
Re_x	Reynolds Number defined by $Re_x = \frac{\bar{\rho}_\infty \bar{u}_\infty \bar{L}}{\bar{\mu}_\infty}$
r	Distance measured from the origin of the r, θ, ϕ coordinate system as shown in Figure 4.1 non-dimensionalized by $r = \frac{\bar{r}}{\bar{L}}$

s	Entropy
$\bar{s}_1, \bar{s}_2, \bar{s}_3$	Arc lengths in the ξ, η, ζ direction, respectively.
t	Dimensionless temperature non-dimensionalized by $t = \frac{\bar{t}}{\bar{u}_\infty^2/R}$.
T	Absolute temperature.
\bar{t}_r	Reference temperature defined by $\bar{t}_r = \frac{\bar{u}_\infty^2}{R}$.
\bar{u}_∞	Free-stream velocity.
u	Longitudinal velocity component (in ξ -direction) non-dimensionalized by $u = \frac{\bar{u}}{\bar{u}_\infty}$.
v	Specific volume.
v	Transverse velocity component (in η -direction) non-dimensionalized by $v = \frac{\bar{v}}{\bar{u}_\infty}$.
w	Normal velocity component (in ζ -direction) defined by (2.08).
x, y, z	Cartesian coordinates as shown in Figure 4.1 and 4.2.
α	Angle of attack as shown in Figures 2.1, 4.1 and 4.2.

$\alpha'_{1n}, \alpha'_{2n}, \alpha'_{3n}, \alpha'_{4n}, \alpha'_{5n}$	Coefficients in (3.08).
γ	Ratio of specific heats defined to be $= \frac{\bar{c}_p}{\bar{c}_v}$.
$\bar{\delta}$	Boundary-layer thickness.
ζ	Normal coordinate as shown in Figure 2.1.
η	Surface coordinate as shown in Figure 2.1.
θ	Non-dimensional temperature as defined by (2.11).
θ	Spherical coordinate system angle as shown in Figure 4.1.
μ	Viscosity defined by (2.06) and non-dimensionalized by $\mu = \frac{\bar{\mu}}{\bar{\mu}_r}$.
$\bar{\mu}_r$	Viscosity evaluated at the reference temperature, \bar{t}_r .
ξ	Surface coordinate as shown in Figure 2.1.
ξ^*	Scaling function in (2.07) and (2.08).
$\bar{\xi}$	Parameter describing a conical ray in shock layer (Fig. 4.3).

$\bar{\rho}_\infty$	Free-stream density.
ρ	Dimensionless density non-dimensionalized by $= \frac{\bar{\rho}}{\bar{\rho}_\infty}$.
τ_{w_ξ}	Longitudinal wall shear stress component (in ξ -direction).
τ_{w_η}	Transverse wall shear stress component (in η -direction).
ϕ	Spherical coordinate system angle as shown in Figure 4.1.
ϕ	Shear parameter defined in (2.17).
ω	Variable used to represent alternately ϕ , G , or θ in (3.08).
$\Delta\xi$	Step size in the longitudinal (ξ) direction.
$\Delta\eta$	Step size in the transverse (η) direction.
$\Delta\zeta$	Step size in the normal (ζ) direction.

Subscripts

e	Inviscid condition at the body surface.
w	Conditions at the body surface.

- o Stagnation conditions.
- ∞ Free-stream conditions.

Superscripts

- Dimensional quantity.

1. INTRODUCTION

The Navier Stokes equations of motion which describe compressible viscous fluid flow past a body are highly non-linear and present formidable obstacles to classical analytical or numerical methods of solution except in special cases. However, since at high Reynolds number the effects of fluid viscosity are confined to a thin layer near the body surface, many terms in the full equations can be neglected by making the boundary-layer approximation. The resulting equations can be solved numerically for specified boundary conditions at the wall and at the edge of the boundary-layer for prescribed external inviscid fluid properties. This is possible since the boundary-layer equations are parabolic whereas, the original Navier Stokes equations are elliptic. Parabolic equations are in general easy to solve numerically whereas, elliptic equations are not.

In order to solve the boundary-layer equations, external inviscid properties are needed. The usual assumption for the external flow at the body surface for supersonic flow is that it is of constant entropy corresponding to either the oblique shock entropy or stagnation streamline entropy. However, as the boundary-layer thickens in the streamwise and cross-flow directions in three-dimensional flow, streamlines of variable entropy are entrained into the boundary-layer and the isentropic condition, especially for a body at an angle of attack, does not hold.

One objective of this study is to develop a method to

account for the effect of the variable entropy layer near the surface of a body at angle of attack on the solutions for laminar three-dimensional viscous flows as compared with the classical solutions for viscous flow which have been based on constant entropy surface conditions. It is interesting to note that despite a large body of literature related to three-dimensional boundary layers, this particular area has remained relatively unexplored.

The literature reviews by Cooke and Hall (ref. 1), Mager (ref. 2) and Stewartson (ref. 3) reflect the major extent of work done in the area of three-dimensional boundary-layers. A case which has received considerable attention, because of simplifications due to spanwise derivatives being zero, is conical flow. The majority of the work done on viscous conical flows has been concerned with approximate methods of solution which are usually valid for small cross-flow and small angle of attack. Only recently the restriction of small cross-flow has been removed in work for sharp circular cones by Boericke (ref. 4), McGowan and Davis (ref. 5), and others. In conical flows the boundary-layer solution is actually two-dimensional since similarity exists in the streamwise direction. The flow near the windward side creates no problems and is dominated by inviscid conical flow with a favorable pressure gradient. The region near the leeward plane at high angles of attack may be strongly influenced by inviscid viscous interactions. There is flow turning toward the windward plane of symmetry which may give rise to imbedded shocks if the local

Mach number in the cross-flow plane is supersonic. This may cause separation. The presence of an adverse pressure gradient can cause the cross-flow velocity to reverse and cause the flow to recirculate. Typically, the flow in this region even at moderate angles of attack, exhibits a bump with streamlines diverging as they approach the leeside of the body, (Fig. 1.1).

A cone at angle of attack is characterized by the fact that the streamlines around the periphery of the cone are passing through a shock of varying strength and possess different entropies. The surface streamlines pass through the windward meridian plane and have the highest value of entropy. The streamlines away from the windward plane pass through a weaker shock and possess lower values of entropy and enter the flow field nearly meridionally. There is a layer near the surface in which the entropy varies rapidly with the distance from the surface, from the maximum value, to a lower value consistent with a weaker shock. Thus, although the entropy at the surface is constant, the entropy of the streamlines entrained by the boundary-layer is of varying magnitude. The question of the magnitude of the effect of the variable entropy on the viscous boundary-layer flow has been of considerable concern and importance. This problem also occurs on a blunted body at zero angle of attack with a bow shock which is normal for the stagnation streamline wetting the surface. The streamlines passing through an oblique shock have lower entropy as they are "swallowed" by the boundary-layer downstream,

(Fig. 1.2). The same phenomenon occurs on a sharp cone at angle of attack (Fig. 1.3) where the streamlines away from windward plane enter the boundary-layer with lower entropy and create a thin vorticity layer. Of course, outer edge boundary conditions accounting for streamline swallowing will yield results different from the classical approach using edge conditions of constant state as was concluded by Ferri (ref. 6) and Mayne and Adams (ref. 7). A more proper approach to account for swallowing of a streamline as it enters the boundary-layer, would be to use the edge conditions consistent with the flow conditions at the distance from the surface equal to the boundary-layer thickness.

In order to establish the extent of the influence of the streamline swallowing upon the boundary-layer, a method for accounting for the effects of vorticity swallowing has been developed. The objective of the technique presented here is to determine the effects of the variable entropy edge conditions on solutions to the three-dimensional boundary-layer equations for supersonic flow over a right circular cone at angle of attack. The second part of this work is devoted to the solution of viscous laminar flows over blunted cones.

The governing boundary-layer equations will be first modified by a similarity type transformation and then transformed into a Crocco-type form. The resulting equations will then be solved simultaneously by an iterative method using an implicit finite difference scheme similar to one developed by Dwyer (ref. 8) with modifications by Kraus (ref. 9).

2. THREE-DIMENSIONAL COMPRESSIBLE LAMINAR BOUNDARY-LAYER EQUATIONS*

An implicit finite-difference technique originally developed by McGowan and Davis (ref. 5) will be employed for solving the three-dimensional compressible laminar boundary-layer equations over sharp and blunt right circular cones. The governing equations for a generalized body-oriented coordinate system to be used in the analysis (see Fig. 2.1) are as follows:

ξ - momentum

$$\begin{aligned} \frac{\bar{u}}{\bar{h}_1} \frac{\partial \bar{u}}{\partial \xi} + \frac{\bar{v}}{\bar{h}_2} \frac{\partial \bar{u}}{\partial \eta} + \frac{\bar{w}}{\bar{h}_3} \frac{\partial \bar{u}}{\partial \zeta} + \frac{\bar{u}\bar{v}}{\bar{h}_1\bar{h}_2} \frac{\partial \bar{h}_1}{\partial \eta} - \frac{\bar{v}^2}{\bar{h}_1\bar{h}_2} \frac{\partial \bar{h}_2}{\partial \xi} \\ = - \frac{1}{\bar{\rho}\bar{h}_1} \frac{\partial \bar{p}}{\partial \xi} + \frac{1}{\bar{\rho}\bar{h}_3} \frac{\partial}{\partial \zeta} \left[\frac{\bar{\mu}}{\bar{h}_3} \frac{\partial \bar{u}}{\partial \zeta} \right] , \end{aligned} \quad (2.01)$$

η - momentum

$$\begin{aligned} \frac{\bar{u}}{\bar{h}_1} \frac{\partial \bar{v}}{\partial \xi} + \frac{\bar{v}}{\bar{h}_2} \frac{\partial \bar{v}}{\partial \eta} + \frac{\bar{w}}{\bar{h}_3} \frac{\partial \bar{v}}{\partial \zeta} - \frac{\bar{u}^2}{\bar{h}_1\bar{h}_2} \frac{\partial \bar{h}_1}{\partial \eta} + \frac{\bar{u}\bar{v}}{\bar{h}_1\bar{h}_2} \frac{\partial \bar{h}_2}{\partial \xi} \\ = - \frac{1}{\bar{\rho}\bar{h}_2} \frac{\partial \bar{p}}{\partial \eta} + \frac{1}{\bar{\rho}\bar{h}_3} \frac{\partial}{\partial \zeta} \left[\frac{\bar{\mu}}{\bar{h}_3} \frac{\partial \bar{v}}{\partial \zeta} \right] , \end{aligned} \quad (2.02)$$

* Detailed presentation of the equations and transformations discussed in this section is given by McGowan and Davis (ref. 5) and Der (ref. 10).

energy

$$\begin{aligned} \frac{\bar{u}}{\bar{h}_1} \frac{\partial \bar{t}}{\partial \xi} + \frac{\bar{v}}{\bar{h}_2} \frac{\partial \bar{t}}{\partial \eta} + \frac{\bar{w}}{\bar{h}_3} \frac{\partial \bar{t}}{\partial \zeta} = \frac{1}{\bar{c}_{p\rho}} \left[\frac{\bar{u}}{\bar{h}_1} \frac{\partial \bar{p}}{\partial \xi} + \frac{\bar{v}}{\bar{h}_2} \frac{\partial \bar{p}}{\partial \eta} \right] \quad (2.03) \\ + \frac{\bar{\mu}}{\bar{c}_{p\rho} \bar{h}_3^2} \left[\left[\frac{\partial \bar{u}}{\partial \zeta} \right]^2 + \left[\frac{\partial \bar{v}}{\partial \zeta} \right]^2 \right] + \frac{1}{\bar{c}_{p\rho} \bar{h}_3} \frac{\partial}{\partial \zeta} \left[\frac{\bar{k}}{\bar{h}_3} \frac{\partial \bar{t}}{\partial \zeta} \right] , \end{aligned}$$

continuity

$$\frac{\partial}{\partial \xi} (\bar{h}_2 \bar{h}_3 \bar{\rho} \bar{u}) + \frac{\partial}{\partial \eta} (\bar{h}_1 \bar{h}_3 \bar{\rho} \bar{v}) + \frac{\partial}{\partial \zeta} (\bar{h}_1 \bar{h}_2 \bar{\rho} \bar{w}) = 0 \quad , \quad (2.04)$$

state

$$\bar{p} = R \bar{\rho} \bar{t} \quad , \quad (2.05)$$

and

viscosity (Sutherland)

$$\frac{\bar{\mu}}{\bar{\mu}_r} = \frac{\bar{t}_r + C \left[\frac{\bar{t}}{\bar{t}_r} \right]^{3/2}}{\bar{t} + C \left[\frac{\bar{t}}{\bar{t}_r} \right]} \quad (2.06)$$

where $C = 198.6^\circ R$ for air.

The ξ -coordinate is chosen to be the arc length along the body; therefore, \bar{h}_1 will be a constant, \bar{L} . \bar{h}_2 and \bar{h}_3 are chosen to be arbitrary functions of the coordinates. ξ , η , and ζ are dimensionless, consequently the scale factors h_1 ,

h_2 and h_3 have the dimensions of length. Similarity-type transformations for the normal coordinate and velocity are defined as follows:

$$\bar{h}_3 = \xi^* \frac{\bar{\rho}_e}{\bar{\rho}} \frac{\bar{L}}{\sqrt{Re}} h_3 \quad (2.07)$$

and

$$\bar{w} = \frac{1}{\xi^*} \frac{\bar{\rho}_e}{\bar{\rho}} \frac{\bar{u}_\infty}{\sqrt{Re}} w \quad (2.08)$$

where ξ^* is an arbitrary function of ξ and η and will be chosen such that similarity conditions are satisfied. For convenience the following definitions are made:

$$F = \frac{u}{u_e}, \quad G = \frac{v}{v_e}, \quad \theta = \frac{t}{t_e}, \quad H = \frac{w}{u_e} \text{ and } \lambda = \frac{\mu}{t}. \quad (2.09-2.13)$$

The equation of state in the dimensionless variables is written as:

$$\rho = p_e/t \quad (2.14)$$

The scale factors h_2 and h_3 are defined such that the equations will be in a Crocco-type form. The dimensionless scale factor h_2 is a function of ξ and η ; that is

$$h_2 = h_2(\xi, \eta) \quad (2.15)$$

The normal coordinate ζ is defined as

$$\zeta = \sqrt{1 - F} \quad (2.16)$$

and finally we choose the shear parameter ϕ to replace F as a dependent variables as

$$\phi = \frac{\ell}{2\zeta} \frac{1}{h_3} \frac{\partial F}{\partial \zeta} = - \frac{\ell}{h_3} \quad (2.17)$$

Equations (2.09) to (2.17) are next substituted into the governing equations (equations (2.01) to (2.04)). These variables are similar to those used by Der (ref. 10). The main advantage of these variables is that in the numerical calculations the integration is always carried out between $\zeta = 0$ (freestream) to $\zeta = 1$ (wall boundary). Thus use of a specified finite region in the ζ -direction can save large amounts of computer time over other variables which extend over an infinite region. This is important in three dimensional boundary-layer calculations where computing times can become excessive.

The governing equations (equations (2.01) to (2.04)) can

then be expressed in terms of Crocco-type variables as follows:

$$A_4 (1-\zeta^2)^2 + A_5 (1-\zeta^2)G + A_3 \frac{\zeta \phi H}{\ell} - A_6 G^2 = -A_7 \theta - \frac{\phi}{\ell} \frac{\partial}{\partial \zeta} (\phi \zeta) , \quad (2.18)$$

$$A_1 (1-\zeta^2) \frac{\partial G}{\partial \xi} + A_2 G \frac{\partial G}{\partial \eta} - A_3 \frac{\phi H}{\ell} \frac{\partial G}{\partial \zeta} + A_8 (1-\zeta^2)G + A_9 G^2 = -A_{10} \theta + \frac{\phi}{\ell} \frac{\partial}{\partial \zeta} (\phi \frac{\partial G}{\partial \zeta}) , \quad (2.19)$$

$$A_1 (1-\zeta^2) \frac{\partial \theta}{\partial \xi} + A_2 G \frac{\partial \theta}{\partial \eta} - A_3 \frac{\phi H}{\ell} \frac{\partial \theta}{\partial \zeta} = [A_{11} - A_{18}] (1-\zeta^2) \theta + [A_{12} - A_{19}] G \theta + [A_{13} \zeta^2 + A_{14} (\frac{\partial G}{\partial \zeta})^2] \frac{\phi^2}{\ell} + \frac{1}{Pr} \frac{\phi}{\ell} \frac{\partial}{\partial \zeta} (\phi \frac{\partial \theta}{\partial \zeta}) \quad (2.20)$$

and

$$A_1 (1-\zeta^2) \frac{\partial}{\partial \xi} (\frac{\ell}{\phi}) + A_2 \frac{\partial}{\partial \eta} (\frac{\ell G}{\phi}) - A_3 \frac{\partial H}{\partial \zeta} + (4A_4 + A_{15}) (1-\zeta^2) \frac{\ell}{\phi} + (2A_{17} + A_{16}) \frac{\ell G}{\phi} = 0. \quad (2.21)$$

The coefficients A_1, A_2, \dots, A_{19} are functions of the inviscid quantities and body geometry and are defined in Appendix A by equations A1 to A19. In order to reduce the system to three governing equations, equation (2.18) is solved for H as follows:

$$H = \frac{A_6 G^2 \ell}{A_3 \zeta \phi} - \frac{A_5 G (1-\zeta^2) \ell}{A_3 \zeta \phi} - \frac{A_4 (1-\zeta^2)^2 \ell}{A_3 \zeta \phi} - \frac{A_7 \theta \ell}{A_3 \zeta \phi} \quad (2.22)$$

$$- \frac{1}{A_3 \zeta} \frac{\partial}{\partial \zeta} (\phi \zeta) \quad .$$

Substituting equation (2.22) into equations (2.19) to (2.21) leads to the final form of the three governing equations for the dependent variables G , θ , and ϕ :

$$\frac{\partial^2 G}{\partial \zeta^2} + (B_1 - \frac{1}{\zeta}) \frac{\partial G}{\partial \zeta} + B_2 G + B_3 + B_4 \frac{\partial G}{\partial \xi} + B_5 \frac{\partial G}{\partial \eta} = 0 \quad , \quad (2.23)$$

$$\frac{\partial^2 \theta}{\partial \zeta^2} + [\frac{(1-Pr)}{\phi} \frac{\partial \phi}{\partial \zeta} - \frac{Pr}{\zeta} + B_6] \frac{\partial \theta}{\partial \zeta} + B_7 \theta + B_8 + B_9 \frac{\partial \theta}{\partial \xi}$$

$$+ B_{10} \frac{\partial \theta}{\partial \eta} = 0 \quad , \quad (2.24)$$

and

$$\frac{\partial^2 \phi}{\partial \zeta^2} + (\frac{1}{\zeta} + \frac{B_{11}}{\phi^2}) \frac{\partial \phi}{\partial \zeta} - \frac{\phi}{\zeta^2} + \frac{B_{12}}{\phi} + \frac{B_{13}}{\phi^2} \frac{\partial \phi}{\partial \xi} + \frac{B_{14}}{\phi^2} \frac{\partial \phi}{\partial \eta} = 0 \quad ;$$

$$(2.25)$$

where B_1, B_2, \dots, B_{14} are defined in Appendix A by equations A20 to A33.

The viscosity function appearing in the B_i coefficients (see equations (A20) to (A33)) is given by Sutherland's law as

$$\ell = \frac{1 + C/\bar{t}_r}{\theta + C/\bar{t}_e} \left[\frac{\theta}{\bar{t}_e} \right]^{1/2} = \frac{\mu}{\bar{t}} \quad (2.26)$$

The quantity $\partial \ell / \partial t$ (see equation (A31)) is obtained by differentiating equation (2.26) with respect to t ; that is,

$$\frac{\partial \ell}{\partial t} = \frac{\partial \ell}{\partial \theta} \frac{\partial \theta}{\partial t}.$$

The boundary conditions on G and θ at the body surface are:

$$G = 0 \quad (2.27)$$

and

$$\theta = \frac{t_w}{t_e}, \quad \text{at } \zeta = 1 \quad (2.28)$$

or

$$\frac{\partial \theta}{\partial \zeta} = f(\xi, \eta) \quad (2.29)$$

where $f(\xi, \eta)$ is related to some specified body surface heat transfer, and t_w is some specified body surface temperature.

At the outer edge of the boundary-layer the boundary conditions on G and θ are:

$$\left. \begin{array}{l} G = 1 \\ \theta = 1 \end{array} \right\} \quad \text{at } \zeta = 0 \quad (2.30)$$

and

$$\left. \begin{array}{l} G = 1 \\ \theta = 1 \end{array} \right\} \quad (2.31)$$

The boundary conditions on ϕ are more complicated. Applying L'Hospital's rule to (2.17) evaluated at the outer edge of the boundary-layer yields:

$$\phi \Big|_{\zeta=0} = \frac{\lambda}{2h_e} \frac{\partial^2 F}{\partial \zeta^2} \Big|_{\zeta=0}. \quad (2.32)$$

The quantity $\frac{\partial^2 F}{\partial \zeta^2}$ must vanish at the inviscid edge; therefore, at $\zeta = 0$

$$\phi \Big|_0 = 0 \quad (2.33)$$

The boundary condition on ϕ at the wall can be derived from (2.18) applied at the wall. Setting $\zeta = 1$ and using the no slip conditions result in:

$$\left[\frac{\partial \phi}{\partial \zeta} \right]_w = (- A_3 H - A_7 \frac{2\theta}{\phi} - \phi)_w \quad (2.34)$$

The nondimensional heat-transfer rate can be shown to be:

$$q = \frac{\bar{q}}{\bar{\rho}_\infty \bar{u}_\infty^3} = \left(\frac{\gamma}{\gamma-1} \right) \frac{t_e^2}{P_{r\xi}^* \sqrt{Re}} \left(\phi \frac{\partial \theta}{\partial \zeta} \right)_w \quad (2.35)$$

Also the skin friction coefficients can be shown to be:

$$C_{f_\xi} = \frac{\bar{\mu}}{\bar{h}_3} \left[\frac{\partial \bar{u}}{\partial \zeta} \right]_w \Big/ \frac{1}{2} \bar{\rho}_\infty \bar{u}_\infty^2 = \frac{4 t_e \phi_w u_e}{\xi^* \sqrt{Re}} \quad (2.36)$$

and

$$C_{f_\eta} = \frac{\bar{\mu}}{\bar{h}_3} \left[\frac{\partial \bar{v}}{\partial \zeta} \right]_w \Big/ \frac{1}{2} \bar{\rho}_\infty \bar{u}_\infty^2 = - \frac{2 t_e \phi_w v_e}{\xi^* \sqrt{Re}} \left(\frac{\partial G}{\partial \zeta} \right)_w \quad (2.37)$$

Finally, the physical normal distance can be expressed as:

$$\bar{s}_3 = - \int_{\zeta}^1 \frac{\ell}{\phi} \xi^* \theta d\zeta \frac{\bar{L}}{\sqrt{Re}} . \quad (2.38)$$

The governing equations and boundary conditions are now in a convenient form for solution using numerical methods. The next section will deal with developing an implicit finite difference method of solution.

3. NUMERICAL METHOD OF SOLUTION

The governing equations presented in Section 2 will now be reduced to finite-difference form in order that they may be solved numerically. The complete solution to be obtained on a digital computer will be comprised of three separate cases: a general scheme, a scheme in which similarity exists in one of the surface variables, and a scheme in which similarity exists in both surface variables. Finally, the complete computation scheme will be explained as a combination of the three separate cases. This development is identical to that presented in reference 5.

The governing equations are solved using a step-by-step finite-difference method similar to that suggested by Dwyer (ref. 8) with modifications by Krause (ref. 9). The method has accuracy of order Δ^2 , where Δ is either $\Delta\xi$ or $\Delta\eta$, and is stable for negative transverse velocity if proper step sizes are chosen. A schematic of the difference model is presented in Figure 3.a. It should be noted that the equations are written at the point $(0,n)$ and solved for the values of the quantities ϕ , θ and G at the point $(2,n)$. Thus, the quantities

$$\left(\frac{\partial^2 \omega}{\partial \zeta^2}\right)_{0,n}, \left(\frac{\partial \omega}{\partial \zeta}\right)_{0,n}, \left(\frac{\partial \omega}{\partial \xi}\right)_{0,n}, \left(\frac{\partial \omega}{\partial \eta}\right)_{0,n}, \text{ and } \omega_{0,n},$$

where the subscripts $(0,n)$ refer to the point $(0,n)$, can be expressed as:

$$\omega_{0,n} = \frac{\omega_{2,n} + \omega_{3,n}}{2} + o(\Delta^2), \quad (3.01)$$

$$\left(\frac{\partial \omega}{\partial \zeta}\right)_{0,n} = \frac{\left(\frac{\partial \omega}{\partial \zeta}\right)_{2,n} + \left(\frac{\partial \omega}{\partial \zeta}\right)_{3,n}}{2} + o(\Delta^2), \quad (3.02)$$

and

$$\left(\frac{\partial^2 \omega}{\partial \zeta^2}\right)_{0,n} = \frac{\left(\frac{\partial^2 \omega}{\partial \zeta^2}\right)_{2,n} + \left(\frac{\partial^2 \omega}{\partial \zeta^2}\right)_{3,n}}{2} + o(\Delta^2), \quad (3.03)$$

where

$$\left(\frac{\partial \omega}{\partial \zeta}\right)_{i,n} = \frac{\omega_{i,n+1} - \omega_{i,n-1}}{2\Delta\zeta} + o(\Delta\zeta^2) \quad (3.04)$$

and

$$\left(\frac{\partial^2 \omega}{\partial \zeta^2}\right)_{i,n} = \frac{\omega_{i,n+1} - 2\omega_{i,n} + \omega_{i,n-1}}{\Delta\zeta^2} + o(\Delta\zeta^2), \quad (3.05)$$

} with $i = 2, 3$

$$\left(\frac{\partial \omega}{\partial \xi}\right)_{0,n} = \frac{\omega_{2,n} - \omega_{3,n}}{\Delta\xi} + o(\Delta^2), \quad (3.06)$$

and

$$\left(\frac{\partial \omega}{\partial \eta}\right)_{0,n} = \frac{(\omega_{2,n} - \omega_{1,n}) + (\omega_{4,n} - \omega_{3,n})}{2\Delta\eta} + o(\Delta^2). \quad (3.07)$$

The governing equations (2.23) through (2.25) can be written in the following general form:

$$\left(\frac{\partial^2 \omega}{\partial \zeta^2}\right)_n + \alpha'_{1n} \left(\frac{\partial \omega}{\partial \zeta}\right)_n + \alpha'_{2n} \omega_n + \alpha'_{3n} + \alpha'_{4n} \left(\frac{\partial \omega}{\partial \xi}\right)_n + \alpha'_{5n} \left(\frac{\partial \omega}{\partial \eta}\right)_n = 0. \quad (3.08)$$

Substituting equations (3.01) through (3.07) and rearranging yields the following expressions for (3.08):

$$A'_n \omega_{2,n-1} + B'_n \omega_{2,n} + C'_n \omega_{2,n+1} = D'_n. \quad (3.09)$$

where

$$A'_n = \frac{1}{2} \left(\frac{1}{\Delta \zeta^2} - \frac{\alpha'_{1n}}{2\Delta \zeta} \right), \quad (3.10)$$

$$B'_n = \left(\frac{\alpha'_{2n}}{2} - \frac{1}{\Delta \zeta^2} + \frac{\alpha'_{4n}}{\Delta \xi} + \frac{\alpha'_{5n}}{2\Delta \eta} \right), \quad (3.11)$$

$$C'_n = \frac{1}{2} \left(\frac{1}{\Delta \zeta^2} + \frac{\alpha'_{1n}}{2\Delta \zeta} \right), \quad (3.12)$$

and

$$D'_n = - \left[\alpha'_{3n} + \left(\frac{1}{2\Delta \zeta^2} + \frac{\alpha'_{1n}}{4\Delta \zeta} \right) \omega_{3,n+1} \right] \quad (3.13)$$

$$\begin{aligned}
 & + \left(\frac{1}{2\Delta\zeta} - \frac{\alpha_1 n}{4\Delta\zeta} \right) \omega_{3,n-1} - \frac{\alpha_5 n}{2\Delta\eta} \omega_{1,n} \\
 & + \left(\frac{\alpha_2 n}{2} - \frac{1}{\Delta\zeta} - \frac{\alpha_4 n}{\Delta\zeta} - \frac{\alpha_5 n}{2\Delta\eta} \right) \omega_{3,n} + \frac{\alpha_5 n}{2\Delta\eta} \omega_{4,n} \Big] .
 \end{aligned}$$

In the special case for which there is similarity in the ξ -direction for example at the tip of a sharp cone or the nose of a blunted cone, a Crank-Nicolson finite-difference scheme can be used in the cross-flow direction with accuracy of order $\Delta\eta^2$. In this scheme, the equations are written at the 0-point and solved for the value of the quantities θ , ϕ , and G at the 2-point. Thus, yields the following relations (Fig. 3.1b) for the value and partial derivatives of a variable:

$$\omega_{0,n} = \frac{\omega_{2,n} + \omega_{1,n}}{2} + O(\Delta\eta^2), \quad (3.14)$$

$$\left(\frac{\partial \omega}{\partial \zeta} \right)_{0,n} = \frac{\left(\frac{\partial \omega}{\partial \zeta} \right)_{2,n} + \left(\frac{\partial \omega}{\partial \zeta} \right)_{1,n}}{2} + O(\Delta\eta^2), \quad (3.15)$$

$$\left(\frac{\partial^2 \omega}{\partial \zeta^2} \right)_{0,n} = \frac{\left(\frac{\partial^2 \omega}{\partial \zeta^2} \right)_{2,n} + \left(\frac{\partial^2 \omega}{\partial \zeta^2} \right)_{1,n}}{2} + O(\Delta\eta^2), \quad (3.16)$$

where

$$\left(\frac{\partial \omega}{\partial \zeta} \right)_{i,n} = \frac{\omega_{i,n+1} - \omega_{i,n-1}}{2\Delta \zeta} + o(\Delta \zeta^2) \quad (3.17)$$

and

$$\left(\frac{\partial^2 \omega}{\partial \zeta^2} \right)_{i,n} = \frac{\omega_{i,n+1} - 2\omega_{i,n} + \omega_{i,n-1}}{\Delta \zeta^2} + o(\Delta \zeta^2) \quad (3.18)$$

and

$$\left(\frac{\partial \omega}{\partial \eta} \right)_{0,n} = \frac{\omega_{2,n} - \omega_{1,n}}{\Delta \eta} + o(\Delta \eta^2). \quad (3.19)$$

Similarly, as before, the governing equations can be written in the form of equation (3.08) with $\alpha_4 = 0$; upon substituting the finite-difference form of the partial derivatives as specified in equations (3.14) through (3.19) into (3.08) a relation of the form of equation (3.09) is obtained. In this case,

$$A'_n = \left(\frac{1}{2} - \frac{\alpha'_1}{4\Delta \zeta} \right), \quad (3.20)$$

$$B'_n = \left(\frac{\alpha'_2}{2} - \frac{1}{\Delta \zeta^2} + \frac{\alpha'_5}{\Delta \eta} \right), \quad (3.21)$$

$$C'_n = \left(\frac{1}{2\Delta\zeta} + \frac{\alpha'_{1n}}{4\Delta\zeta} \right), \quad (3.22)$$

and

$$D'_n = - \left[\alpha'_{3n} + \left(\frac{1}{2\Delta\zeta} + \frac{\alpha'_{1n}}{4\Delta\zeta} \right) \omega_{1,n+1} \right] \quad (3.23)$$

$$- \left[\left(\frac{1}{2\Delta\zeta} - \frac{\alpha'_{1n}}{4\Delta\zeta} \right) \omega_{1,n-1} + \left(\frac{\alpha'_{2n}}{2} - \frac{1}{\Delta\zeta} - \frac{\alpha'_{5n}}{\Delta\eta} \right) \omega_{1,n} \right].$$

Equation (3.08) can be evaluated in a similar way for the case similarity in the η -direction with $\alpha'_{5n} = 0$.

Finally, an iterative finite-difference scheme is used for the case of similarity in both the ξ -coordinate and the η -coordinate. In this case the governing equations reduce to ordinary differential equations with the equations being written at the 2-point and the values generated at the 2-point; subsequently, the accuracy is of order $\Delta\zeta^2$. The partial derivatives, which are now actually total derivatives, become:

$$\left(\frac{\partial \omega}{\partial \zeta} \right)_{2,n} = \frac{\omega_{2,n+1} - \omega_{2,n-1}}{2\Delta\zeta} + O(\Delta\zeta^2) \quad (3.24)$$

and

$$\left(\frac{\partial^2 \omega}{\partial \zeta^2} \right)_{2,n} = \frac{\omega_{2,n+1} - 2\omega_{2,n} + \omega_{2,n-1}}{\Delta\zeta^2} + O(\Delta\zeta^2). \quad (3.25)$$

Again, the governing equations can be written in the form of equation (3.08) with $\alpha'_{4n} = \alpha'_{5n} = 0$. Upon substituting the finite-difference form of the partial derivatives as expressed by equations (3.24) and (3.25) into equation (3.08) equation (3.09) results, where:

$$A'_n = \left(\frac{1}{\Delta \zeta^2} - \frac{\alpha'_{1n}}{2\Delta \zeta} \right), \quad (3.26)$$

$$B'_n = \left(\frac{-2}{\Delta \zeta^2} + \alpha'_{2n} \right), \quad (3.27)$$

$$C'_n = \left(\frac{1}{\Delta \zeta^2} + \frac{\alpha'_{1n}}{2\Delta \zeta} \right), \quad (3.28)$$

$$\text{and } D'_n = -\alpha'_{3n}. \quad (3.29)$$

Thus, one can apply equation (3.09) at N-2 evenly spaced points in the normal direction from point 2, one step away from the outer edge, to point N-1 one step away from the wall.

The general solution to equation (3.09), as given by Richtmeyer (ref. 11) for example, is of the form:

$$\omega_{2,n} = E'_n \omega_{2,n+1} + F'_n. \quad (3.30)$$

If one applies the outer-edge boundary conditions at $\zeta = 0$ and requires that equation (3.30) holds independently

of step size, the resulting conditions are:

$$E'_1 = 0$$

and $F'_1 = 0, 1, 1$ respectively for ϕ , θ , and G .

Then the following recursion relations can be derived:

$$E'_n = \frac{-C'_n}{A'_n E'_{n-1} + B'_n} \quad (3.31)$$

and

$$F'_n = \frac{D'_n - A'_n F'_{n-1}}{A'_n E'_{n-1} + B'_n} \quad (3.32)$$

With the known values of the variables at the wall and known E'_n and F'_n , one can calculate the values of $\omega_{2,N-1}$ to $\omega_{2,2}$.

The boundary conditions at the wall for θ and G are $\frac{t_w}{t_e}$ and 0, respectively. However, the boundary condition at the wall on ϕ from (2.34) has the following form:

$$\left(\frac{\partial \phi}{\partial \zeta}\right)_{2,N} = (-A_3 H_{2,N} - \frac{A_7 \ell_{2,N} \theta_{2,N}}{\phi_{2,N}} - \phi_{2,N}). \quad (3.33)$$

With a 3-point difference form for the above partial derivatives at the wall, one obtains:

$$\left(\frac{\partial \phi}{\partial \zeta}\right)_{2,N} = \frac{1}{2\Delta\zeta} (3\phi_{2,N} - 4\phi_{2,N-1} + \phi_{2,N-2}) + O(\Delta\zeta^2). \quad (3.34)$$

Now using equation (3.09) for ϕ at the point N-1 gives and additional relation:

$$A'_{N-1}\phi_{2,N-2} + B'_{N-1}\phi_{2,N-1} + C'_{N-1}\phi_{2,N} = D'_{N-1} \quad (3.35)$$

The final expression for this boundary condition is determined by applying equation (3.30) for ϕ at N-1:

$$\phi_{2,N-1} = E'_{N-1}\phi_{2,N} + F'_{N-1} \quad (3.36)$$

Applying equations (3.34) through (3.36) and evaluating for $\phi_{2,N}$, one arrives at a quadratic equation having solution:

$$\phi_{2,N} = \frac{-b' - \sqrt{b'^2 - 4a'c'}}{2a'} \quad (3.37)$$

with

$$a' = \frac{C'_{N-1}}{A'_{N-1}} + 4E'_{N-1} + E'_{N-1} \frac{B'_{N-1}}{A'_{N-1}} - 2\Delta\zeta - 3, \quad (3.38)$$

$$b' = 4F'_{N-1} + F'_{N-1} \frac{B'_{N-1}}{A'_{N-1}} - \frac{D'_{N-1}}{A'_{N-1}} - A_3 2\Delta\zeta H_{2,N}, \quad (3.39)$$

and

$$c' = -A_7 \ell_{2,N} \theta_{2,N} 2\Delta\zeta. \quad (3.40)$$

It should be remembered that the coefficients A_n in equation (3.09) are functions of the dependent variables ϕ , θ , and G and are unknown a priori. An initial guess for these unknown variables is required and the result is iterated upon until the values of these unknown variables are relaxed.

It has been found that the $1/\phi$ term in equation (2.25) and subsequently in equation (3.08) caused the iteration scheme to diverge. Therefore, a "quasi-linearization" of this particular term was introduced as follows:

$$1/\phi = 2/\phi_G - \phi/\phi_G^2 \quad (3.41)$$

where ϕ_G is the value of the shear parameter at the previous iteration; with this modification the solution converged rapidly.

3.1 General Solution Technique

The system of non-linear second order parabolic equations developed in Section 2 are solved simultaneously by an iterative process for a sharp circular cone and for a spherically blunted cone. The governing equations (2.23) to (2.25) are reduced by replacing the partial derivatives by finite difference expressions, to algebraic equations having the tridiagonal form of equation (3.08). The α_i coefficients in equation (3.08) are functions of the dependent variables θ , ϕ and G which are to be determined and must be represented

by their assumed initial values and are subsequently updated during the iteration process. At the tip of a sharp cone or at the stagnation point of a sphere cone (which correspond to $\xi = 0$ and $\eta = 0$) similarity in the ξ and η directions exist. The mathematical solution at this point is considered as a limiting case as $\xi \rightarrow 0$ and $\eta \rightarrow 0$. The governing equations at this point reduce to ordinary differential equations in ζ only. The solution to this two-point boundary-value problem is a starting solution. For grid points on the surface corresponding to $\xi = 0$ and $\eta > 0$, similarity in ξ exists (there is no ξ -dependence in the equations) and the solutions are obtained using the starting solution and marching circumferentially around the body in the η -direction. Thus, the solution in the (η, ζ) plane is reduced to a two-dimensional problem. In the plane (ξ, ζ) , with $\eta = 0$ and $\xi > 0$, similarity in η exists and two-dimensional solutions in the windward meridian plane are obtained. For points outside of the $\xi = 0$ and $\eta = 0$ planes the dependence on ξ , η and ζ exists and the solutions are obtained by using the solution at the windward plane and marching in planes around the body in the η -direction and stepping forward in ξ -direction (Fig. 3.2). At each (ξ, η) grid point on the surface, iteration is applied on the values of θ , ϕ and G in the normal direction until the slope of the shear parameter in the normal direction is relaxed.

4. SOLUTIONS FOR SHARP CIRCULAR CONES AT ANGLE OF ATTACK WITH STREAMLINE SWALLOWING

The recent contribution in the field of three-dimensional boundary-layer studies by McGowan and Davis (ref. 5) has extended the numerical analysis of three-dimensional laminar flow to sharp circular or elliptical cones at angle of attack. The work by Boericke (ref. 4) treats laminar flow over circular cones at angle of attack using Moore's transformation and numerical as well as experimental surface pressure distributions. Quite recently the work by Mayne (ref. 12) presents an analysis of laminar boundary-layers on right circular cones at angle of attack, including the effects of streamline entropy swallowing with the assumption of a negligible effect of streamline swallowing in the windward plane (a similarity solution at $\xi = \eta = 0$ has been used to apply to the region $\xi > 0, \eta = 0$).

In the present work a method for solving for flows over sharp cones at angle of attack with streamline entropy swallowing is developed. The details of this method will be presented in the following sections.

4.1 The Geometry of the Problem

In spherical coordinates, an infinitesimal arc length is given by (Fig. 4.1):

$$dl^2 = dr^2 + r^2(d\phi^2 + \sin^2\phi d\theta^2). \quad (4.01)$$

In the ξ, η, ζ body-oriented coordinate system, as shown in Figure 4.2, an infinitesimal arc length along the surface of a sharp cone is

$$dl^2 = h_1^2 d\xi^2 + h_2^2 d\eta^2 \quad (4.02)$$

where one can identify

$$r = \xi \text{ and } h_2 = \xi$$

$$h_1 = 1, d\eta = \sin\phi d\theta \quad (4.03 \text{ a-f})$$

$$\frac{\partial h_2}{\partial \xi} = 1 \text{ and } \frac{\partial h_2}{\partial \eta} = 0$$

4.2 Conditions at the Outer Edge of the Boundary Layer

The usual procedure of matching the viscous and inviscid flow fields at the edge of the boundary layer assumes the inviscid value of the pressure at the body surface and the entropy value consistent with the oblique shock or stagnation streamline value. It has been indicated, however, that there is a need to develop solution techniques which include shock layer vorticity (ref. 13). In the current scheme the initial step in determining the inviscid edge properties is to obtain a boundary layer solution for inviscid values at the surface. Having obtained the magnitude of the boundary-layer thickness, new inviscid values are obtained by interpolating the inviscid properties for cones (ref. 14) around the body at a distance

from the wall equal to the boundary layer thickness. With these inviscid properties, a new boundary-layer solution is then obtained at the next downstream station.

The scheme adopted for determining the inviscid properties is based on the invariance of total enthalpy in the inviscid part of the shock layer which is true if the total enthalpy in the freestream is constant. Due to the presence of vorticity in the inviscid flow, the velocity and temperature gradients are no longer zero at the boundary layer edge. However, it is assumed that the net energy flux between adjacent fluid laminae in the edge region, particularly on sharp bodies becomes negligible.

4.3 Non-Isentropic Conditions

The entropy is defined by the expression

$$ds = \left(\frac{dg}{T} \right)_{\text{rev}} .$$

Using the thermodynamic relation

$$ds = \frac{dh - vdp}{T}$$

one can show for a perfect gas with constant specific heats with

$$pv = RT ,$$

$$\frac{\bar{C}_p}{\bar{C}_v} = \gamma$$

$$\bar{C}_p - \bar{C}_v = R$$

that the change of entropy is related to pressure and density by the expression

$$\bar{S} - \bar{S}_{\text{ref}} = \bar{C}_v \ln \frac{\bar{p}/\bar{p}_{\text{ref}}}{(\bar{\rho}/\bar{\rho}_{\text{ref}})^\gamma} .$$

Therefore the parameter

$$K = p/\rho^\gamma \quad (4.04)$$

is a measure of the change of entropy and can be used to relate the value of entropy to pressure and density.

4.4 Boundary Layer Thickness

The physical coordinate normal to the surface of the body is defined by equation (2.38) as

$$\bar{S}_3 = - \int_{\zeta}^1 \frac{\bar{L}}{\phi} \xi^* \theta d\zeta \frac{\bar{L}}{\sqrt{Re}} \quad (4.05)$$

which results in

$$\frac{\bar{S}_3 \sqrt{Re}}{\bar{L} \xi^*} = - \int_{\zeta}^1 \frac{\bar{L}}{\phi} \theta d\zeta = Y(\zeta) \quad (4.06)$$

If we define the thickness of the boundary layer at the point where the local tangential velocity u in the streamwise ξ -direction reaches 90% of the edge value or where $F = \frac{u}{u_e} = .9$, we obtain the boundary layer thickness $\bar{\delta} = \bar{S}_3 \text{ } F=.9$:

$$\left[\frac{\bar{\delta}}{\bar{L}} \frac{\sqrt{Re}}{\sqrt{\xi}} = Y(N) \right]_{F = .9}$$

where ξ^* was replaced by $\sqrt{\xi}$ in order to insure similarity at the tip (see section 4.9). With Reynolds number defined by

$$Re = \frac{\bar{\rho}_\infty \bar{u}_\infty \bar{L}}{\bar{\mu}_\infty}$$

we obtain an expression for the boundary layer thickness

$$\bar{\delta} = \bar{S}_3 = \frac{\sqrt{\xi} Y_{F=.9} L}{\sqrt{Re}} \quad (4.07)$$

4.5 Location of the Edge of the Boundary-Layer

The location of the edge of the boundary-layer in the shock layer is specified in terms of the $\bar{\xi}$ parameter which identifies rays in the conical flow (Fig. 4.3):

$$\bar{\xi} = \frac{\bar{a}}{\bar{b}}$$

The expression for the $\bar{\xi}$ parameter when evaluated in terms of the boundary-layer thickness $\bar{\delta}$ and body coordinate ξ , takes the form

$$\bar{\xi} = \frac{\bar{\delta}/\cos^2 \phi_c}{(\xi \bar{L} - \bar{\delta} \tan \phi_c) (\tan \phi_s(\phi) \tan \phi_c)} \quad (4.08)$$

The shock angle ϕ_s is interpolated by the interpolation routine as $\phi_s = \phi_s(\eta)$ and the $\bar{\delta}$ value is known from the previous ξ station.

4.6 Inviscid Data

The inviscid data used as an input to solve the boundary-layer equations is obtained from Jones (ref. 14). In order to obtain a consistent set of inviscid data for the case of entropy swallowing, the input values of v_e , w_e , p_e , and ρ_e at discrete points around the periphery of a body, and Bernoulli's equation

$$v_e^2 + w_e^2 + u_e^2 + \frac{2p_e}{\rho_e} \frac{\gamma}{\gamma-1} - 2h_0 = 0 \quad (4.09)$$

are used.

In the above equation the expression for v_e is found from the ξ -momentum equation

$$v_e = \frac{\partial u_e}{\partial \eta} + \frac{\xi u_e}{v_e} \frac{\partial u_e}{\partial \xi} + \frac{\xi}{v_e \rho_e} \frac{\partial p_e}{\partial \xi} \quad (4.10)$$

and a 5-point difference expression for $\frac{\partial u_e}{\partial \eta}$ is used, i.e.

$$\frac{\partial u_e}{\partial \eta} = \frac{8(u_{j+1} - u_{j-1}) - (u_{j+2} - u_{j-2})}{12\Delta\eta} \quad (4.11)$$

The following two expressions require special attention in the plane of symmetry where $v_e = 0$:

$$\frac{1}{v_e} \frac{\partial u_e}{\partial \xi} \quad \text{and} \quad \frac{1}{v_e} \frac{\partial p_e}{\partial \xi} \quad (4.12)$$

The first expression is obtained by a limit process and the second one is obtained from the ξ -momentum equation

$$\frac{\xi}{v_e} \frac{\partial u_e}{\partial \xi} = \frac{1}{u_e} \left(v_e - \frac{\partial u_e}{\partial \eta} - \frac{\xi}{\rho_e} \frac{1}{v_e} \frac{\partial p_e}{\partial \xi} \right) \quad (4.13)$$

With equation (4.10), equation (4.09) becomes

$$\begin{aligned} & \left(\frac{\partial u_e}{\partial \eta} \right)^2 + u_e^2 + u_e^2 \left(\frac{\xi}{v_e} \frac{\partial u_e}{\partial \xi} \right)^2 + \left(\frac{\xi}{\rho_e v_e} \frac{\partial p_e}{\partial \xi} \right)^2 + u_e \frac{\partial u_e}{\partial \eta} \left(\frac{2\xi}{v_e} \frac{\partial u_e}{\partial \xi} \right) \\ & + \frac{\partial u_e}{\partial \eta} \left(\frac{2}{\rho_e} \frac{\xi}{v_e} \frac{\partial p_e}{\partial \xi} \right) + 2u_e \left(\frac{\xi}{v_e} \frac{\partial u_e}{\partial \xi} \right) \left(\frac{\xi}{\rho_e v_e} \frac{\partial p_e}{\partial \xi} \right) + w_e^2 \\ & + 2 \left(\frac{2\gamma}{\gamma-1} p_e \frac{\gamma-1}{\gamma} K \frac{1}{\gamma} - h_0 \right) = F \end{aligned} \quad (4.14)$$

which is of the form

$$F \left(h_0, u_e, v_e, w_e, p_e, K, \xi, \frac{\partial u_e}{\partial \xi}, \frac{\partial u_e}{\partial \eta}, \frac{\partial p_e}{\partial \xi}, \frac{\partial p_e}{\partial \eta} \right) = 0 .$$

Introducing equation (4.11) and evaluating the equation (4.14) at N points, a set of N simultaneous nonlinear equations in

$$\bar{u} = (u_1, u_2, \dots, u_n)$$

is obtained and is solved by the Newton-Rapson iteration technique using the Gauss-Jordan method.

Defining

$$F_{ij}(\bar{u}) = \frac{\partial F_i(\bar{u})}{\partial u_j} = \phi(\bar{u}) \quad (4.15)$$

with the starting velocity vector

$$\bar{u}_0 = (u_{10}, u_{20}, \dots, u_{n0})$$

the solution vector for velocity is

$$\bar{u}^{k+1} = \bar{u}^k + \bar{\delta}^k \quad (4.16)$$

where $\bar{\delta}^k$ is the solution vector for the set of simultaneous linear equations

$$\phi(\bar{u}) \bar{\delta}_j = -F_i(\bar{u}) \quad (4.17)$$

and is obtained by the Gauss-Jordan method.

With

$$\bar{\delta}_j = - \Delta \bar{u}_j \quad (4.18)$$

the solution vector for velocity is determined for the k-th iteration

$$\bar{u}_j^{k+1} = \bar{u}_j^K - \Delta \bar{u}_j^K . \quad (4.19)$$

In order to compute the values of u_e which are consistent with the entire set of the inviscid data, the following inviscid values have to be given or generated:

$$p_e, u_e, v_e, w_e, K = \frac{p_e}{\rho_e \gamma}, \frac{\partial p_e}{\partial \xi}, \frac{\partial p_e}{\partial \eta}, \frac{\partial u_e}{\partial \xi}, \frac{\partial u_e}{\partial \eta}$$

where u_e can be used as initial values. In evaluating the inviscid values, the symmetry relations for the windward and leeward planes are utilized. All interpolations are made by the cubic spline method (Appendix B).

In the present analysis, including the effect of the entropy swallowing, the edge conditions are determined at the normal distance δ from the wall and they vary from station to station in the ξ direction giving rise to gradients $\frac{\partial Q}{\partial \xi}$, where $Q = u_e, v_e, p_e$, and t_e . The derivative $\frac{\partial v_e}{\partial \xi}$ is obtained from the η -momentum equation (2.02) as

$$\frac{\partial v_e}{\partial \xi} = - \left(\frac{v_e}{\xi} + \frac{1}{\xi \rho_e u_e} \frac{\partial p_e}{\partial \eta} + \frac{v_e}{\xi u_e} \frac{\partial v_e}{\partial \eta} \right) \quad (4.20)$$

and the $\frac{\partial t_e}{\partial \xi}$ derivative is obtained from the energy equation (2.03) as

$$\frac{\partial t_e}{\partial \xi} = \frac{1}{u_e} \left[\frac{\gamma-1}{\gamma} \frac{1}{\rho_e} \left(u_e \frac{\partial p_e}{\partial \xi} + \frac{v_e}{\xi} \frac{\partial p_e}{\partial \eta} \right) - \frac{v_e}{\xi} \frac{\partial t_e}{\partial \eta} \right]. \quad (4.21)$$

In order to obtain $\frac{\partial t_e}{\partial \eta}$ in this expression, the equation

$$t_e = p_e^{\frac{\gamma-1}{\gamma}} K(\eta)^{\frac{1}{\gamma}}$$

is used as follows:

$$\frac{\partial t_e}{\partial \eta} = \frac{\gamma-1}{\gamma} \frac{t_e}{p_e} \frac{\partial p_e}{\partial \eta} + \frac{1}{\gamma} \left(\frac{t_e}{p_e} \right)^{1-\gamma} \frac{\partial K}{\partial \eta} \quad (4.22)$$

For the case of constant entropy with zero values of derivatives in the quantities $\frac{\partial Q}{\partial \xi}$, the inviscid ξ -momentum equation applied at the surface yields:

$$\frac{\partial u_e}{\partial \eta} = v_e, \quad (4.23)$$

and using the fact that the entropy is constant on the surface of a cone:

$$K = \frac{p_e}{\rho_e^\gamma} \quad (4.24)$$

One can then generate the entire set of inviscid data by the method described previously.

The value of the inviscid, outer edge temperature is obtained from (4.18) along with the perfect gas law (2.05) to

$$t_e = (K p_e^{\gamma-1})^{1/\gamma} \quad (4.25)$$

and therefore

$$\frac{\partial t_e}{\partial \eta} = \frac{(\gamma-1)}{\gamma} \frac{t_e}{p_e} \frac{\partial p_e}{\partial \eta} \quad (4.26)$$

From the inviscid η -momentum equation, one can get an expression for the pressure derivative:

$$\frac{1}{\rho_e} \frac{\partial p_e}{\partial \eta} = -v_e \left(\frac{\partial v_e}{\partial \eta} + u_e \right) \quad (4.27)$$

This form of the pressure derivative is convenient since the value of $\frac{1}{v_e} \frac{p_e}{\partial \eta}$ is necessary in (A10) and although both $\frac{\partial p_e}{\partial \eta}$ and v_e go to zero at certain points, the quantity $\frac{1}{v_e} \frac{\partial p_e}{\partial \eta}$ does not, for example at the windward streamline.

The inviscid flow properties are determined by the previously described method which reduces to a solution of a set of non-linear simultaneous equations for u_e . In solving this system the following two cases are considered:

1) for isentropic conditions the surface entropy is assumed to be constant for the entire shock layer, $K = p/\rho^\gamma = \text{constant}$

2) for entropy swallowing the entropy varies with η , ξ and ζ , therefore, for each ξ station the value of K at the edge of the boundary layer is $K = K(\eta) = \frac{p(\eta)}{\rho(\eta)^\gamma}$. Since both pressure and density vary in the normal and circumferential directions, $p = p(\eta, \zeta)$ and $\rho = \rho(\eta, \zeta)$ are obtained by a double interpolation routine using cubic splines as $p(\eta) = p(\eta, \bar{\delta})$ and $\rho(\eta) = \rho(\eta, \bar{\delta})$. With the $p(\eta)$ and $\rho(\eta)$ values known, the velocity u_e is obtained by the method described in this section. In order to make the inviscid values generated by Jones (ref. 14) consistent with this program, certain conversion factors have to be introduced:

$\rho = \frac{\bar{p}}{\bar{p}_\infty} = \rho_J$, where subscript J denotes data by Jones
and

$$p = \frac{\bar{p}}{\bar{p}_\infty} = p_J \left(\frac{\gamma}{2} M^2 \sin^2 \phi_c \right)$$

4.7 Limitations of the Inviscid Flow Methods

The boundary layer equations can be solved once the inviscid edge conditions are prescribed. The computation of the inviscid properties is complicated by the existence of a strong entropy gradient and the occurrence of a singularity at the leeward symmetry plane.

The flow around a cone at an angle of attack, which is of interest in this work, is rather complex. One can distinguish the region on the lower surface of the cone which can be represented by elliptic equations. In this region the effect of the boundary layer is present but one can assume that the results of the inviscid theory are valid. The flow above the body is represented by hyperbolic equations and can be solved by the method of characteristics reaching in some cases as far as leeward plane. However, the flow symmetry is not satisfied in this region for high angles of attack which indicates in general the possible presence of internal shocks (ref. 27). The region near the leeward plane with separated flow and internal imbedded shocks is dominated by strong viscous effects and should be handled by equations which include viscous effects even outside of the boundary layer (ref. 15). The possibility of the presence of internal shocks can be inferred from the fact that the flow Mach number in the cross-plane reaches values greater than unity on the upper surface (Fig. 4.4). It can be concluded from the scatter of the inviscid data that the computed inviscid data are not accurate for these conditions and the computed viscous parameters may not be precise.

Current techniques for obtaining the inviscid flow properties include perturbation methods (refs. 16-18) and numerical methods (refs. 19-22). The perturbation methods rely on first order perturbation solutions for the velocity components and lead to considerable inaccuracy in velocities

and pressure at large Mach numbers and at moderate to large angles of attack. The numerical methods for computing the inviscid conical flow are applicable at relative angles of attack α/ϕ_c up to unity. The computed pressure distribution is generally fairly accurate, however, the computed values of velocity components u and v are not. A more consistent set of inviscid data is possible by using the computed or experimental pressure distribution and entropy value at the windward plane and computing v , ρ , and u from cross-flow momentum, conservation of total enthalpy and constancy of entropy at the surface (ref. 4). A comparison of the pressure distributions computed by various methods (ref. 4) including the values used in this analysis is given in Figure 4.5. The pressure by Moretti (ref. 19) and by Jones (ref. 14) give the best agreement with the test data by Tracy (ref. 23). Since the present method accounts for the effects of entropy swallowing and the pressure distribution across the entire shock layer is required, the readily available inviscid values by Jones were used. It should be noted that this pressure is a fairly good approximation to experimental pressure over most of the body, but may become inadequate in the leeward region where the strong interaction with the viscous flow is not accounted for.

4.8 Difficulties at the Leeward Plane

In solving three-dimensional laminar boundary layer equations, difficulties were encountered in obtaining solutions

at the leeward symmetry plane where a complex interaction between the inviscid flow and the boundary layer occurs, (Moore, ref. 24). Moore showed that the cross-flow momentum equation has a unique asymptotic solution at certain condition and non-uniqueness occurs otherwise. This indeterminacy was attributed by Moore to a lack of previous history of the fluid which enters the leeward region from around the cone. Solutions in this region were studied by a number of authors, Moore (ref. 25); Cheng (ref. 26); Vvedenskaya (ref. 27); Libby (refs. 28-29), and Dwyer (ref. 30). Murdock (ref. 31) obtained solutions in the leeward region which were not known previously and determined conditions for which the boundary layer in this region is independent of the out-of-plane flow. He investigated cases for which complete boundary layer solution does not exist and concluded that the boundary layer model has a defect in this case which results in discontinuous derivatives in the leeward plane. This is the region where the boundary layer model breaks down and the continuity of mass is not satisfied.

It was found in this study that the boundary layer solution at the leeward plane does not exist, and that the region within which convergence cannot be obtained grows with angle of attack. It is believed that the boundary layer equations are inadequate in this region which was demonstrated by the inability to produce solutions except at small and moderate angles of attack. This seems to be confirmed by the fact that the boundary layer thickness does not grow

as fast as was observed experimentally in the leeward region.

4.9 Solution to the Problem

The governing equations to be solved are (2.23) through (2.25). Implicit within this set of three equations, the quantities A_1, A_2, \dots, A_{19} (see equations (A1) through (A19)) need to be specified. These nineteen quantities determine all the inviscid and geometric restrictions on the flow. However, the quantity ξ^* has yet to be determined. In order for the quantities $A_8, A_6,$ and A_{15} to remain finite at the tip of the sharp cone, ξ^* must be chosen to be $\sqrt{\xi}$ (this could have been deduced from the usual form of the similarity transformation as is used for most compressible cone solutions). Note that now the three governing equations (2.23) through (2.25) are similar in ξ for the case of constant entropy since there is no dependence of the inviscid quantities on ξ and since there is no explicit dependence of the set A_1, A_2, \dots, A_{19} . $A_4, A_7, A_{11},$ and A_{18} are zero along with terms such as $\frac{\partial G}{\partial \xi}, \frac{\partial \theta}{\partial \xi},$ and $\frac{\partial \phi}{\partial \xi}$. For this set of cases, injection will not be considered so that H_w will be zero. Therefore, the boundary condition on ϕ as in equation (2.34) reduces to the following:

$$\frac{\partial \phi}{\partial \xi} \Big|_w = - \phi_w \quad (4.28)$$

The problem of obtaining the starting solution for the step-by-step integration in the η -direction around the cone still remains. Note that a similarity solution exists at the point at which the transverse pressure gradient, and likewise the transverse velocity given by equation (4.27) is zero. For a circular cone this occurs at the windward and leeward streamlines only. The integration will advance in the positive η -direction from the windward streamline (at $\eta = 0$) in the case of a circular cone.

Thus, the entire set of equations has been specified, and the finite-difference scheme has been developed so that the solution can be integrated step-by-step around the body (Fig. 3.2).

4.10 Results

Based on the analytical model presented, a computer program for solving the system of parabolic boundary-layer equations for a circular cone was developed. This program is a modification of the one developed by McGowan and Davis (ref. 5). This program begins computations for constant entropy at first, computes the boundary-layer thickness at the second step, and switches to the program with entropy swallowing at the third step and approximates the boundary layer thickness at this step (which is not known a priori) by the boundary layer thickness at the preceding step. To be more accurate, after the completion of computations over the prescribed number of steps in the first sweep, a

second sweep can be initiated by returning to the beginning of the program and using the true boundary layer thickness at each station, respectively from the first sweep. The option for performing the second sweep has been provided. As will be shown later, the error resulting from the approximation of the boundary layer thickness by the value from the previous step is negligible.

The computed results include: skin friction, heat transfer, boundary layer thickness, displacement thickness, Stanton number and the normal direction profiles of velocities, temperature, density, and shear parameter. The results of the computations will now be discussed in detail for particular cases presented in Table I. Comparison of results with experimental data and results from other sources will be made.

The computations were performed at conditions which correspond to the tests performed by Tracy (ref. 23) and are:

$$\begin{array}{ll} M_{\infty} = 8 & Re = 4.04 \times 10^4 \text{ where } \bar{L} = 1 \text{ ft.} \\ \phi_C = 10^\circ, \phi_C = 25^\circ & \gamma = 1.4 \\ T_{\infty} = 84.2^\circ R & Pr = .738 \\ T_w = .46 T_o & R = 1718 \text{ ft}^2/\text{sec}^2 \text{ } ^\circ R \\ & C = 198.6^\circ R \end{array}$$

The computed cases are tabulated in Table I. The computations were performed on an IBM 360-65 computer and required a storage capacity of 400K. For the computed cases, 76 points in normal direction from $\zeta = 1$ to $\zeta = 0$ and 61 points in

transverse direction η were used. It was found that this combination of steps represented an optimum from the point of view of convergence, accuracy, and computing time. It took approximately 2.3 seconds to compute the solution at a grid point. The compile time was 4 min. The skin friction and heat transfer were normalized by values $C_{f\xi 0}$ and q_{w0} at zero angle of attack, respectively (Table II). Longitudinal and transverse skin friction and heat transfer distributions in the transverse direction for $\phi_c = 10^\circ$, and $\alpha = 8^\circ, 10^\circ$, and 12° and various values of the Reynolds number are shown in Figures 4.6 to 4.15. The same parameters are shown for $\phi_c = 25^\circ$ and $\alpha = 12.5^\circ$ in Figures 4.16 and 4.17. These figures show values for the constant entropy cases (no swallowing) and for entropy swallowing where inviscid data were interpolated at a distance from the wall equal to the thickness of the boundary layer, δ . Heat transfer results for $\phi_c = 10^\circ$ are compared with the tests by Tracy (ref. 23).

The longitudinal and transverse skin friction distributions for $\phi_c = 10^\circ$, $\alpha = 8^\circ$, and $Re = 4.04 \times 10^4$ are shown in Figure 4.6. The Reynolds number is moderate and the boundary layer has a significant thickness. As a result of entropy swallowing the values of the skin friction are higher than those for constant entropy over almost the entire periphery: about 2% at the windward and 4% at the leeward region. A similar trend is displayed by the heat transfer in Figure 4.7. Heat transfer shows good agreement with the test values by Tracy (ref. 23) except toward the leeward region and windward

region where the computed value is about 3% higher than the test results. Figures 4.8 and 4.9 show the same parameters for higher Reynolds number, $Re = 4.04 \times 10^6$. Because of the thinner boundary layer, smaller entropy swallowing effects are noticeable as is expected. Figures 4.10 and 4.11 show the computational results for $\alpha = 10^\circ$ and $Re = 4.04 \times 10^4$. As before, there is a marked effect of entropy swallowing on $C_{f\xi}$, $C_{f\eta}$ and q_w . A fair agreement of computed heat transfers is still apparent, although the differences are larger near the planes of symmetry and are about 4% at the windward side. The effect of entropy swallowing is reduced by a higher Reynolds number, as is noticeable in Figures 4.12 and 4.13. Considerable difficulties were encountered in obtaining solutions for $\alpha/\phi_c \geq 1$. This is the limit of validity of the inviscid data which becomes progressively more inaccurate as α increases. Figure 4.4 indicates the scatter of the computed inviscid data for $\alpha = 12^\circ$, $\phi_c = 10^\circ$ as obtained by Jones (ref. 14) and the distribution of the flow Mach number in the cross-flow plane, M_c . It is obvious that the inviscid values are inaccurate and the fact that M_c reaches a value of unity at $\theta = 95^\circ$ indicates a possibility of internal imbedded shocks (ref. 27). Results for $\alpha = 12^\circ$ are shown in Figures 4.14 and 4.15. Figures 4.16 and 4.17 show results for $\phi_c = 25^\circ$ and $\alpha = 12.5^\circ$. Although the trends are still the same, the differences between results for entropy swallowing and no swallowing seem to increase. Figure 4.18 represents a compilation of heat transfer distributions for a 10° cone at

$\alpha = 8^\circ$ and includes experimental data by Tracy, results of computations by Boericke (ref. 4) based on experimental pressure, and pressure by Moretti for $M_\infty = 7.95$, and the results by the present method for $M_\infty = 8$. The results of this analysis for entropy swallowing at $M_\infty = 8$ are higher than the results based on pressure by Moretti at $M_\infty = 7.95$ as should be expected. A similar comparison of heat transfer results for $\alpha = 12^\circ$ is shown in Figure 4.19.

The results obtained in this analysis can be compared with the recent solutions by Mayne (ref. 12). The results for $\phi_c = 10^\circ$ and $\alpha = 8^\circ$ (Fig. 4.6, 4.7) show good agreement of skin friction values and heat transfer except in the windward area where Mayne's results show that longitudinal skin friction is identical with the classical value and heat transfer which is lower than the classical value. In the case for $\phi_c = 25^\circ$ and $\alpha = 12.5^\circ$ (Fig. 4.16, 4.17), there is qualitative agreement in the skin friction, except that the results by Mayne for transverse skin friction is becoming lower than the classical toward the leeward side, while the heat transfer results by Mayne are slightly higher near the windward side and become lower for $\theta > 60^\circ$ than the classical values. The heat transfer results by Mayne for these two cases seem to lack consistency as compared with the results of this analysis which are consistently higher or identical for decreasing α values and high Reynolds numbers with streamline swallowing for the range of computed cases. It is believed that these differences are due to the fact that the

streamline swallowing effects in the windward plane have been neglected by Mayne. Mayne argues that the vorticity effects are negligible in this region and assumes the similarity solution at $\xi = 0$, $\eta = 0$ to be valid for $\xi > 0$ and $\eta = 0$. Although the variation of flow properties in the windward plane is small, they are finite. The effects in the adjacent meridian planes are increasing and result in different cross-wise derivatives, $\frac{\partial Q}{\partial \eta}$, which lead to higher values of viscous parameters in this area.

The circumferential boundary layer thickness distribution for $\alpha = 8^\circ$, 10° , and 12° is shown in Figure 4.20. The rate increase of the computed values of δ toward the leeward plane is not as high as of the experimental data by Tracy. The streamwise boundary layer thickness distribution in the meridian planes $\theta = 0^\circ$, 90° , and 150° is shown in Figure 4.21. It follows the law:

$$\delta = \frac{cx}{\sqrt{Re_x}} .$$

The variation of the entropy parameter p/ρ^γ in the circumferential direction is shown in Figure 4.22. The entropy decrease is larger for increasing angle of attack α and for decreasing Reynolds number (larger δ), which is consistent. It can be concluded that the entropy layer grows with the increase of α and δ .

It has been observed that the computed results fluctuate somewhat after the program switches to the variable entropy

scheme as shown in Figure 4.23. This is due to the impact of the different inviscid data set used in the variable entropy part of the program, different parameters used in the finite difference schemes and computed in the constant entropy phase of the program. This is also consistent with a slightly different inviscid data set and due to nonsimilarity of the present scheme ($\frac{\partial Q}{\partial \xi} \neq 0$). These fluctuations practically vanish after the third step.

It was pointed out that the entropy swallowing effects are accounted for by estimating the inviscid data at the distance from the wall equal to δ from the previous step. This approximation results in some error which is shown for $\alpha = 10^\circ$ in Figure 4.24. The results from the second sweep (second set of computations based on true δ from the first set of computations) are higher by .1% at the windward side, .3% and .5% at 90° for q_w and C_f , respectively and go to 3% and 1% for q_w and C_f in the leeward area. For most practical purposes this error is small, and in view of the fact that the leeward results are not precise, the first sweep can be considered as satisfactory.

4.11 Conclusions

The results of the present method for solving the laminar boundary layer equations for a circular cone with entropy swallowing have demonstrated the validity of the approach of this analysis for the representation of viscous flow with the effects of entropy swallowing. In particular, the computed

heat transfer results q_w/q_{w0} are in good agreement with the experimental results by Tracy and with results produced by other methods (ref. 4,12). The effects of entropy swallowing result in values higher than the values for constant entropy and this trend is consistent within the range of the ϕ_c , α and Re values used in these computations. Larger differences occur near the leeward region and this is believed to be due to the inadequacy of the boundary-layer equations as demonstrated in:

1. The inability to predict a sharp rise of boundary layer thickness in this region
2. The inability to produce a solution near the leeward plane which is deteriorating with increase in angle of attack α .

The inviscid flow variables by Jones (ref. 14) seem to be satisfactory for α/ϕ_c up to unity and become inaccurate for larger relative α values over most of the body. They become inadequate near the leeward plane where strong interaction effects may be important.

The error resulting from approximating the boundary layer thickness δ by a value from the previous step is practically negligible and single sweep computations are sufficient.

5. SOLUTIONS FOR BLUNTED CONES AT ANGLE OF ATTACK

Nearly all real configurations for hypersonic vehicles or lifting bodies require a bluntness of finite radius in order to reduce the heat transfer. Since a blunted body is of considerable importance, the second part of this work is devoted to the blunted-cone configuration, in particular to spherically blunted circular cones at angle of attack. The method of solution is similar to the one used for a sharp cone; consequently the same computer program can be used with proper modifications.

5.1 The Geometry of the Problem

The analysis of the viscous boundary layer flow around a blunted cone is performed as follows. The spherical part with symmetrical flow is solved first (Fig. 5.1, region I). After the computations have been carried out a certain distance beyond the body axis, a transfer of coordinates to the spherical part about the body axis with unsymmetrical flow takes place (region II). At the sphere-cone junction, the program switches to the conical coordinate system (region III) and computations are continued in the same way as on a sharp cone.

From the expression for the square of a line element in an orthogonal curvilinear system

$$d\ell^2 = h_1^2 d\xi^2 + h_2^2 d\eta^2 + h_3^2 d\zeta^2 \quad (5.01)$$

one can write for a spherical system (Fig. 5.2)

$$dl^2 = dr^2 + r^2 d\phi^2 + (r \sin\phi)^2 d\theta^2 . \quad (5.02)$$

and identify the scale factors for the surface coordinates as

$$\bar{h}_1 = r , \quad \bar{h}_2 = r \sin\phi , \quad (5.03 \text{ a-d})$$

$$\xi = \phi \text{ and } \eta = \theta .$$

When nondimensionalized by the radius of the sphere r_0 , the following relations hold for the surface of the sphere

$$\begin{aligned} h_1 = \frac{\bar{h}_1}{r_0} = 1 , \quad \frac{\partial h_2}{\partial \xi} = \cos\phi , \\ h_2 = \frac{\bar{h}_2}{r_0} = \sin\phi \text{ and } \frac{\partial h_2}{\partial \eta} = 0 . \end{aligned} \quad (5.04 \text{ a-d})$$

5.2 Flow About a Sphere-Cone

With the scale factors h_1 and h_2 identified, the inviscid coefficients A_i are determined for the symmetrical region I with special attention given to the case of the stagnation point ($\phi = 0$) and the region outside the stagnation point ($\phi > 0$).

The program for the flow about the sphere at an angle of attack is broken up into two parts (Fig. 5.1):

a) symmetrical flow about the wind axis with zero crossflow velocity v_e and azimuth symmetry ($\frac{\partial Q}{\partial \eta} = 0$), this is denoted by region I.

b) unsymmetrical flow about the body axis with non-zero crossflow velocity v_e and crossflow derivatives ($\frac{\partial Q}{\partial \eta} \neq 0$), this is denoted by region II.

Thus, these two regions must be treated separately. One set of inviscid coefficients A_i is specialized to region I and is used to obtain solutions up to an angle $\phi = 3\alpha$. During this phase the results in the plane of symmetry from point ISI to ISF (Fig. 5.3) are stored and will be used as starting solutions for the unsymmetrical region II. Using the geometrical relations between the wind and body systems, the results at a finite number of points from ISI to ISF are interpolated evenly over the entire η region at IWEND points and are used to obtain solutions at the ISF+1 streamwise station and up to the sphere-cone junction CJ.

The position of a point on the sphere in terms of the body coordinate system (x, r, θ) is related to the coordinate x in the symmetrical wind system for a given angle of attack α by the following expression (Fig. 5.4)

$$X_k = R_n + (x_o - R_n) \cos \alpha + r_o \sin \alpha \cos \theta \quad (5.05)$$

Thus, any point on the sphere in the body system along line 1-1 can be reached from the wind system by determining the coordinate X_k .

Since a sphere has no preferred orientation the flow is symmetric in the wind system. The flow in the body system is unsymmetrical. Any point on the sphere and the corresponding flow variables at this point can be obtained from the symmetrical flow about the sphere in the wind system by rotation about the wind axis.

5.3 Method of Solution

The method of solution of the laminar boundary-layer equations for a sphere-cone is essentially the same as the one applied to a sharp cone. For solving the symmetrical sphere flow in region I, it was established (equations 5.03, 5.04) that

$$\begin{array}{lll} \xi = \phi & h_1 = 1 & \frac{\partial h_2}{\partial \xi} = \cos \phi \\ \eta = \theta & h_2 = \sin \phi & \frac{\partial h_2}{\partial \eta} = 0 \end{array}$$

and for similarity to exist at the stagnation point (Appendix C)

$$\xi^* = 1 \quad (5.06)$$

With these relations the inviscid coefficients A_i are specialized to region I by realizing that the crossflow velocity $V_e = 0$ and crossflow derivatives are $\frac{\partial Q}{\partial \eta} = 0$ and that the streamwise derivatives exist, $\frac{\partial Q}{\partial \xi} \neq 0$. In order to be able

to transfer to region II where unsymmetrical flow exist, the computations are carried out to a value of $\xi = 3\alpha$. The computed parameters in the leeward plane are stored and interpolated over the half-range of η in the plane normal to body axis and passing through the last computed point in the leeward plane ISF and are used as starting values in the region II. This region is handled the same way as region I, except that the crossflow velocity and crossflow derivatives are not zero ($V_e \neq 0$, $\frac{\partial Q}{\partial \eta} \neq 0$). After the sphere-cone junction has been reached, computations are performed in the conical coordinate system as for a sharp cone, except that $\xi^* = 1$.

5.4 Inviscid Data

The inviscid flow variables for the sphere-cone analysis were obtained by the method of characteristics by Rakich (ref. 32). The inviscid input data for region I consists of the pressure distribution $p = p(\phi)$, for $\phi = 0$ to $\phi_I = .7986$ radians (Fig. 5.5). With stagnation values specified one obtains the entropy parameter $K = p_o/\rho_o^\gamma$ and total enthalpy

$$H_o = \frac{p_o}{\rho_o} \frac{\gamma}{\gamma-1} \text{ and velocity } u_e = u_e(\phi)$$

$$u_e = \sqrt{2(h_o - (p_e^{\gamma-1} K)^{\frac{1}{\gamma}} (\frac{\gamma}{\gamma-1})} \quad (5.07)$$

In the region II about the body axis, the pressure distribution is generated from the symmetrical pressure $p(\phi)$ from

region I in 7 meridian planes spaced evenly 30° apart by means of relations from section 5.2. These pressure curves are matched with specified pressure distributions in the same meridian planes respectively, beginning at the first location at the axial coordinate x_{II0} . The longitudinal velocity in the windward plane is generated using the relation

$$u_e = \sqrt{2(h_0 - (p_e)^{\gamma-1} K)^{\frac{1}{\gamma}} \frac{\gamma}{\gamma-1}} \quad (5.08)$$

The longitudinal velocity in each cross-plane is obtained by the Newton-Rapson iteration method described in section 4.6 and the crossflow velocity is obtained from the ξ -momentum equation

$$v_e = \tan\phi \left(\frac{u_e}{v_e} \frac{\partial u_e}{\partial \xi} + \frac{1}{\sin\phi} \frac{\partial u_e}{\partial \eta} + \frac{1}{\rho_e v_e} \frac{\partial p}{\partial \xi} \right) \quad (5.09)$$

The relation $\frac{1}{v_e} \frac{\partial p_e}{\partial \xi}$ is computed from equation (5.8). An alternative method for computing the crossflow velocity is determined by the following method. Bernoulli's equation (4.09) is differentiated with respect to ξ and the derivative $\frac{\partial p_e}{\partial \xi}$ is introduced into the momentum equation (2.01) which is specialized to inviscid flow. After some rearrangement one obtains the irrotationality condition on the surface

$$\frac{\partial}{\partial \eta} (h_1 u_e) - \frac{\partial}{\partial \xi} (h_2 v_e) = 0. \quad (5.10)$$

Using a two-point backward finite difference expression for $\frac{\partial v_e}{\partial \xi}$ one arrives at

$$v_{e_{i+1}} = \left[v_{e_i} + \Delta \xi \left(\frac{h_1}{h_2} \frac{\partial u_e}{\partial \eta} + \frac{u_e}{h_2} \frac{\partial h_1}{\partial \eta} \right) \right] / \left(1 + \frac{\Delta \xi}{h_2} \frac{\partial h_2}{\partial \xi} \right) \quad (5.11)$$

Equation (5.11) is much easier to apply than (5.09). Equation (5.10) must be modified if the surface of the body is not a surface of constant entropy.

5.5 Results

Computations for spherically blunted cone were performed for the following conditions:

$$\begin{aligned} M_\infty &= 8 \\ \phi_c &= 10^\circ \\ T_\infty &= 418.87^\circ \text{R} \\ T_w &= .6 T_o \\ R_e &= 1.0 \times 10^6 \\ R_o &= 1 \text{ ft.} \end{aligned}$$

The results for region I are shown in Figure 5.6 and include skin friction, heat transfer, pressure, velocity, u_e , and longitudinal derivatives of pressure and velocity. Skin friction and heat transfer results for region II and III are shown in Figures 5.7 and 5.8. The matching of computed

values at transition from region I to II and from region II to III is good. The circumferential distribution of the skin friction and heat transfer parameters in two cross-planes at $\phi = 56^\circ$ and $\phi = 92^\circ$ is shown in Figure 5.9. Longitudinal pressure and velocity distributions in 7 meridian planes is shown in Figure 5.10, and longitudinal derivatives of pressure and velocity are shown in Figures 5.11 and 5.12. A typical circumferential distribution at $\phi = 56^\circ$ of p_e , u_e , v_e and $\frac{\partial v_e}{\partial \eta}$ is shown in Figure 5.13. The above results for Crocco variables are compared with viscous flow solutions for laminar flow on a blunted cone at the same conditions using Levy-Lees variables (ref. 33) in Figures 5.7 and 5.8. The same pressure was used in both cases, however, the inviscid data were handled differently. This probably accounts for some differences in results. Otherwise, the results show fair agreement as far as magnitude and distribution of parameters are concerned.

5.6 Conclusions

The solutions for viscous laminar flow over a spherically blunted cone were obtained by solving the conservation equations in Crocco variables. The results show fair agreement with similar computations based on Levy-Lees variables and match fairly well at transition points from region I to II (unsymmetrical flow in body system) and from region II to III (conical flow).

Considerable difficulties were encountered in handling

the inviscid data, pressure, velocity and their derivatives. In particular it was difficult to obtain smooth distributions of these curves. Lack of continuity of these curves causes scatter of results or renders a solution impossible. Therefore, a more accurate set of inviscid data would be desirable, and work needs to be done on determining the best way to handle the inviscid data.

REFERENCES

1. Cooke, J.C.; and Hall, M.G.: "Boundary-Layers in Three Dimensions:" Progress in Aeronautical Sciences: Boundary-Layer Problems. Edited by D. Kuchemann and A. Ferri, Vol. II, Pergamon Press, New York, 1962.
2. Mager, A.: "Three-Dimensional Laminar Boundary-Layers, High-Speed Aerodynamics and Jet Propulsion:" Theory of Laminar Flows. Edited by F.K. Moore, Vol. IV, Princeton University Press, Princeton, New Jersey, 1964.
3. Stewartson, K.: The Theory of Laminar Boundary Layers in Compressible Flow. Oxford, Oxford University Press, 1964.
4. Boericke, R.R.: "The Laminar Boundary Layer on a Cone at Incidence in Supersonic Flow." AIAA Paper No. 70-48, 1970.
5. McGowan, J.J., III.; and Davis, R.T.: "Development of a Numerical Method to Solve the Three-Dimensional Compressible Laminar Boundary-Layer Equations with Application to Elliptical Cones at Angle of Attack." ARL 70-0341, December 1970.
6. Ferri, A.: "Some Heat Transfer Problems in Hypersonic Flow," Aeronautics and Astronautics, N.J. Hoff and W.G. Vincenti, editors. New York, Pergamon Press, 1960, pp. 344-377.
7. Mayne, A.W., Jr.; and Adams, J.C., Jr.: "Streamline Swallowing by Laminar Boundary Layers in Hypersonic Flow." Arnold Engineering Development Center, TR-71-32. Arnold Air Force Station, Tennessee, March 1971.
8. Dwyer, H.A.: "Solution of a Three-Dimensional Boundary-Layer Flow with Separation." AIAA Journal, Vol. 6, No. 7, 1968.
9. Krause, E.: "Comment on Solution of a Three-Dimensional Boundary-Layer Flow with Separation". AIAA Journal, Vol. 7, No. 3, 1968.
10. Der, Joe, Jr.: "A Study of General Three-Dimensional Boundary-Layer Problems by an Exact Method." AIAA Paper No. 69-138, 1969.
11. Richtmyer, R.D.: Difference Methods for Initial-Value Problems. Interscience Publishers, Inc., New York, 1957.

12. Mayne, A.W., Jr.: "Analysis of Laminar Boundary Layers on Right Circular Cones at Angle of Attack; Including Streamline-Swallowing Effects." AEDC-TR-72-134, October 1972.
13. Lewis, C.H.; and Whitfield, J.D.: "Theoretical and Experimental Studies of Hypersonic Viscous Effects." AEDC-TR-65-100, May 1965.
14. Jones, D.J.: "Tables of Inviscid Supersonic Flow About Circular Cones at Incidence, $\gamma = 1.4$." AGARDOGRAPH 137, Part I and II.
15. Bazzhin, A.P.: "Some Results of Calculations of Flows Around Conical Bodies at Large Incidence Angles." Proc. of the Second Int. Conf. on Numerical Methods in Fluid Dynamics, Sep. 15-19, 1970, Berkeley, Springer-Verlag, 1971.
16. Stone, A.H.: "On Supersonic Flow Past a Slightly Yawing Cone." Part I, J. Math. and Phys., 27, 1, pp. 67-81, April 1948.
17. Stone, A.H.: "On the Supersonic Flow Past a Slightly Yawing Cone." Part II. J. Math. and Phys., 30, P. 200, 1951.
18. Sims, J.L.: "Tables for Supersonic Flow Around Right Circular Cones at Small Angle of Attack." NASA SP-3007, 1964.
19. Moretti, G.: "Inviscid Flow Field Past a Pointed Cone at an Angle of Attack." General Applied Science Laboratory, Tech. Rep. 577, December 1965.
20. Stocker, P.M.; and Mauger, F.E.: "Supersonic Flow Past Cones of General Cross-section." J. Fluid Mech., 13, pp. 383-399, July 1962.
21. Babenko, K.I.; Voskresenskiy, G.P.; Lyubimov, A.N.; and Rusanov, V.V.: "Three-Dimensional Flow of Ideal Gas Past Smooth Bodies." NASA, TT F-380, April 1966.
22. Jones, D.L.: "Numerical Solutions of Flow Field for Conical Bodies in a Supersonic Stream." Aeronautical Rept. LR-507, National Research Council of Canada, July 1968.
23. Tracy, R.R.: "Hypersonic Flow Over a Yawed Circular Cone." Memo. 69, Graduate Aeronautical Laboratories, California Institute of Technology, August 1963.

24. Moore, F.K.: "Laminar Boundary Layer on Cone in Supersonic Flow at Large Angle of Attack." NACA, Rep. 1132, 1953.
25. Moore, F.K.: "Laminar Boundary Layer on Cone in Supersonic Flow at Large Angle of Attack." NACA TN 2844, 1952.
26. Cheng, H.K.: "The Shock Layer Concept and Three-Dimensional Hypersonic Boundary Layers." Cornell Aero. Lab. Rept. No. AF-1285-A-3, 1961.
27. Vvedenskaya, N.D.: "Calculation of the Boundary Layer Arising in a Flow About a Cone Under an Angle of Attack." Zh. vychisl. Mat. mat. Fizl. 6, 304-312, 1966.
28. Libby, P.A.: "Heat and Mass Transfer at a General Three-Dimensional Stagnation Point." AIAA J. 5, 507-517, 1967.
29. Libby, P.A.; and Liu, T.M.: "Some Similar Laminar Flows Obtained by Quasi-linearization." AIAA J. 6, 1541-1548, 1968.
30. Dwyer, H.A.: "Boundary Layer on a Hypersonic Sharp Cone at Small Angle of Attack." AIAA J. 9, 277-284, 1971.
31. Murdoch, J.W.: "The Solutions of Sharp Cone Boundary Layer Equations in the Plane-of-Symmetry." Aerospace Rept. MOTR-0172 (S2816-60)-1, The Aerospace Corporation, San Bernadino Operations, July 15, 1971.
32. Rakich, T.V.: "A Method of Characteristics for Steady Three-Dimensional Supersonic Flow with Application to Inclined Bodies of Revolution, NASA TND-5341, Oct. 1969.
33. Vatsa, V.N.; and Davis, R.T.: "The Use of Levy-Lees Variables in Three Dimensional Boundary Layer Flows," to appear as a NASA Contractor's report.

TABLE I. CONDITIONS OF COMPUTED SHARP CONE CASES

Case	M_∞	$\phi_c (^\circ)$	T_w/T_o	R_e	$\alpha (^\circ)$
1	8	10	.46	4.04×10^4	8
2	8	10	.46	4.04×10^6	8
3	8	10	.46	4.04×10^4	10
4	8	10	.46	4.04×10^5	10
5	8	10	.46	4.04×10^4	12
6	8	25	.46	4.04×10^4	12.5

TABLE II. COMPUTED SHARP CONE PARAMETERS AT $\alpha = 0^\circ$

Case	M_∞	$\phi_c(o)$	$\alpha(o)$	T_w/T_o	$C_{f_\xi} \sqrt{xRe}$	$\bar{q}_w / (\rho u^3)_\infty \sqrt{xRe}$
1	8	10	0	.46	0.39925	-.05537
2	8	25	0	.46	.71229	-.11582

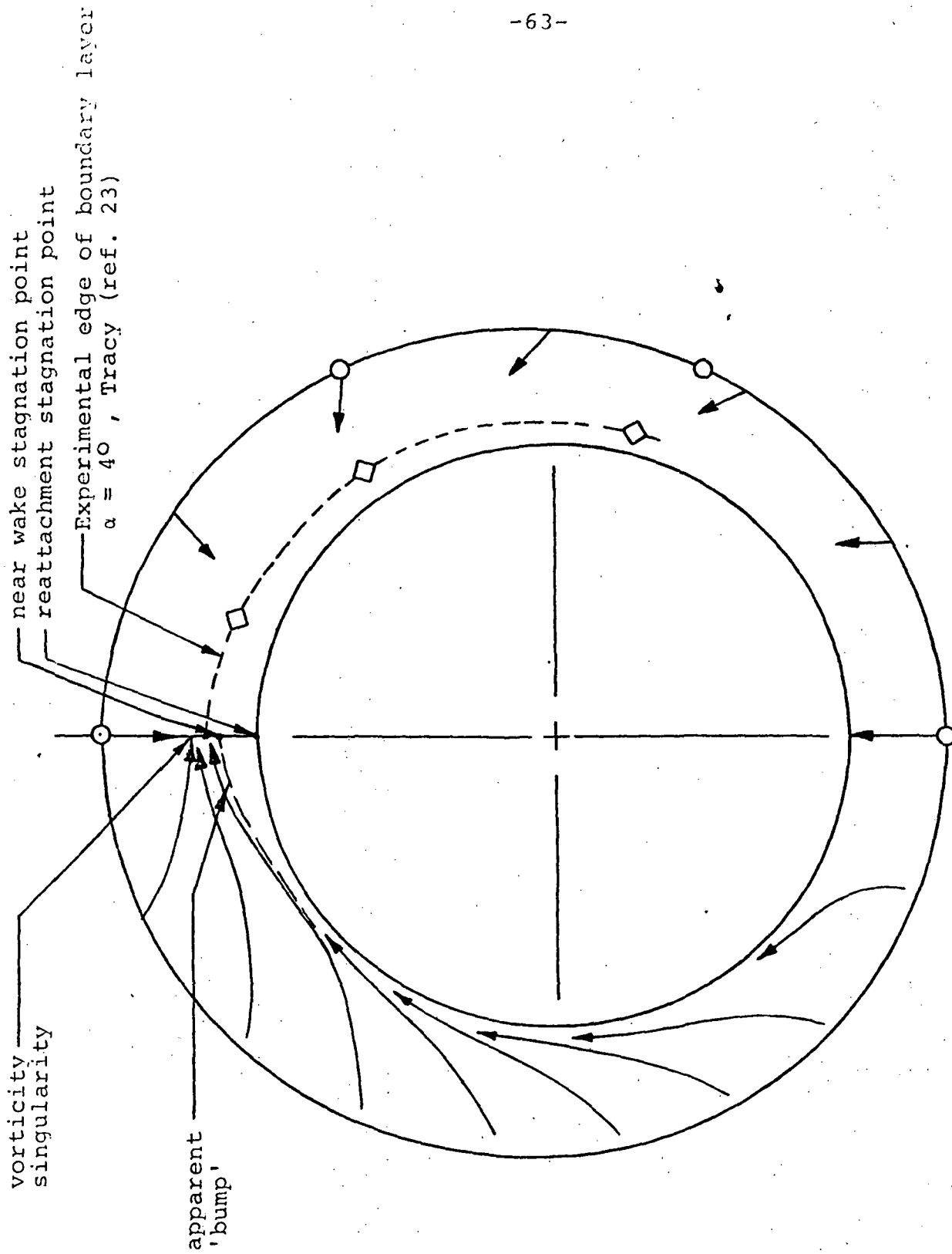


Figure 1.1 Streamline pattern about a sharp circular cone

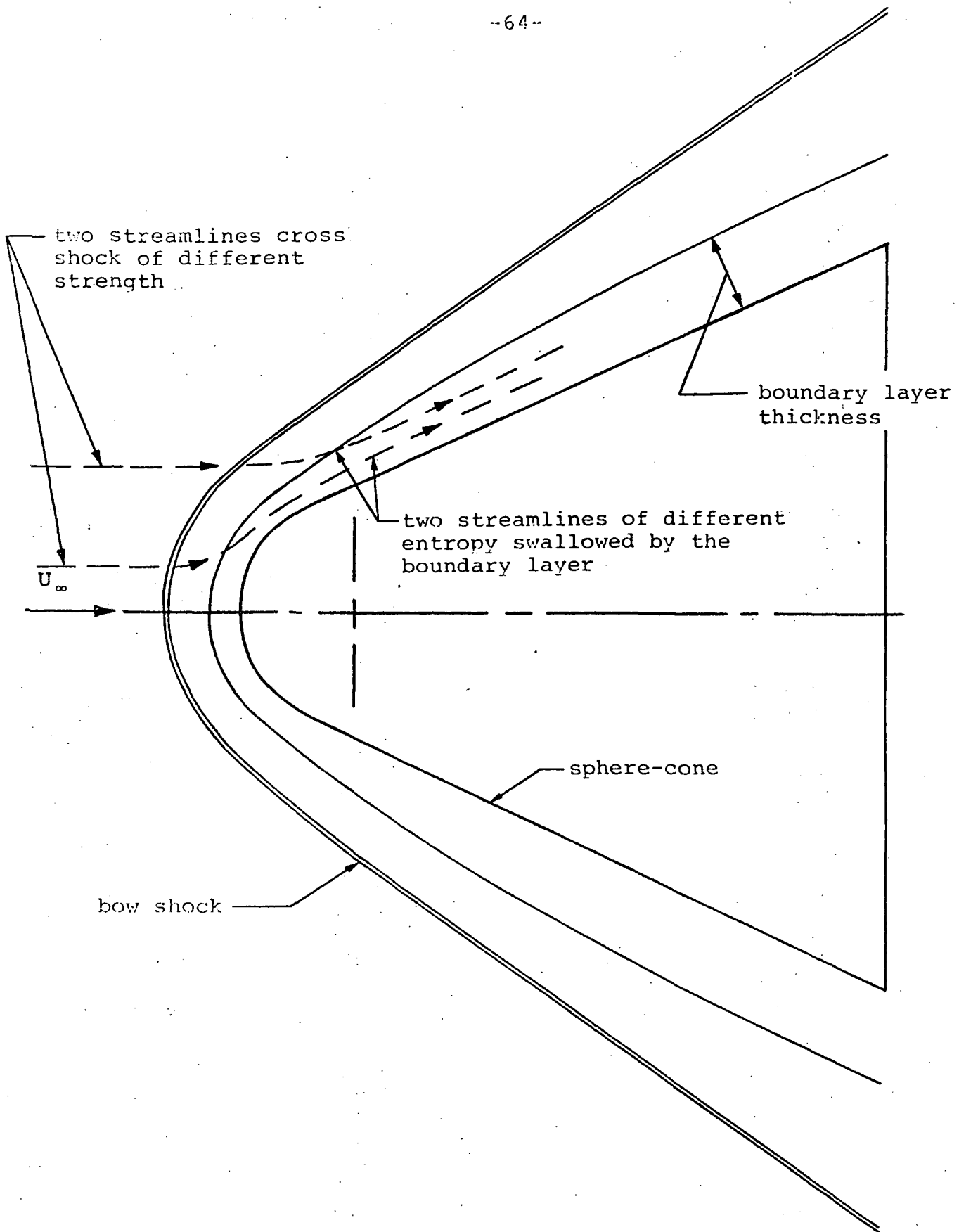


Figure 1.2 Streamline swallowing on a sphere-cone at zero angle of attack

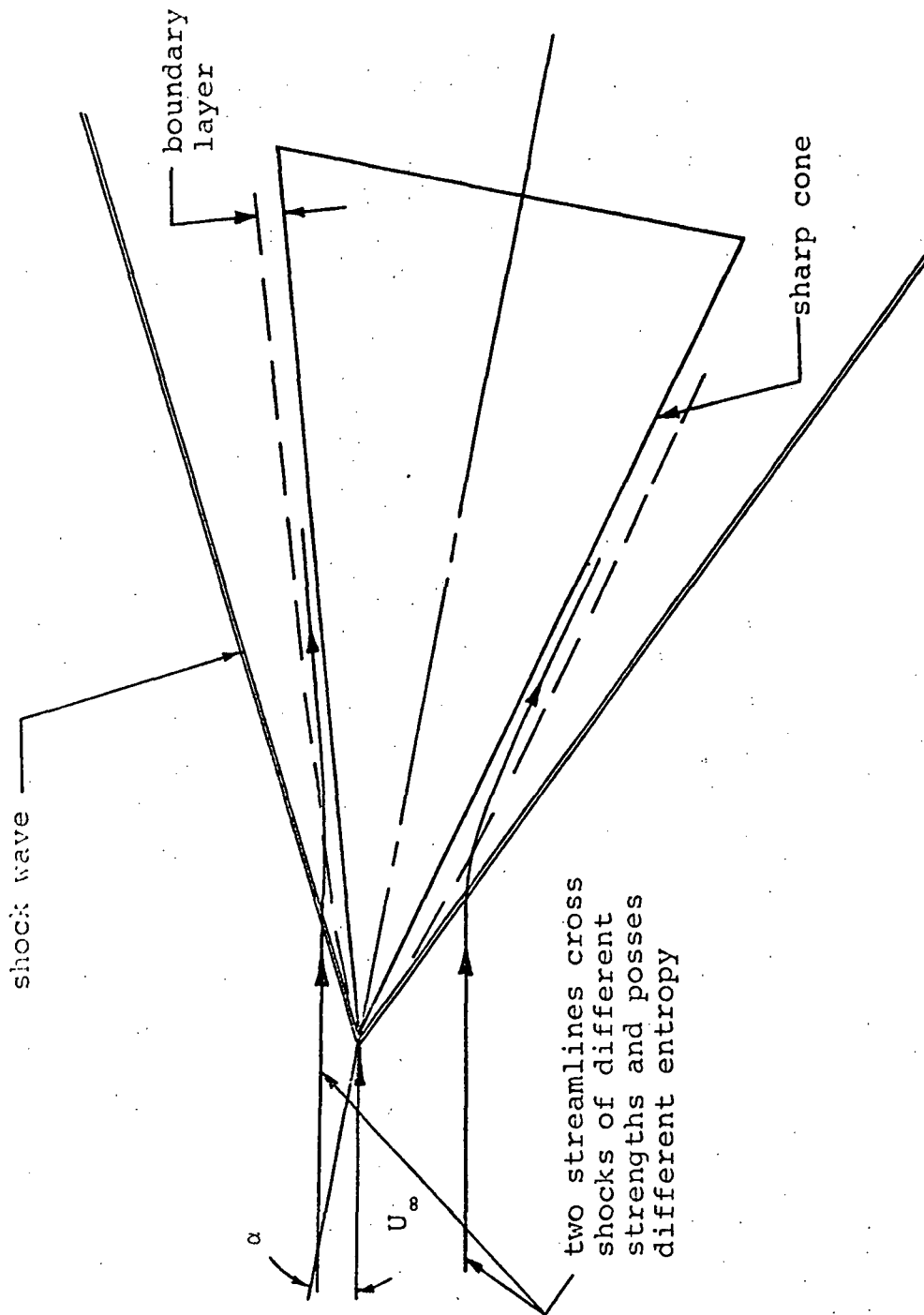
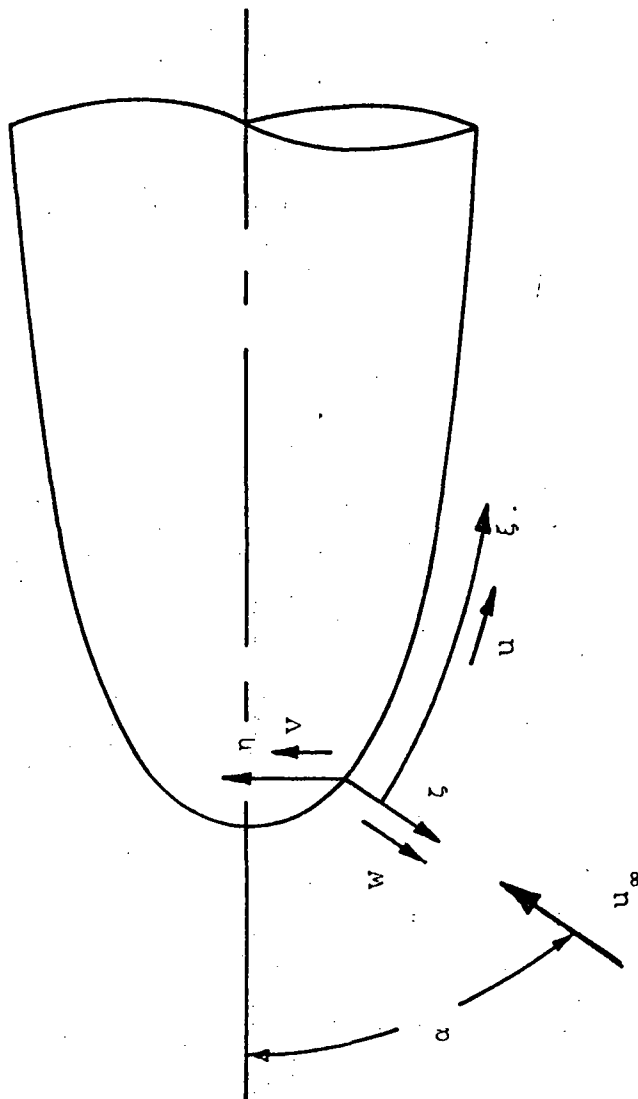


Figure 1.3 Streamline swallowing on a sharp cone
at angle of attack



$$\begin{aligned} d\bar{s}_1 &= \bar{h}_1 d\xi \\ d\bar{s}_2 &= \bar{h}_2 d\eta \\ d\bar{s}_3 &= \bar{h}_3 dz \end{aligned}$$

Figure 2.1 Coordinate system

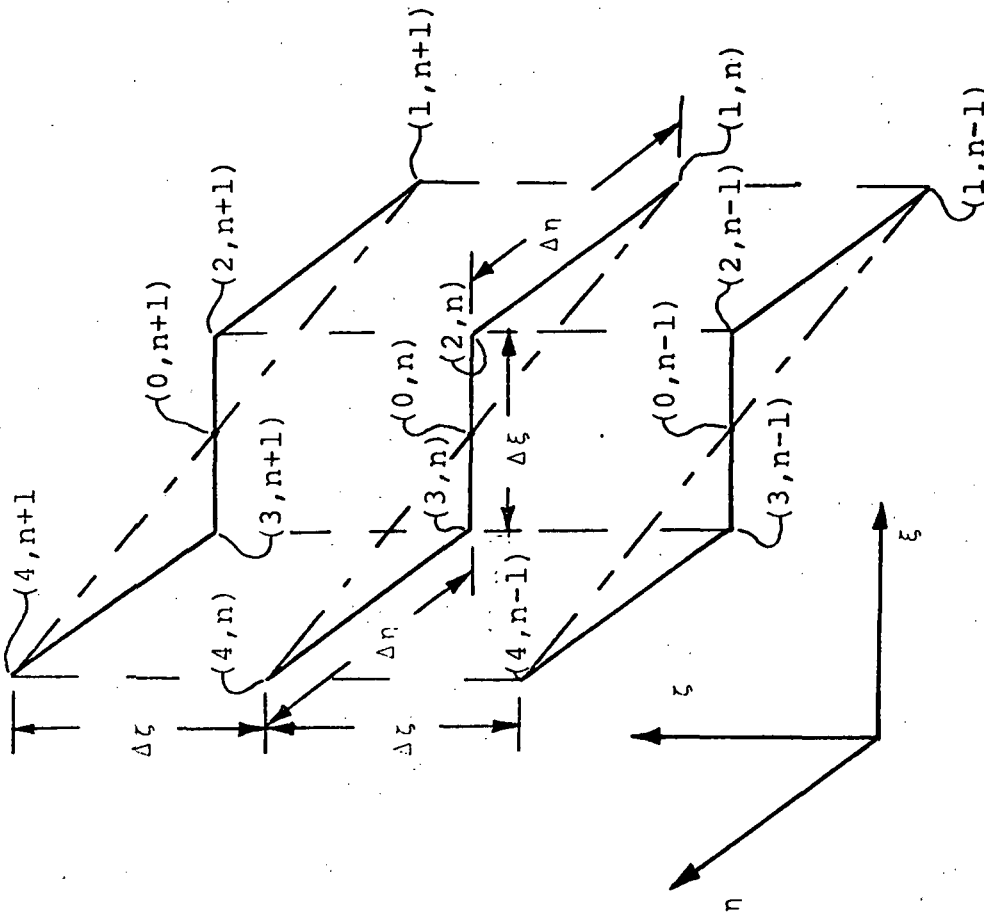


Figure 3.1a Finite-difference scheme used
in the general case

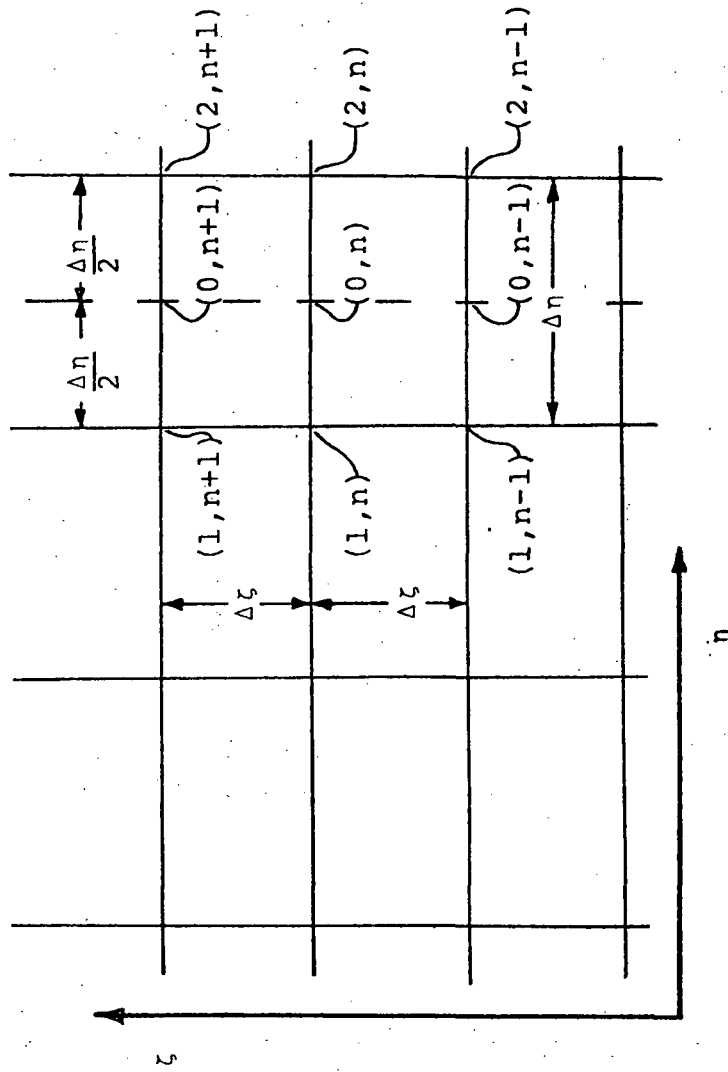


Figure 3.1b Finite-difference scheme used in the case of similarity in the ξ -direction

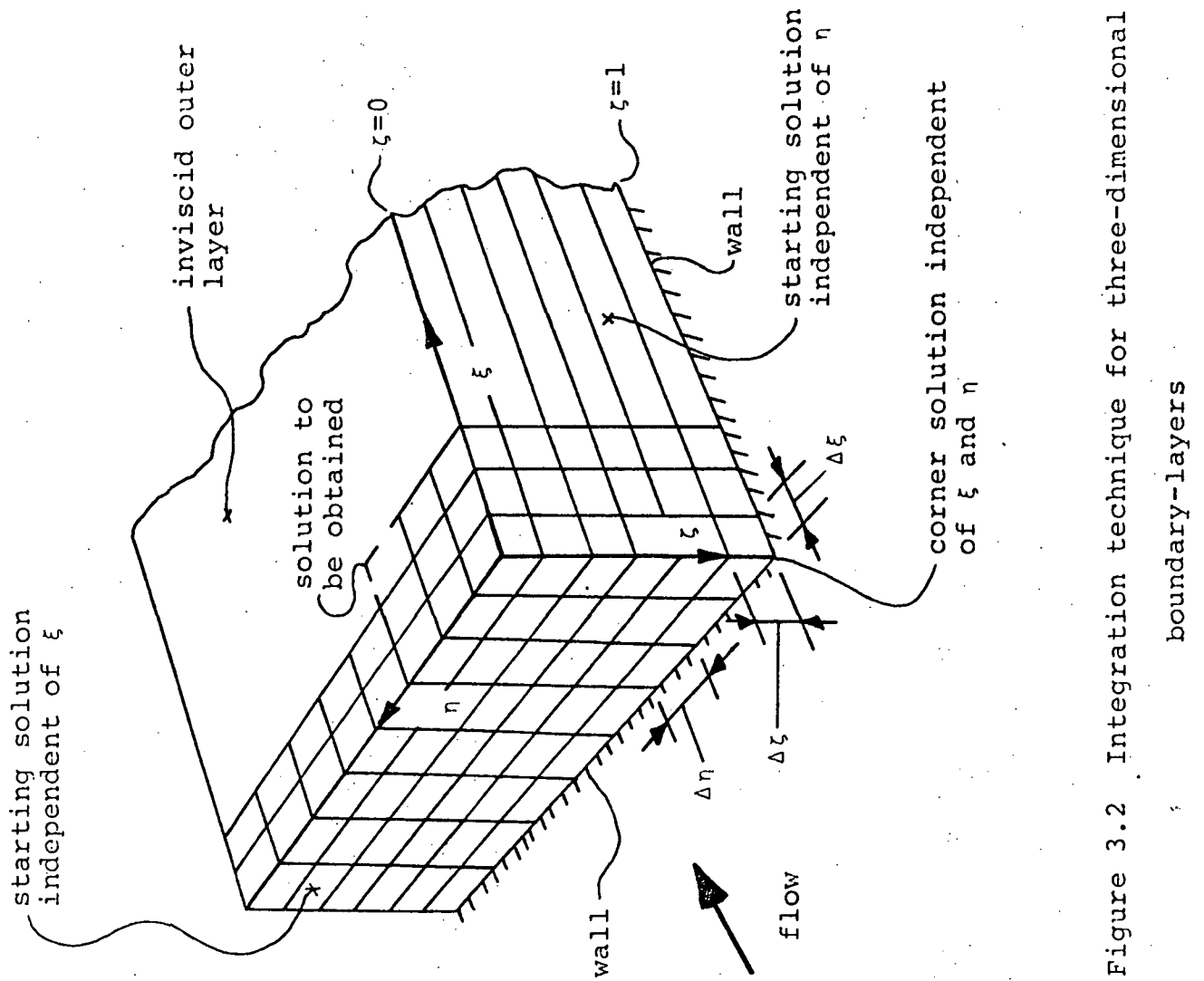


Figure 3.2 Integration technique for three-dimensional boundary-layers

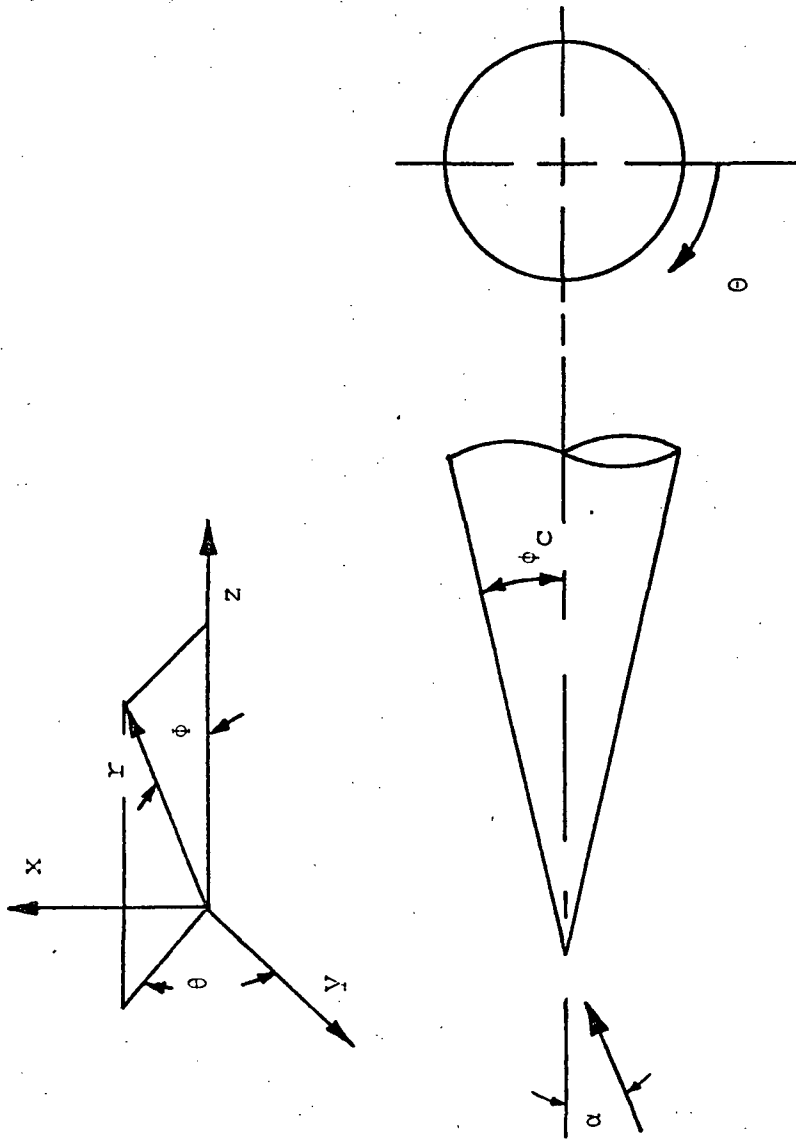


Figure 4.1. Geometry of the circular cone

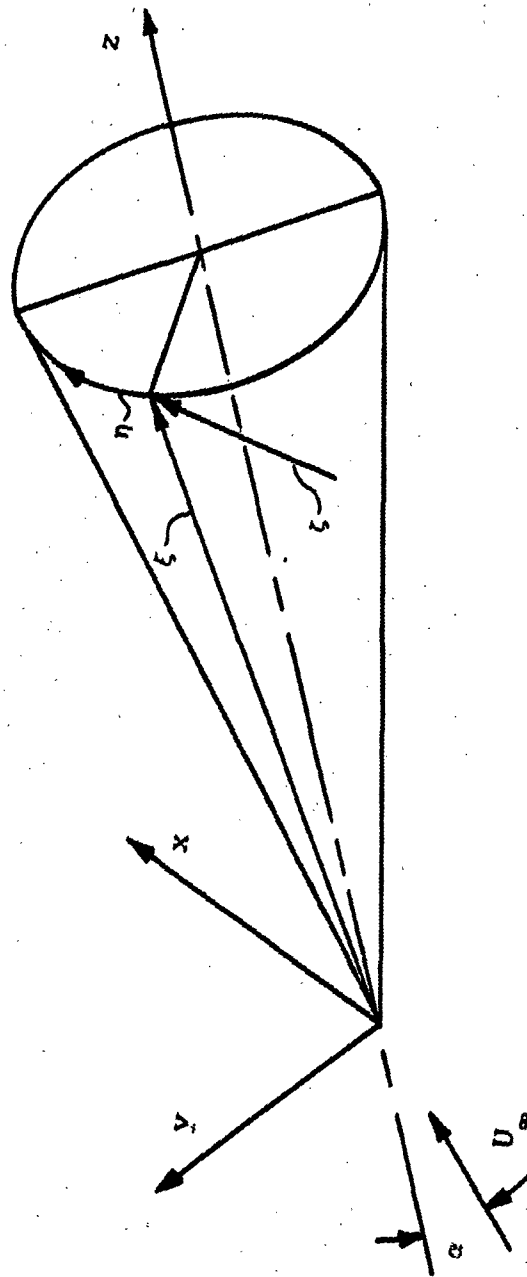
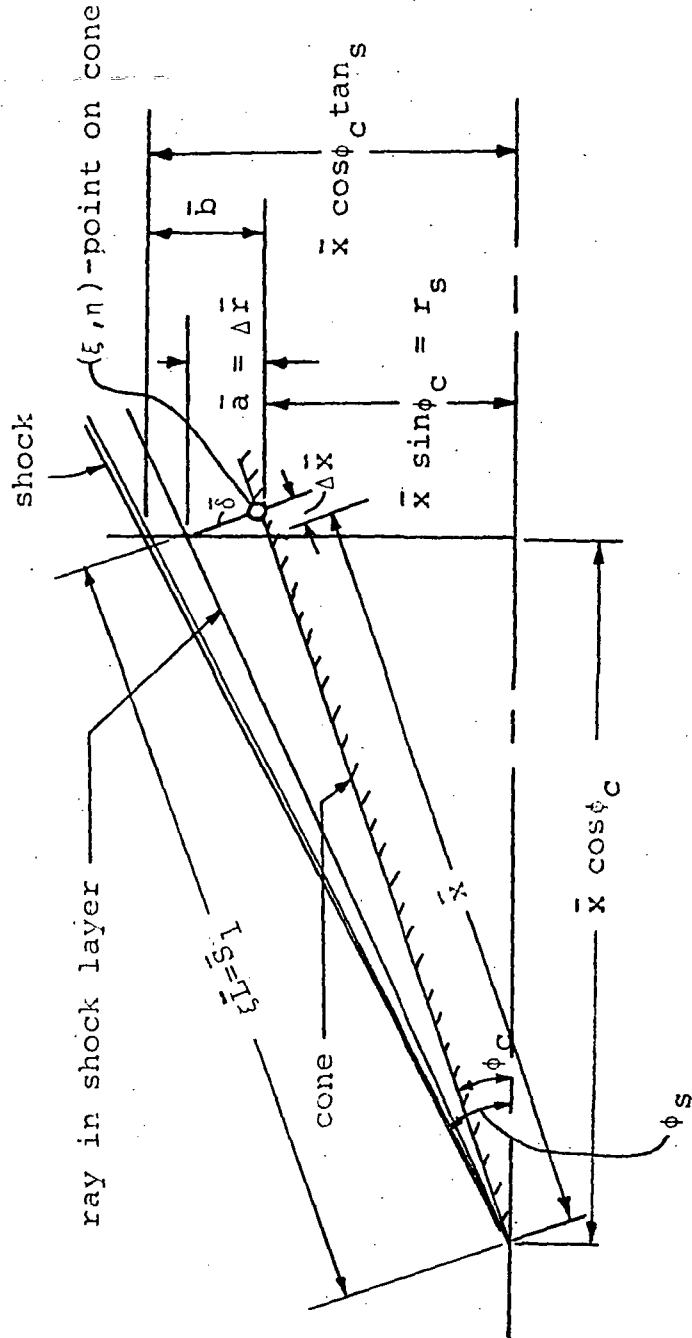


Figure 4.2 Coordinate system for conical flow



$$\Delta \bar{x} = \bar{\delta} \tan \phi_C$$

$$\Delta \bar{r} = \bar{\delta} / \cos \phi_C$$

$$\bar{x} = \bar{S}_1 - \bar{\delta} \tan \phi_C$$

$$\bar{\xi} = \frac{\bar{a}}{\bar{b}} = \frac{\Delta \bar{r}}{\bar{x} (\tan \phi_S - \tan \phi_C) \cos \phi_C}$$

$$\bar{\xi} = \frac{\bar{\delta} / \cos^2 \theta_C}{(\bar{\xi} \bar{L} - \bar{\delta} \tan \phi_C) (\tan \phi_S - \tan \phi_C)}$$

Figure 4.3 Shock-body geometry for a cone

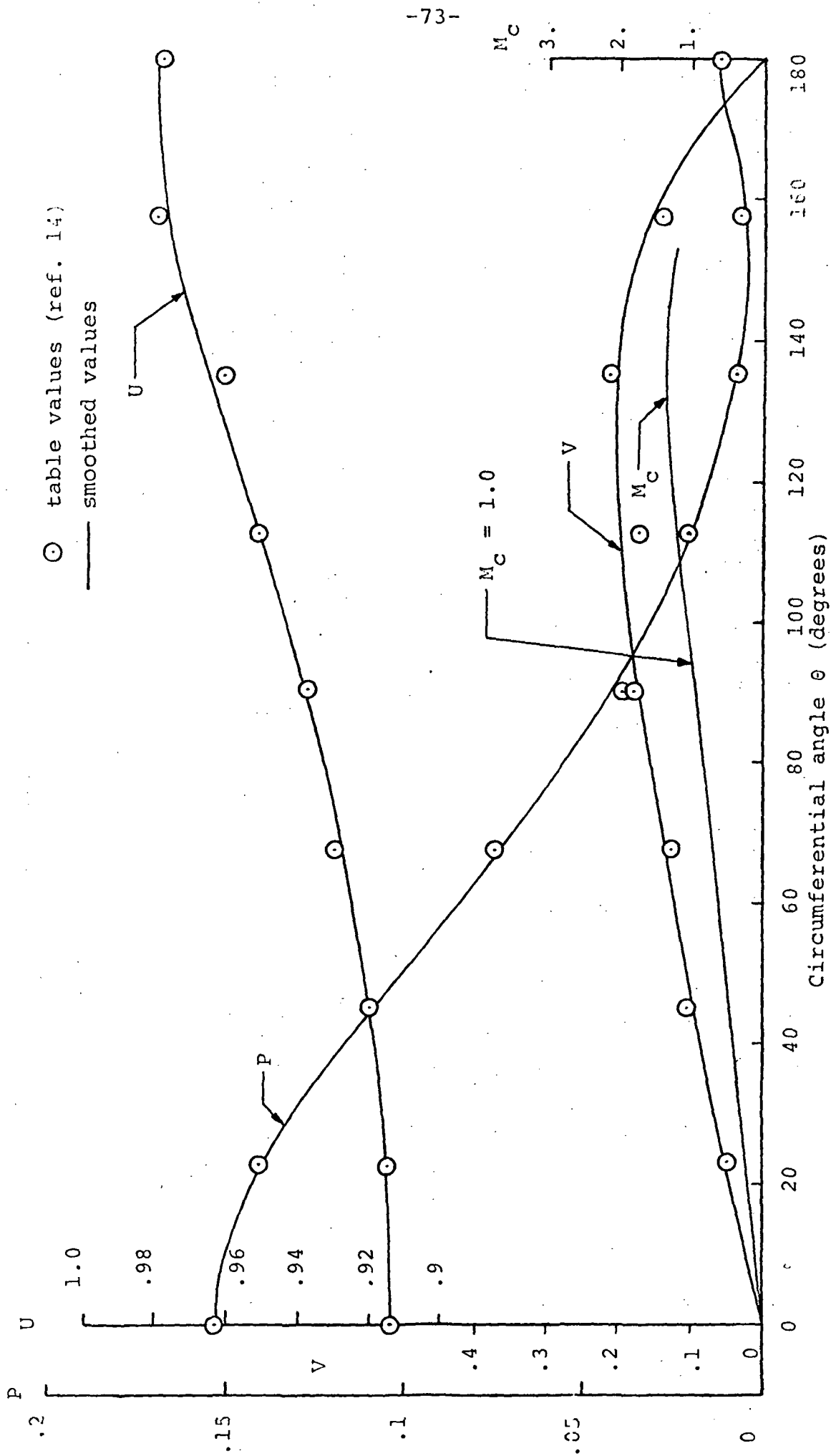


Figure 4.4 Flow variables for a sharp circular cone for $M_\infty = 8$, $\phi_C = 10^\circ$, $\alpha = 12^\circ$

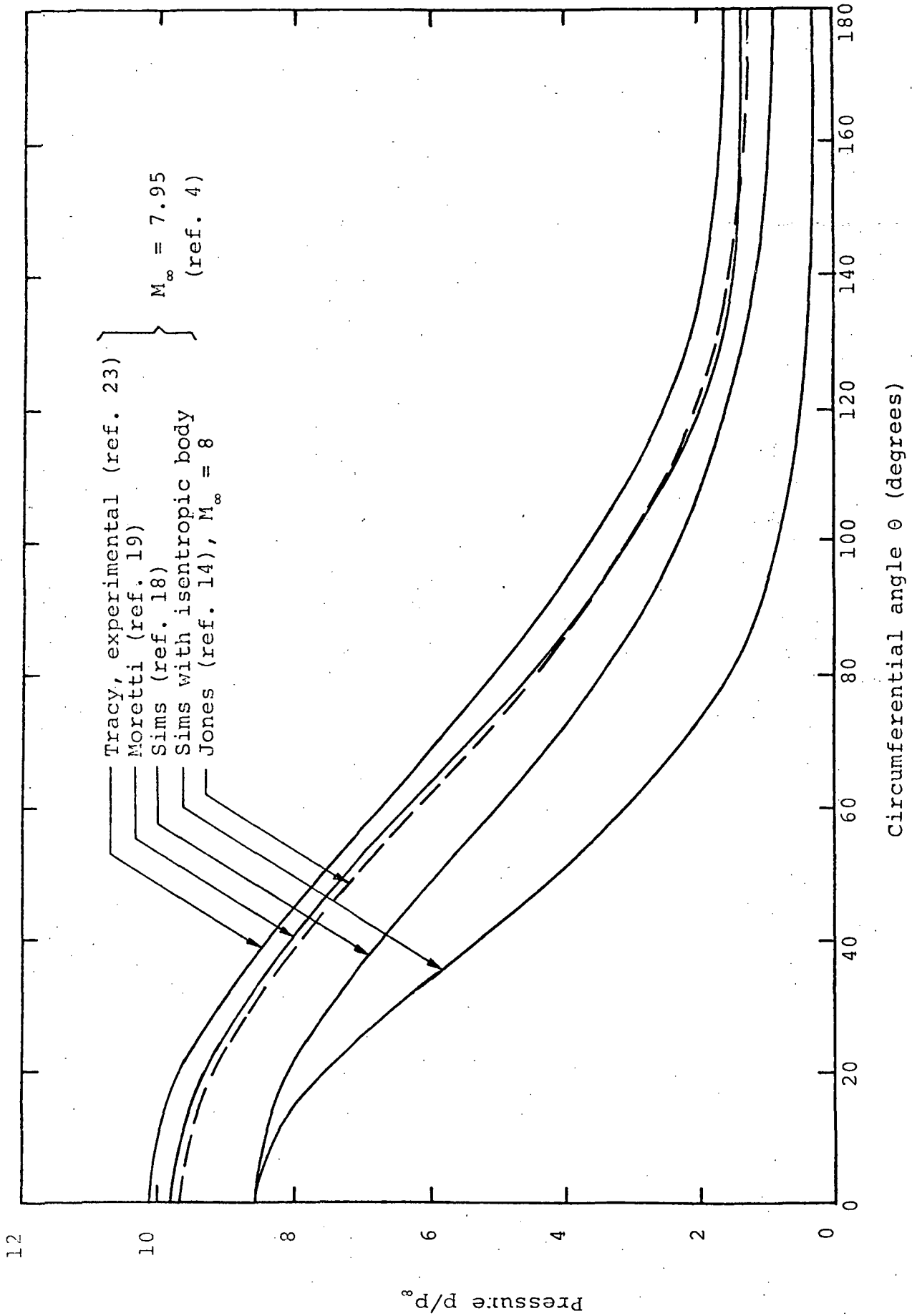


Figure 4.5 Comparison of pressure distribution on 10° sharp cone by various methods, $\alpha = 8^\circ$

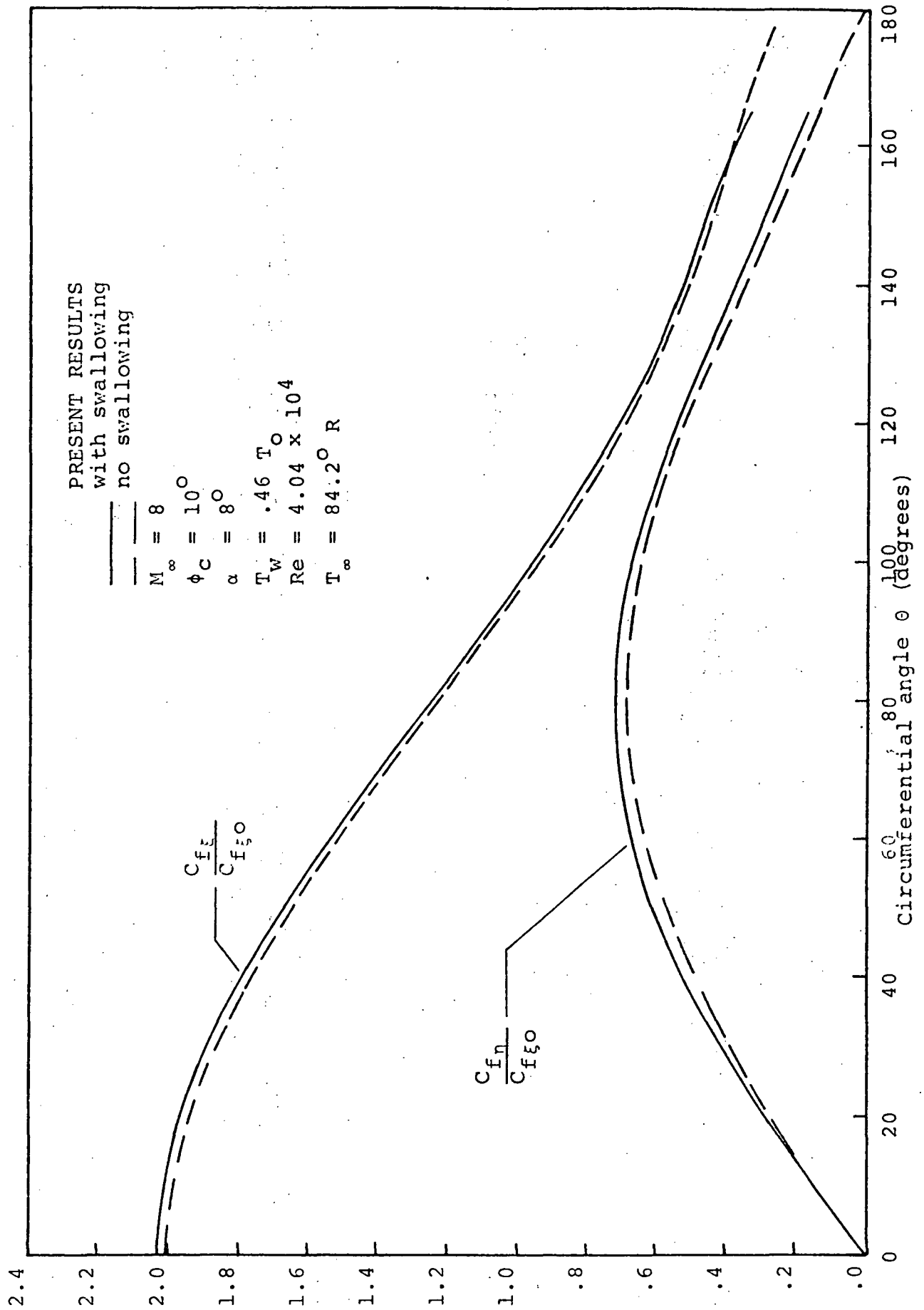


Figure 4.6 Skin friction distribution on a sharp circular cone

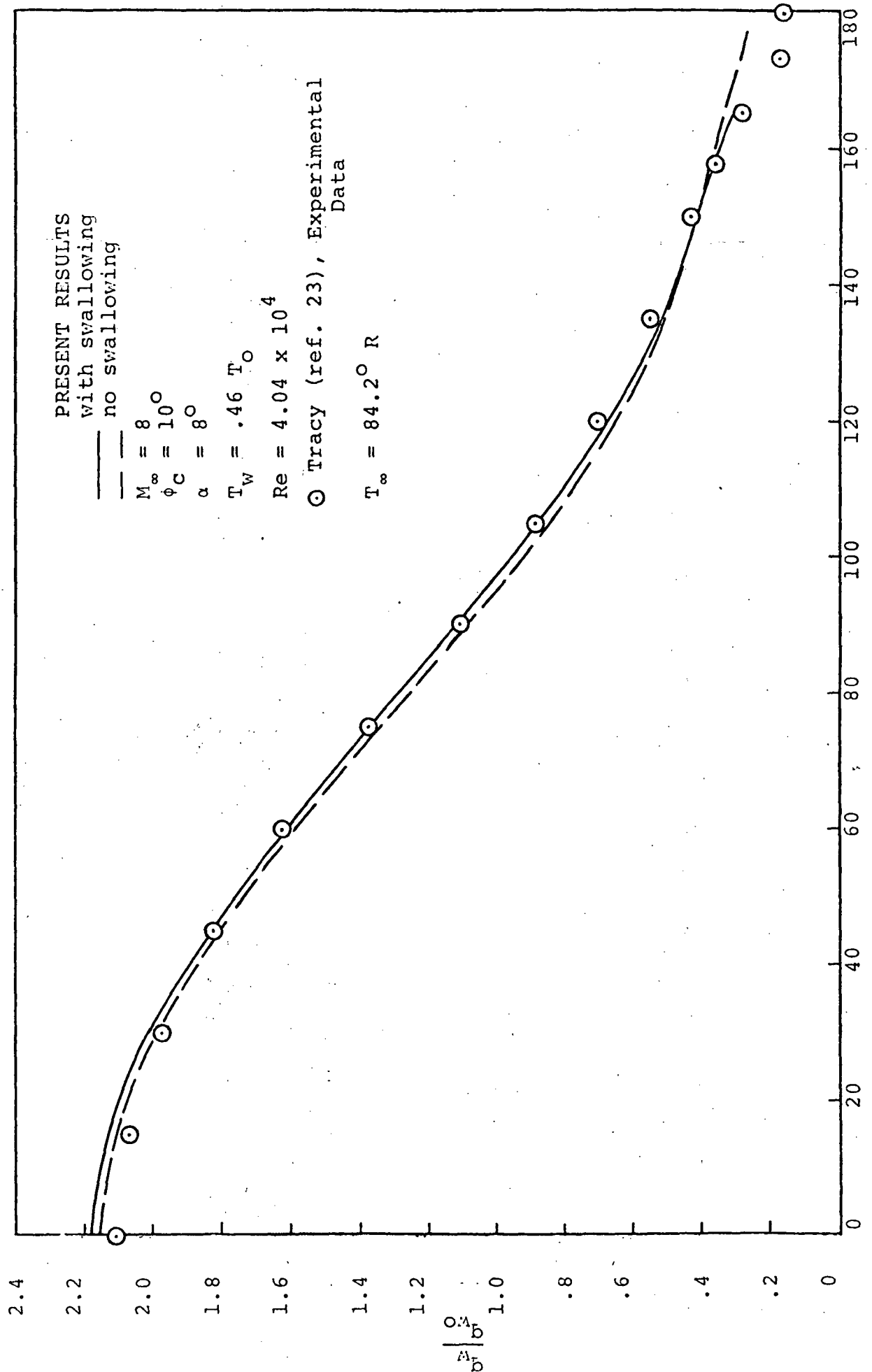


Figure 4.7 Heat transfer distribution on a sharp circular arc

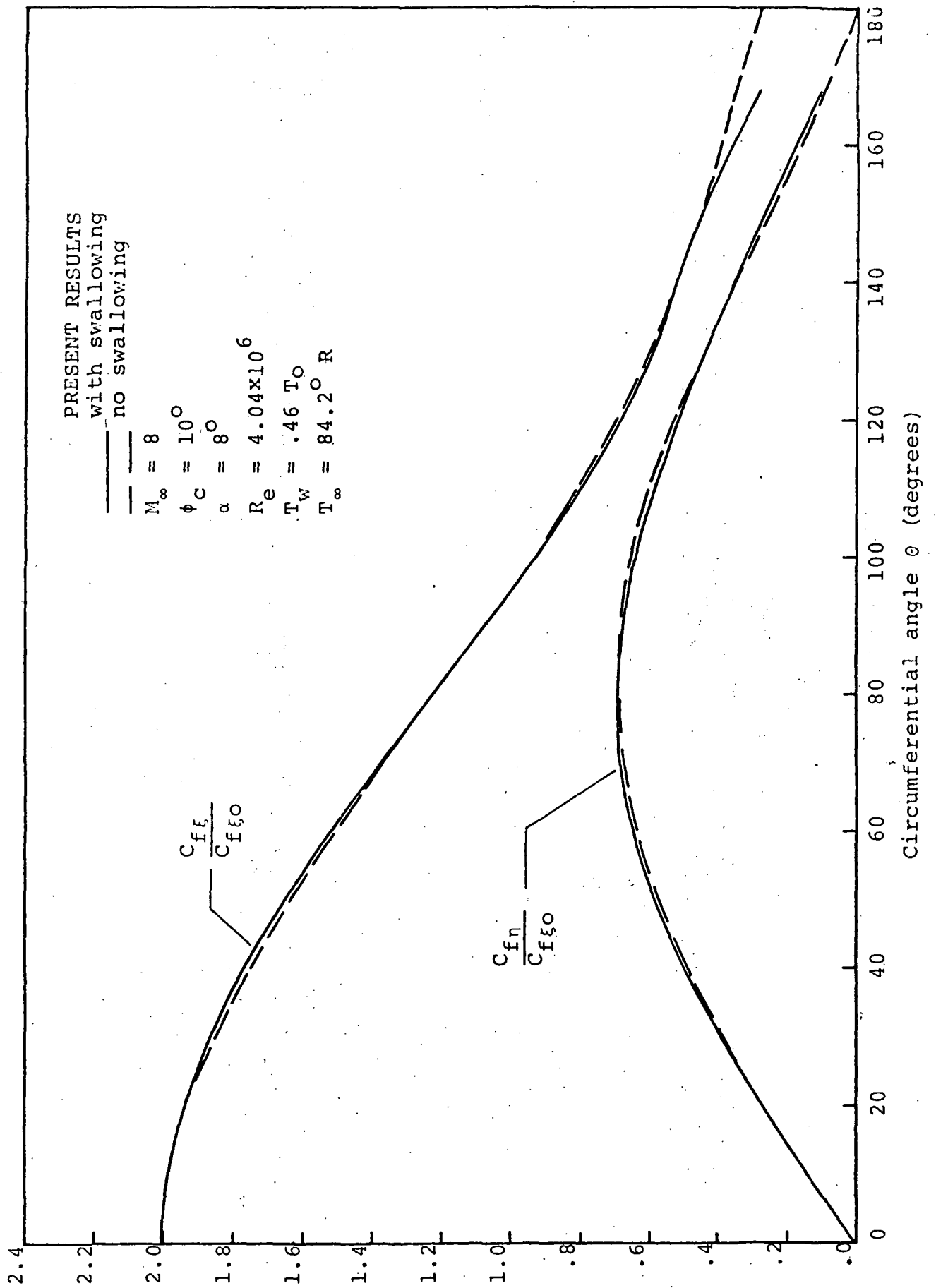


Figure 4.8 Skin friction distribution on a sharp circular cone

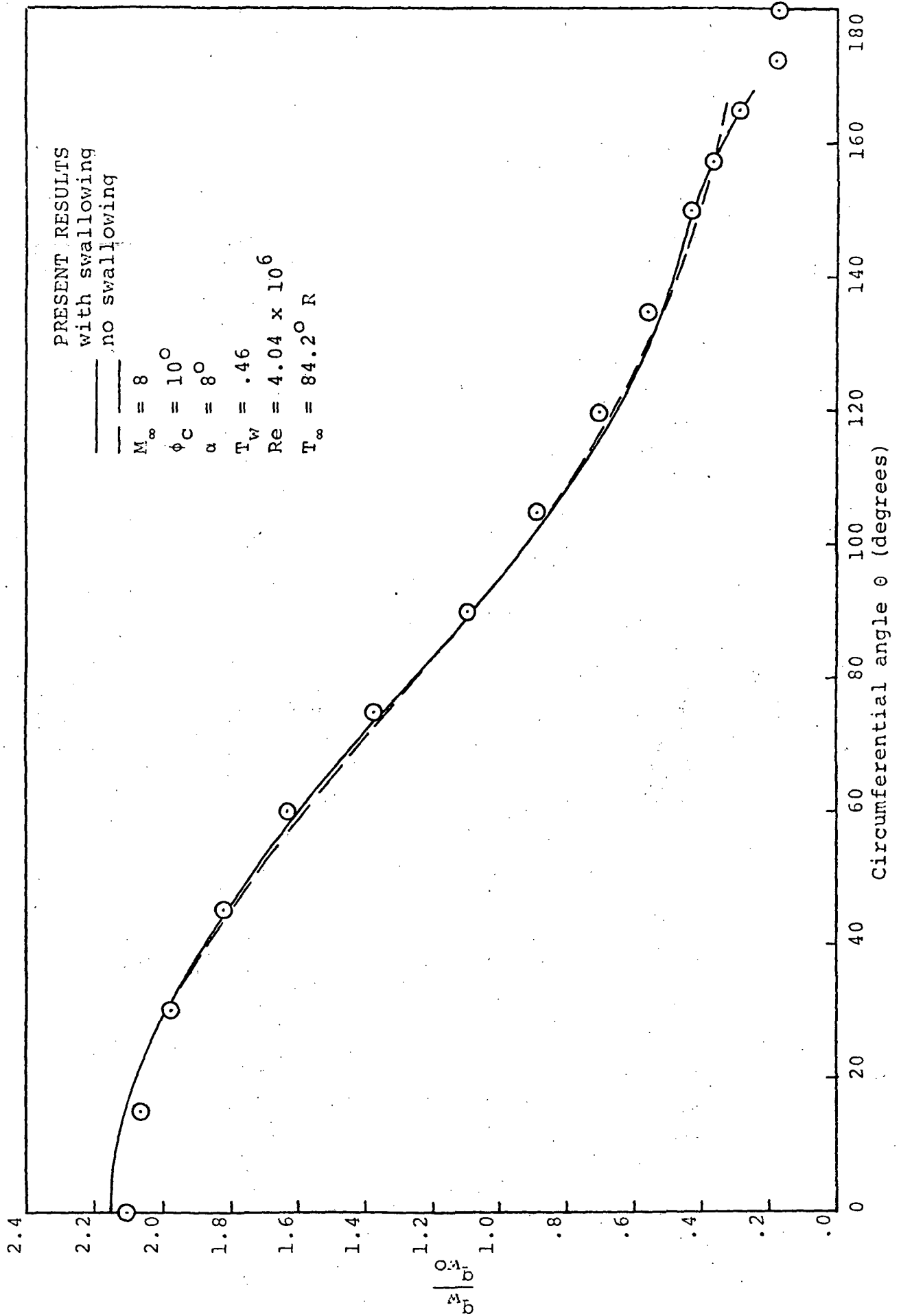


Figure 4.9 Heat transfer distribution on a sharp circular nose

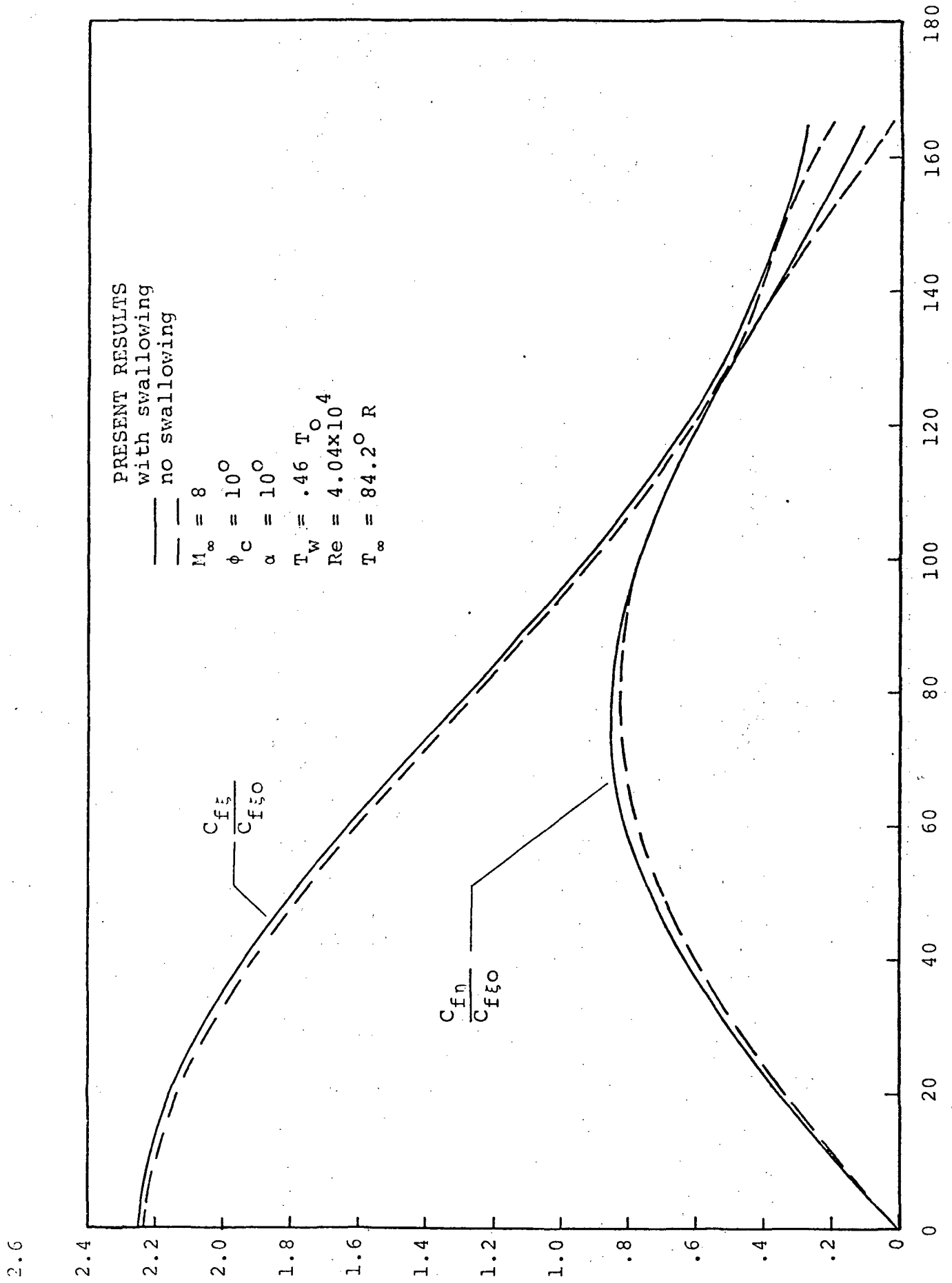


Figure 4.10 Skin friction distribution on a sharp circular cone

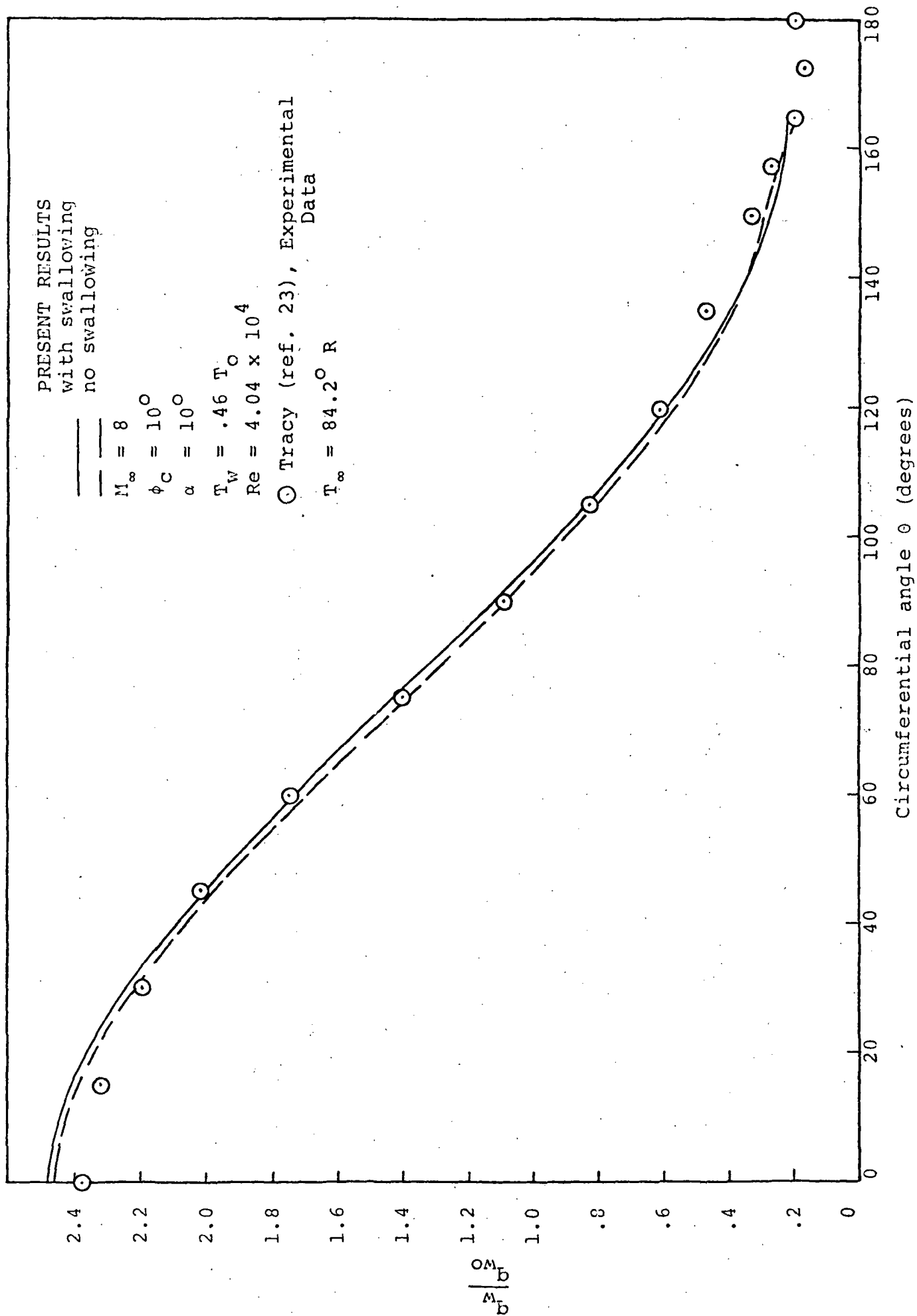


FIGURE 4.11 Heat transfer distribution

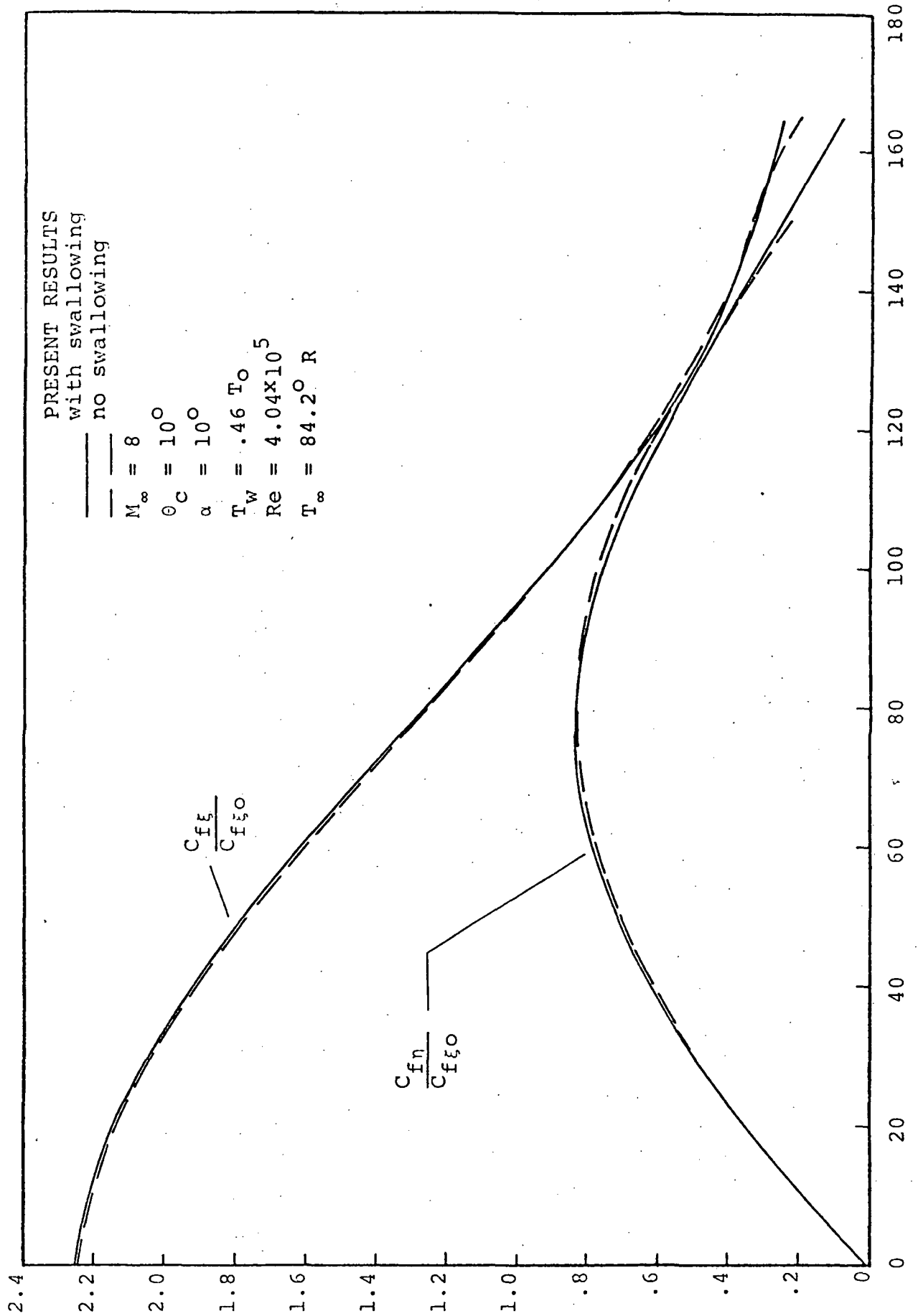


Figure 4.12 Skin friction distribution on a sharp circular cone

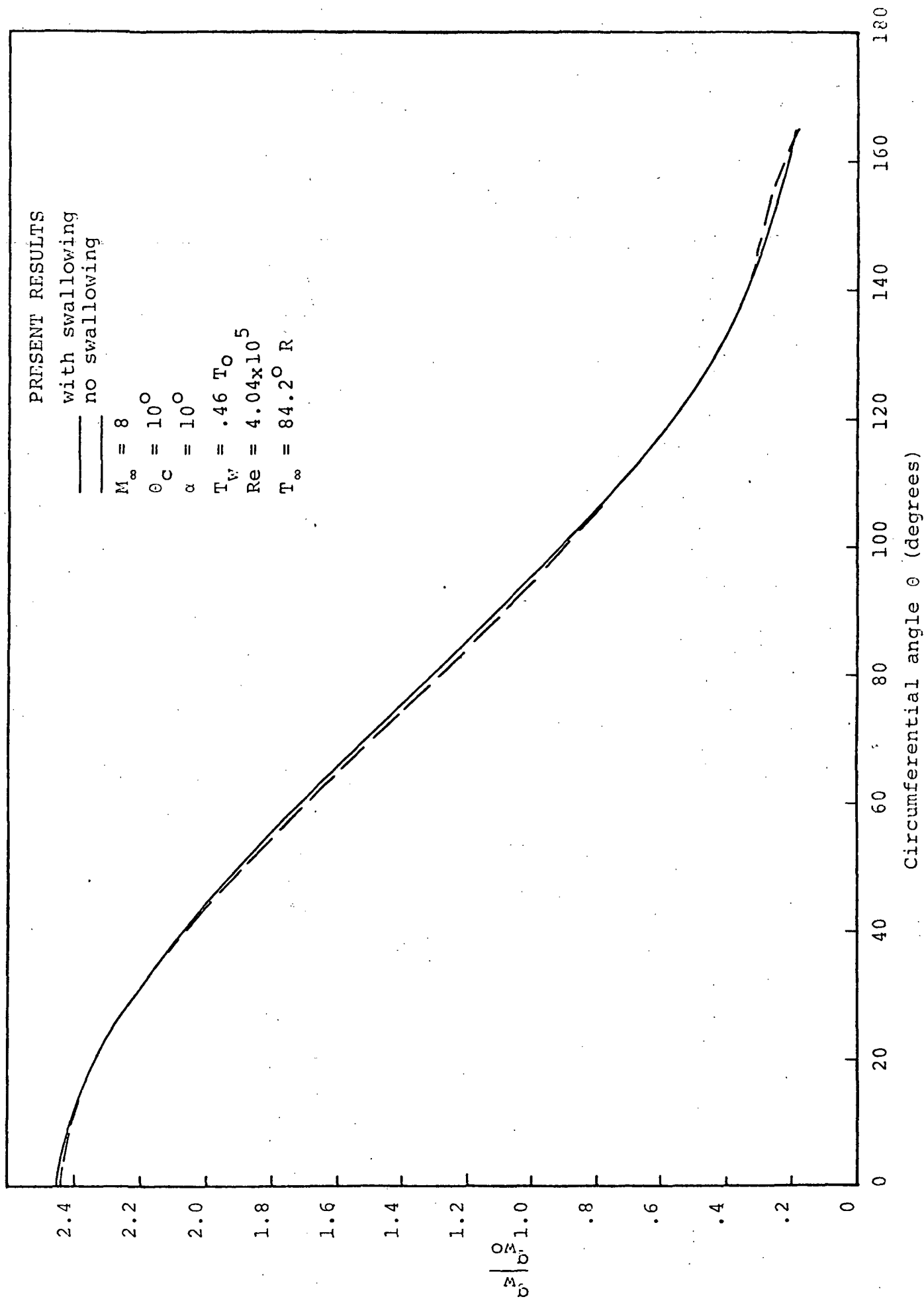


Figure 4.13 Heat Transfer Distribution on a Sharp Circular Cone

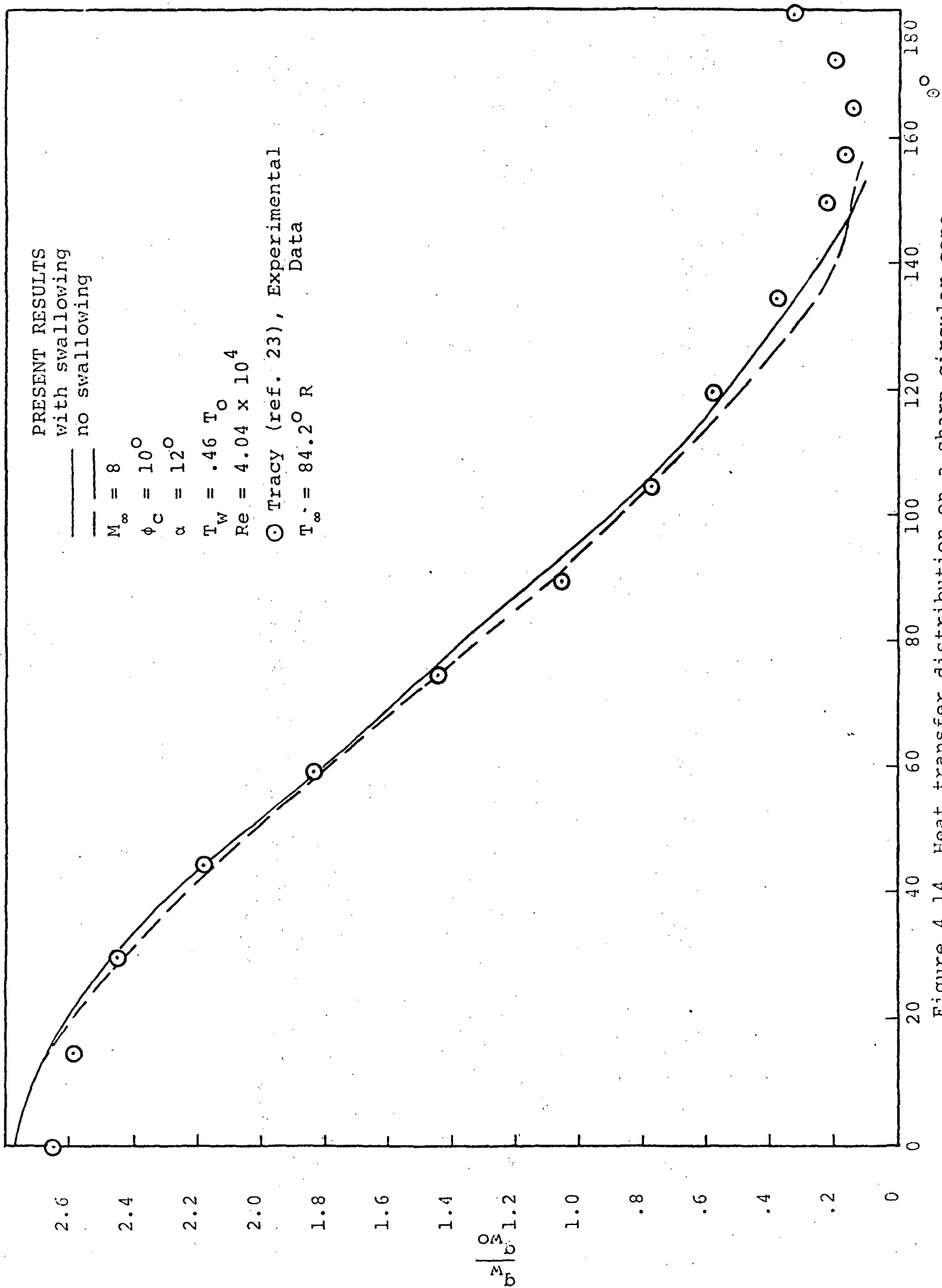


Figure 4.14 Heat transfer distribution on a sharp circular cone

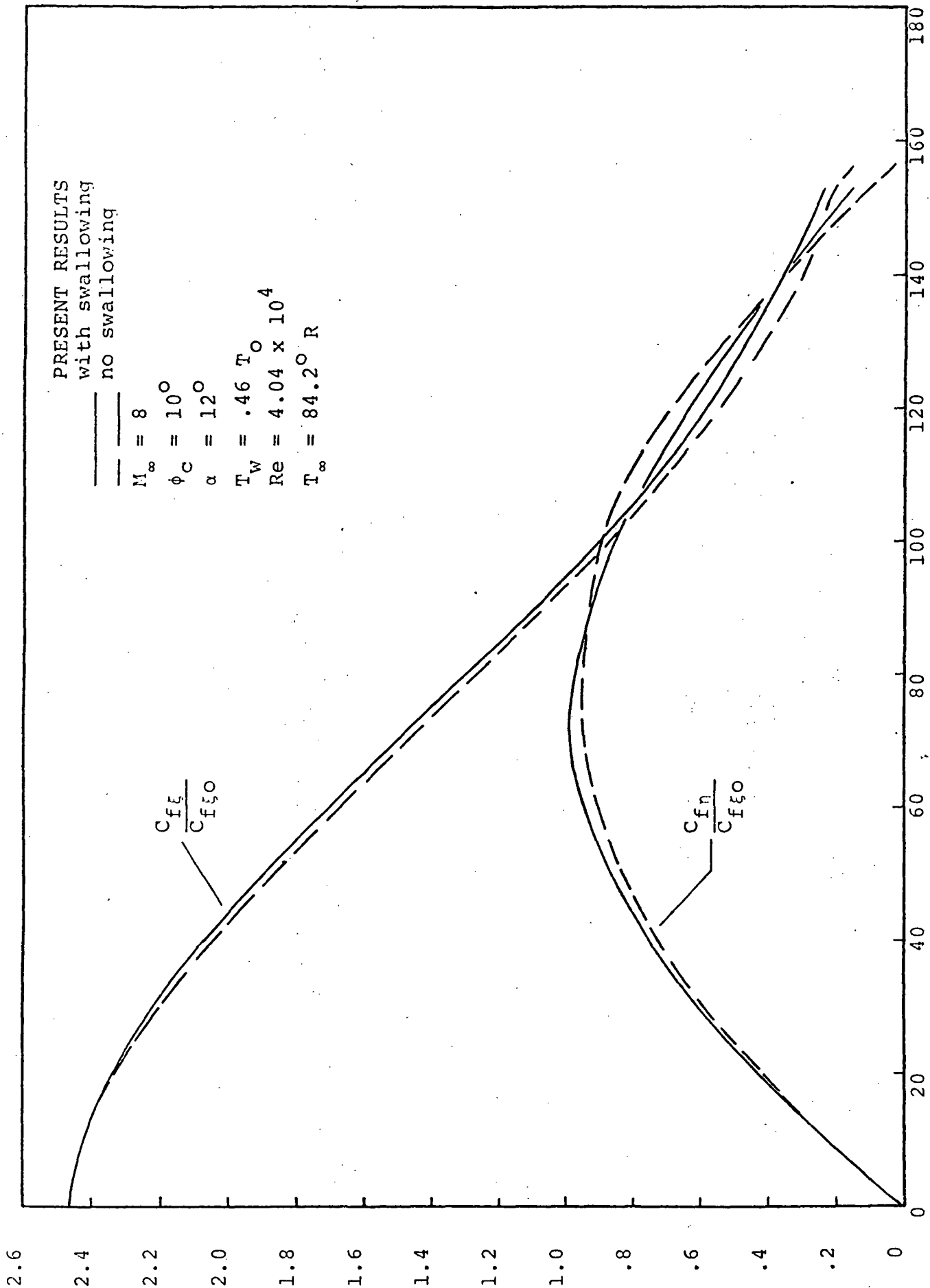


Figure 4.15 Skin friction distribution on a sharp circular cone

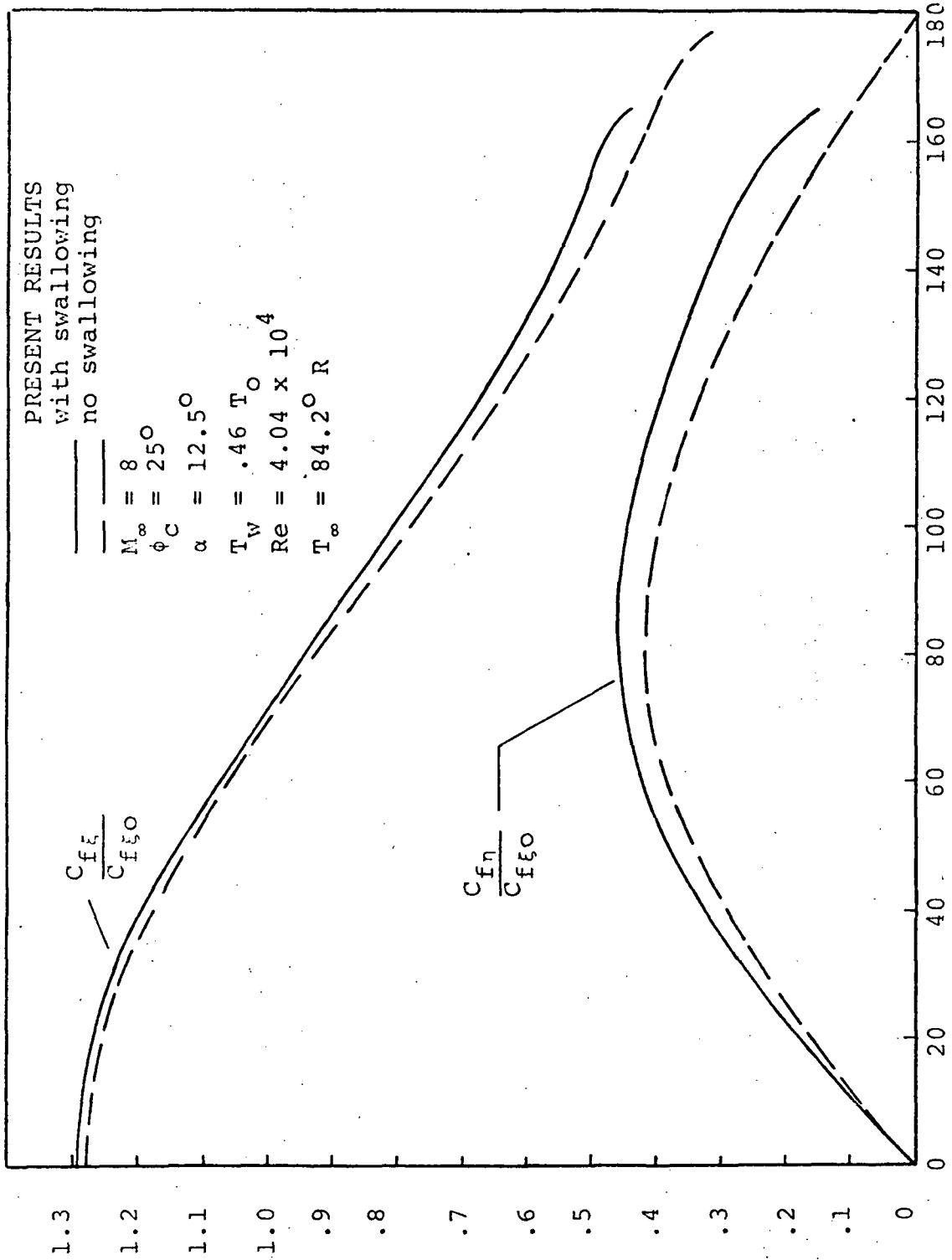


Figure 4.16 Skin friction distribution on a sharp circular cone

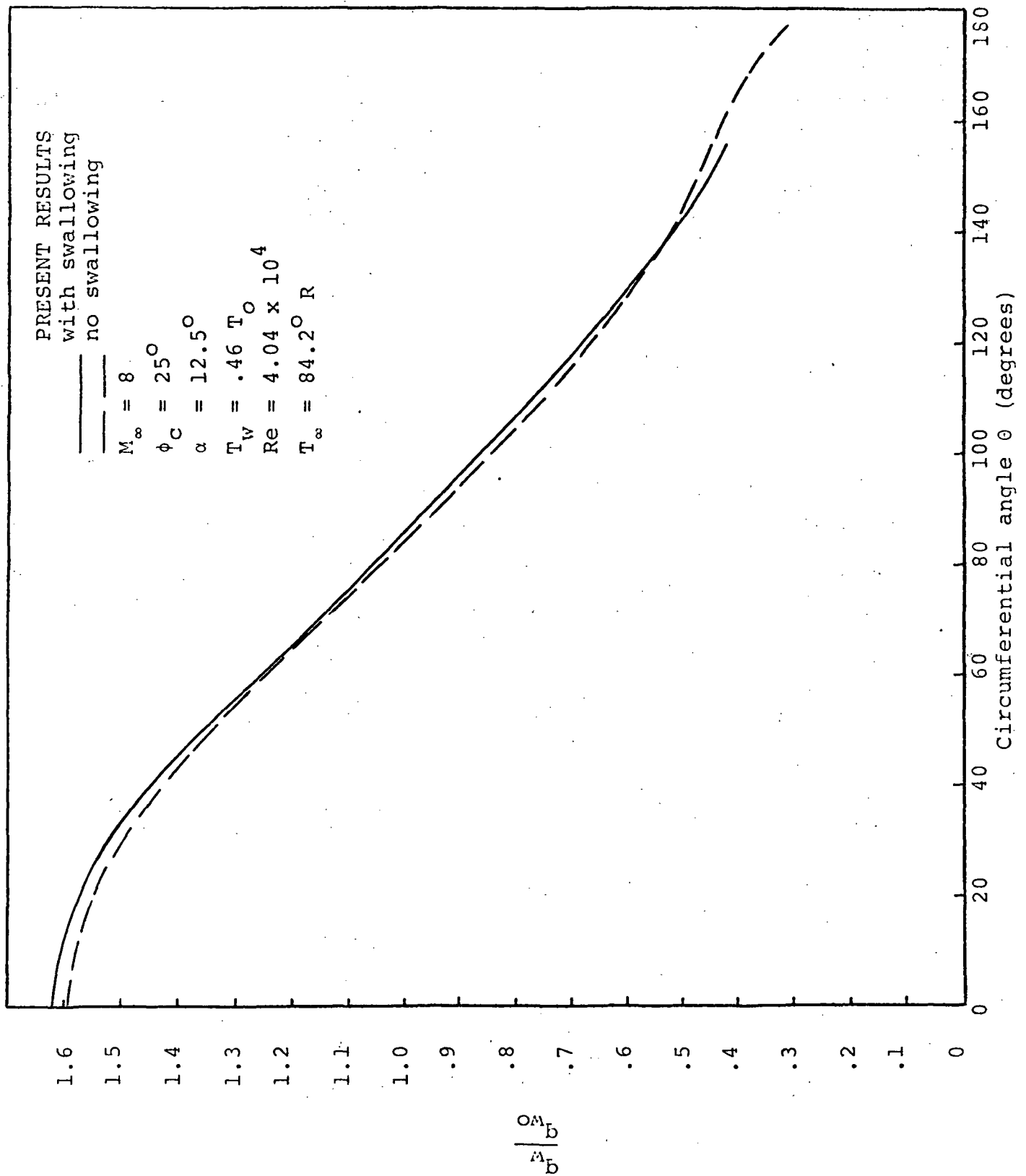


Figure 4.17 Heat transfer distribution on a sharp circular cone

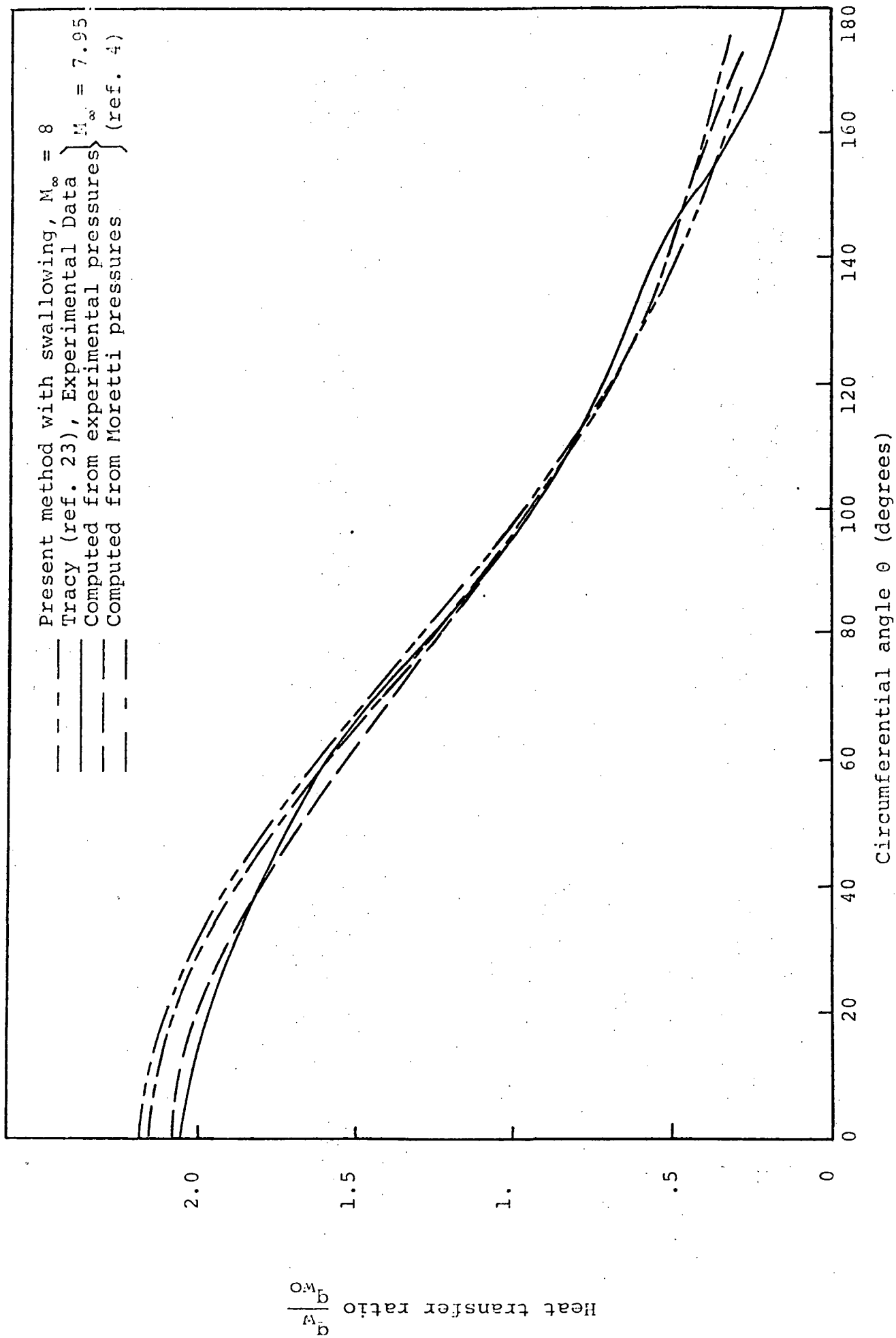


Figure 4.18 Heat transfer distribution on 10° sharp circular cone at $\alpha = 8^\circ$

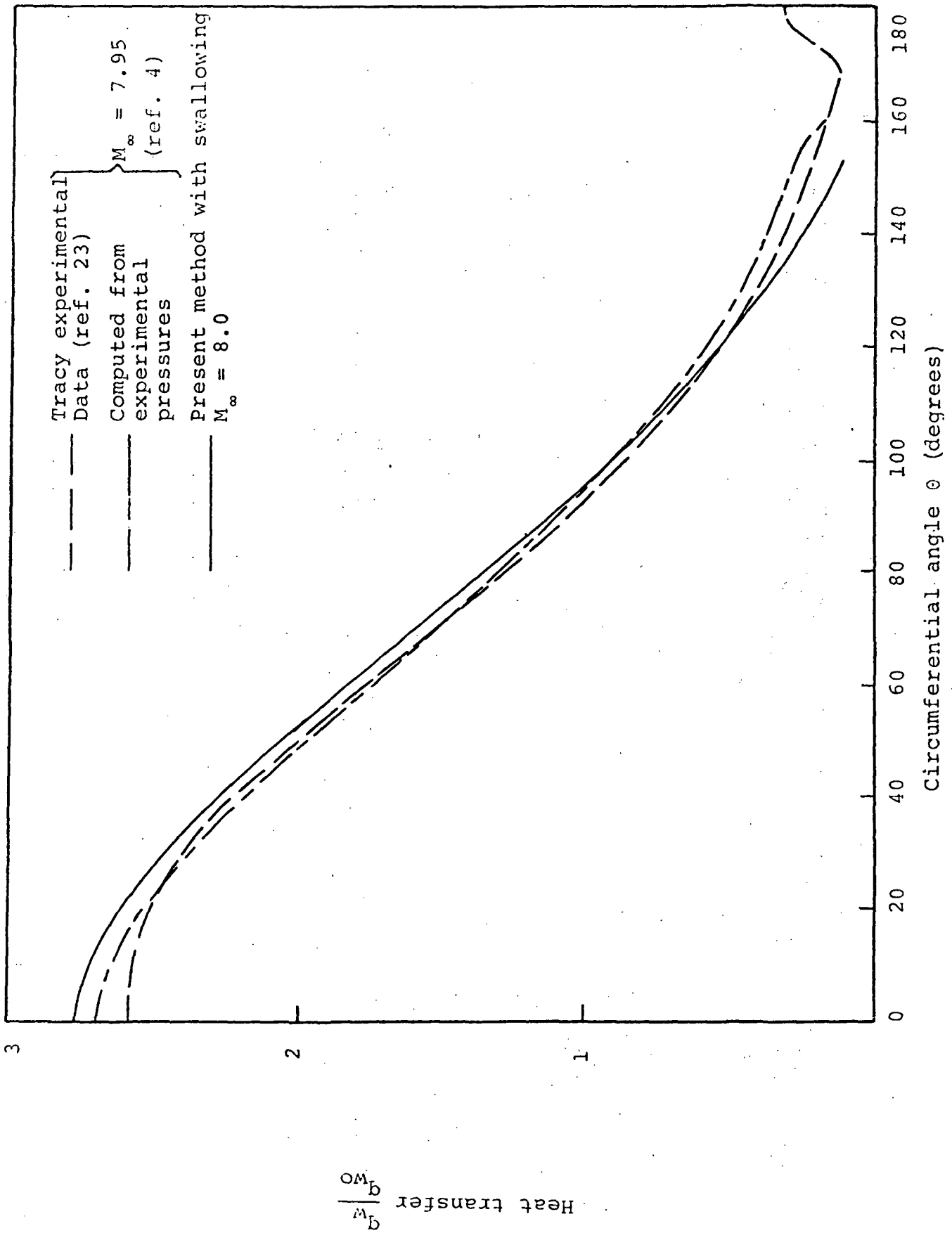


Figure 4.19 Heat transfer distribution on 10° sharp circular cone at $\alpha = 12^\circ$

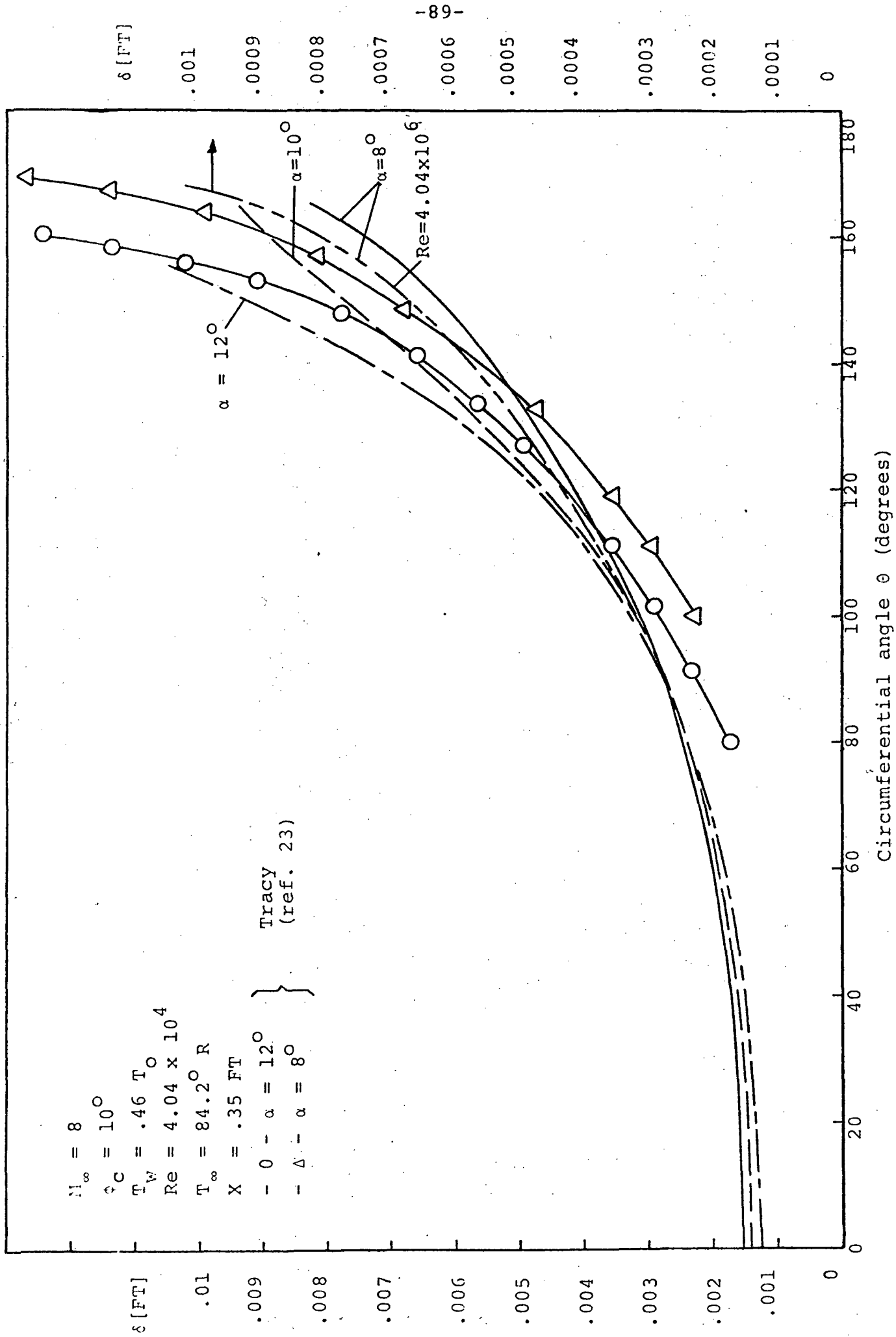


Figure 4.20 Circumferential boundary layer thickness distribution on a sharp circular cone

δ (ft)

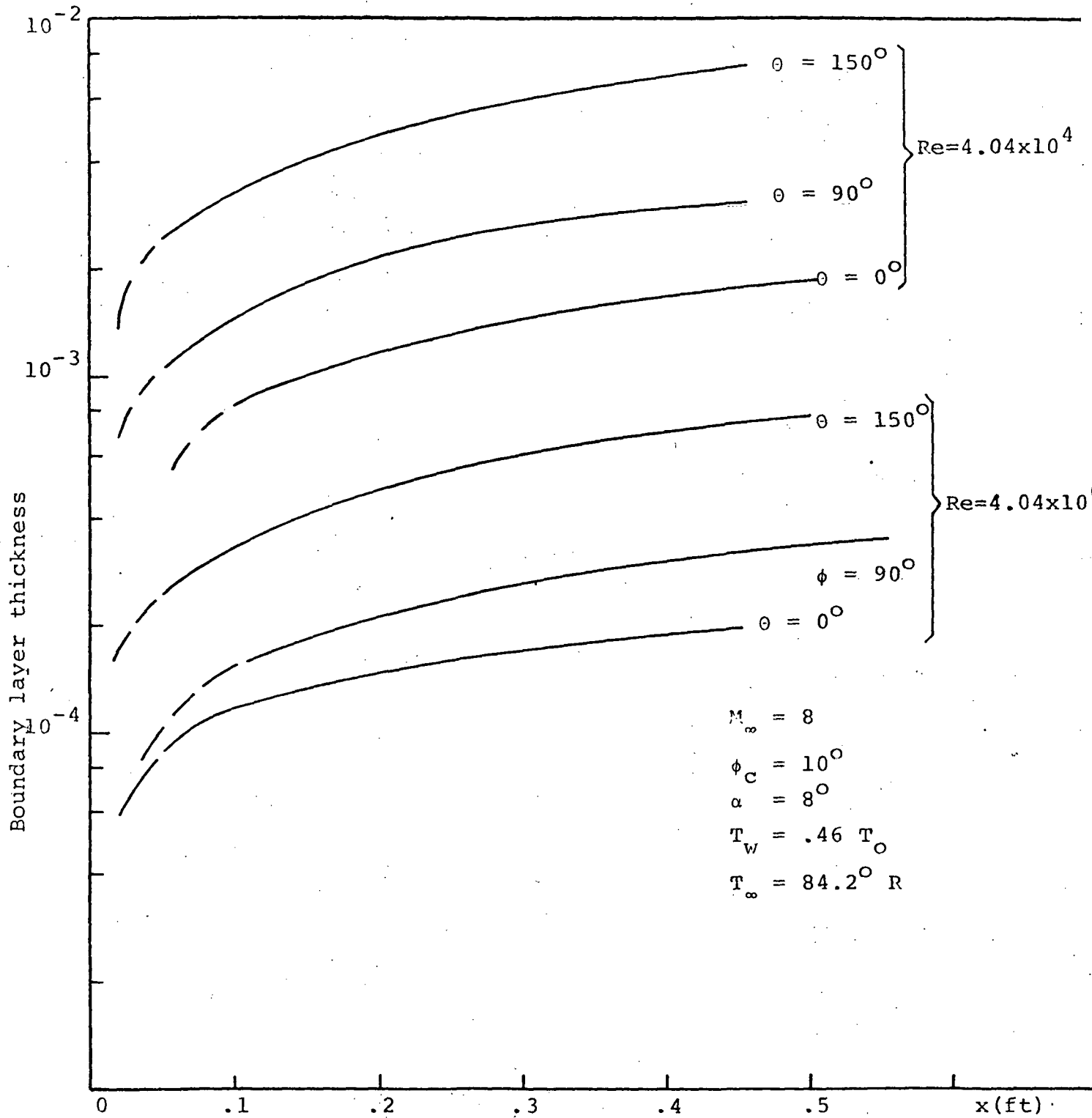


Figure 4.21 Streamwise variation of the boundary layer thickness on a sharp circular cone

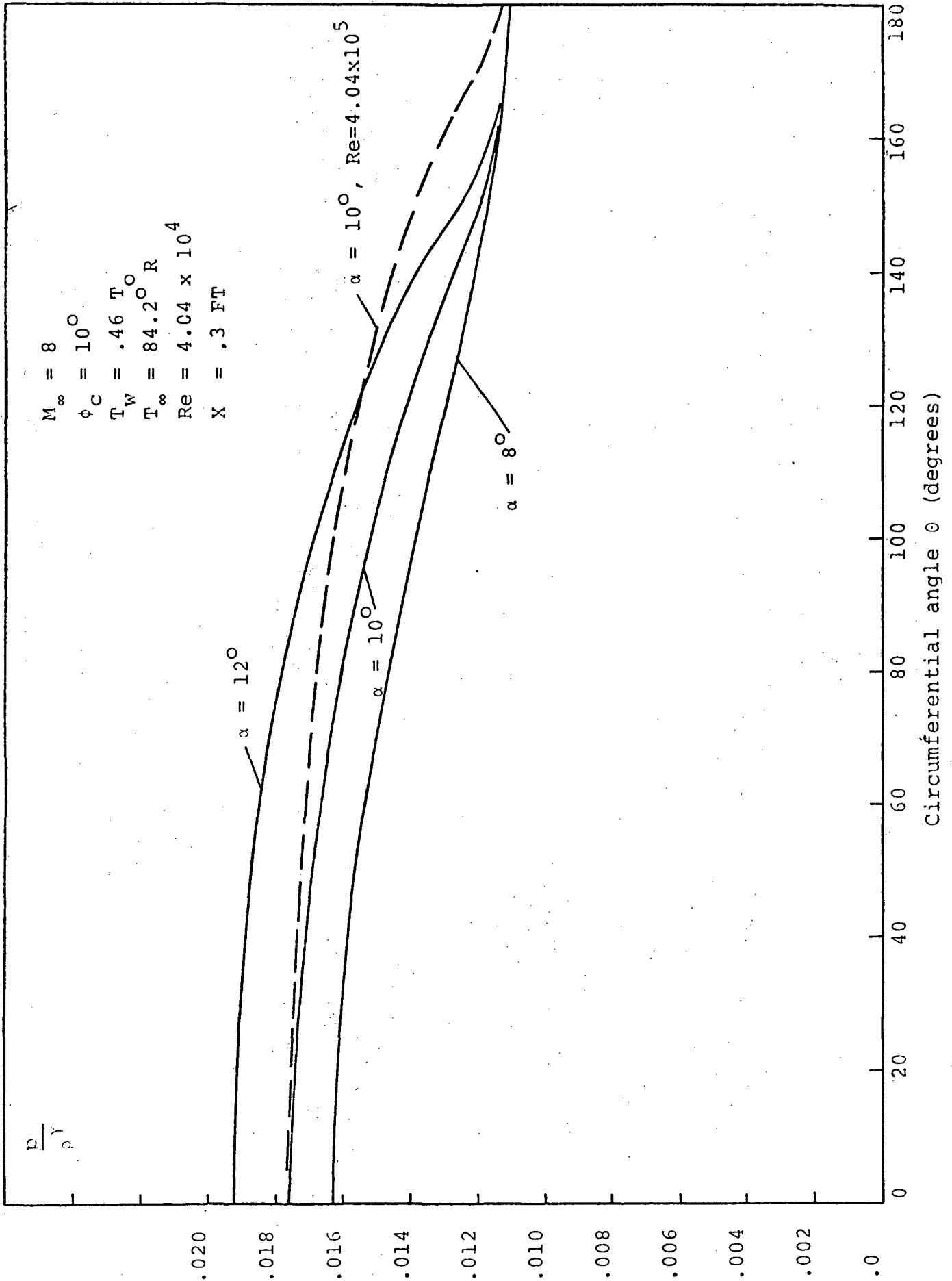


Figure 4.22 Circumferential entropy distribution on a sharp circular cone for the case of entropy swallowing at distance σ

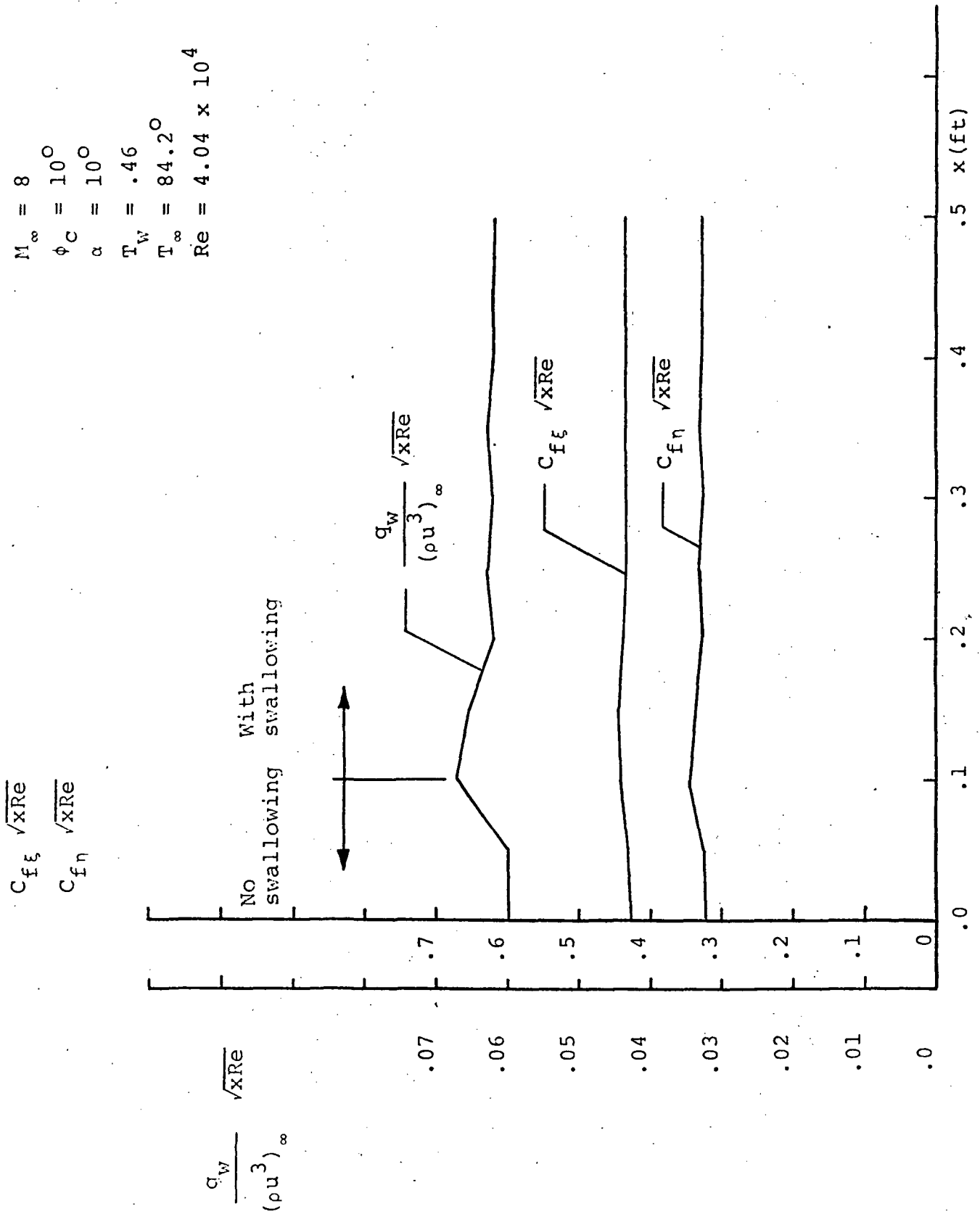


Figure 4.23 Convergence of computed parameters after transfer to entropy swallowing

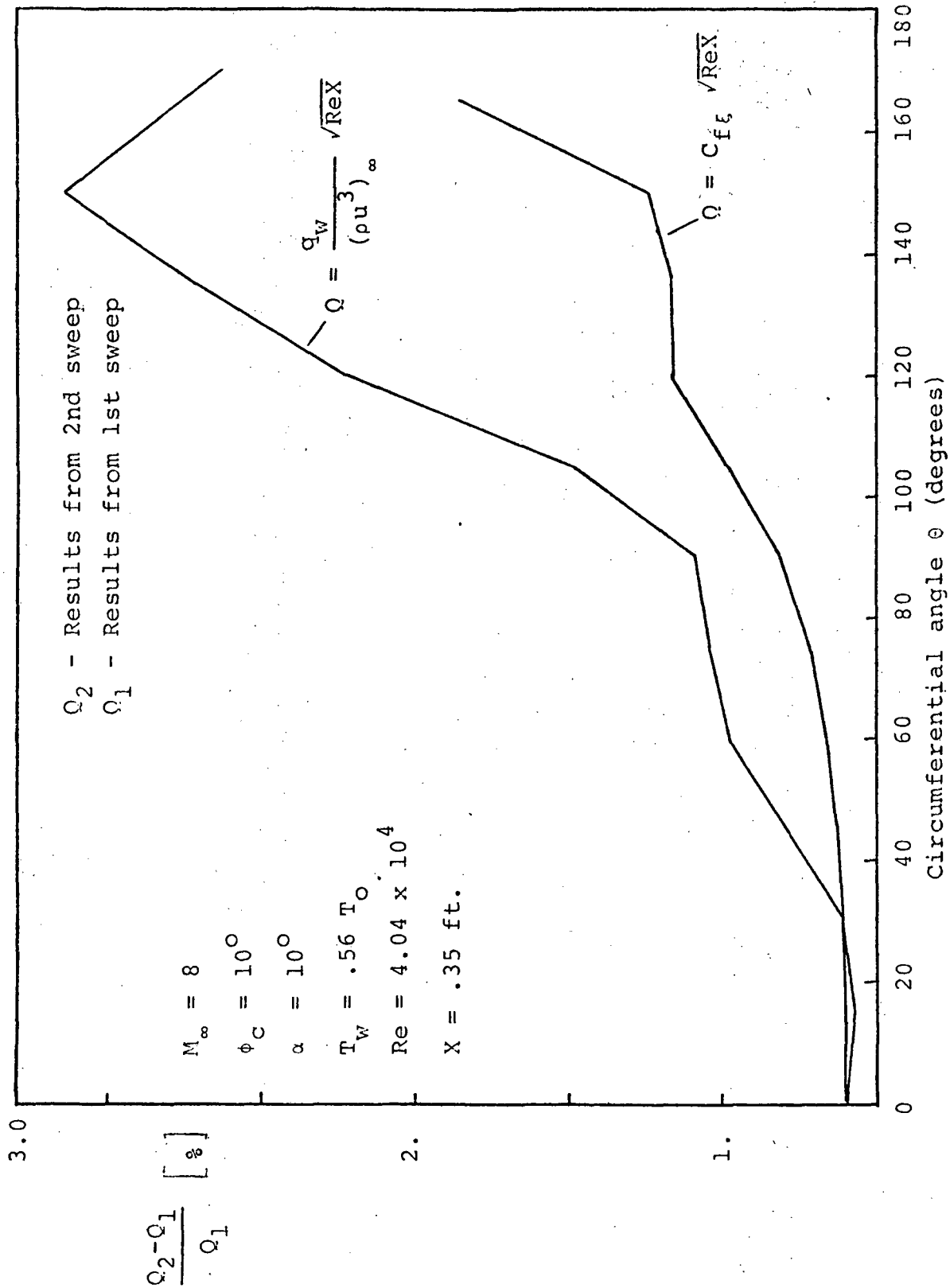


Figure 4.24 Circumferential error distribution between results from 2nd and 1st sweep for a sharp circular cone

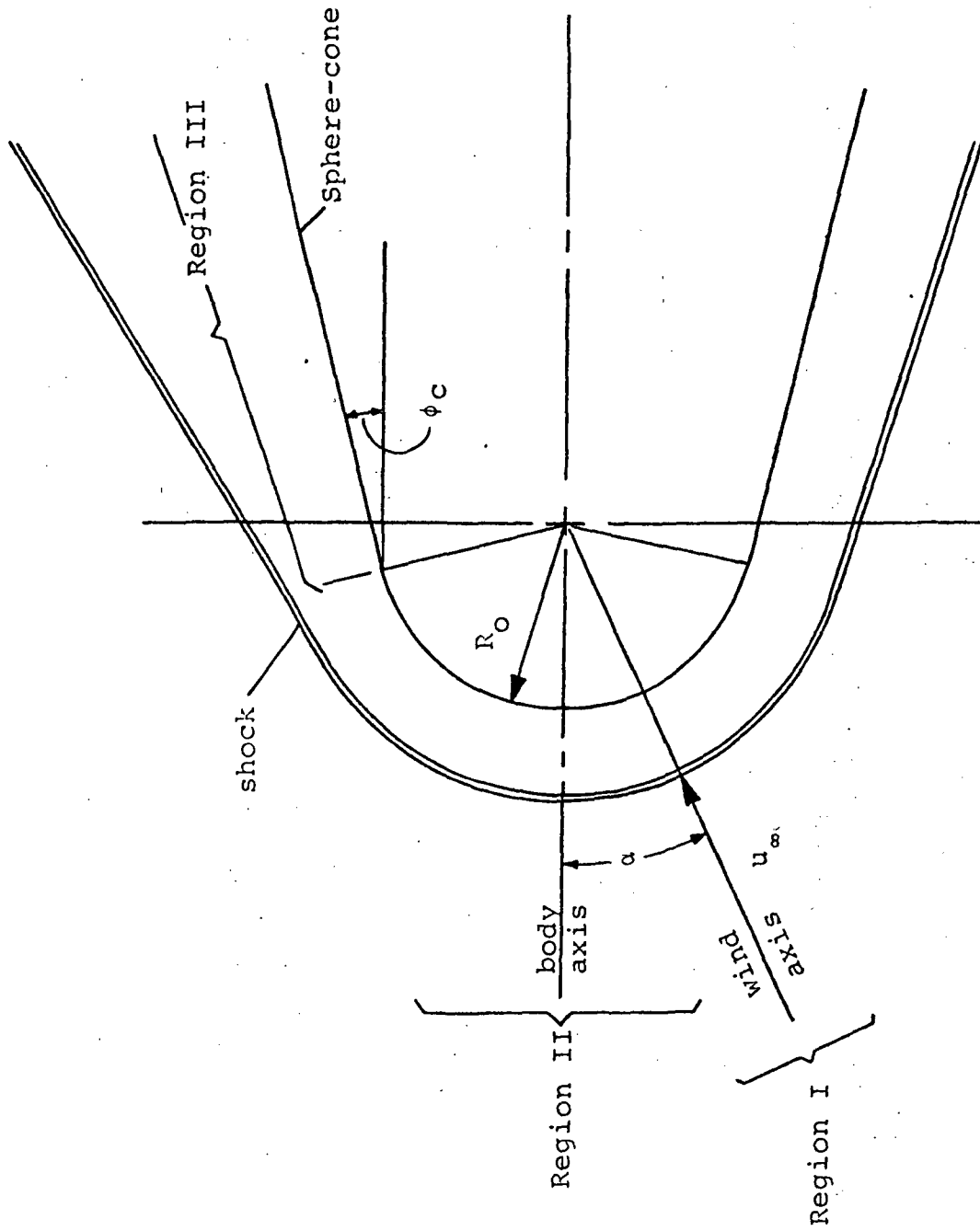
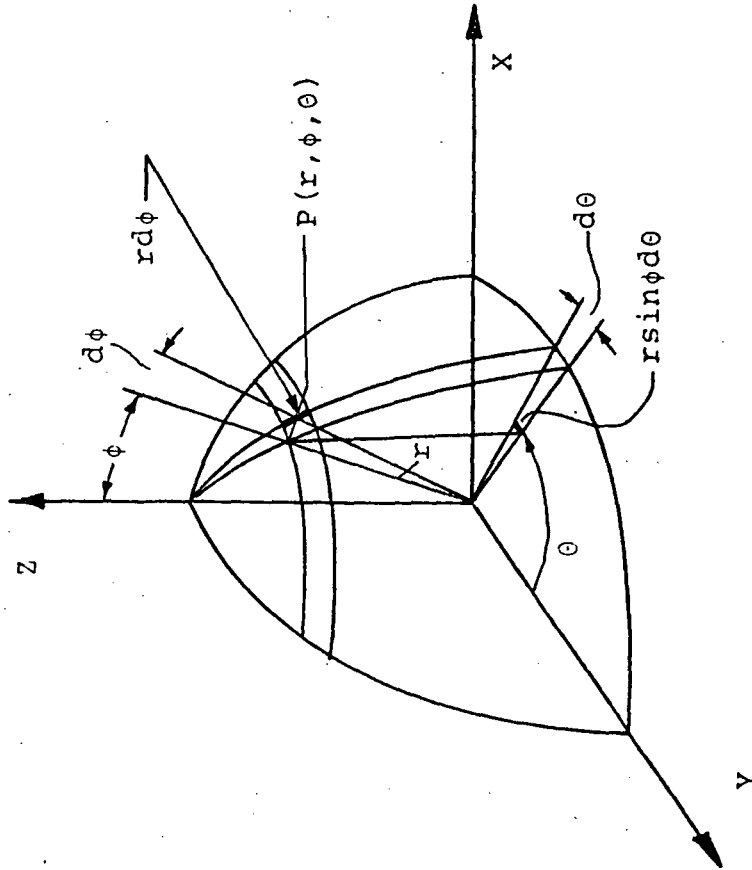


Figure 5.1 Sphere-cone geometry



$$dx^2 = h_1^2 d\xi^2 + h_2^2 d\eta^2 + h_3^2 dz^2$$

$$dx^2 = r^2 d\phi^2 + (r \sin \phi)^2 d\theta^2 + dr^2$$

$$h_1 = r, \quad h_2 = r \sin \phi$$

$$\xi = \phi, \quad \eta = \theta$$

Figure 5.2 Spherical coordinate system

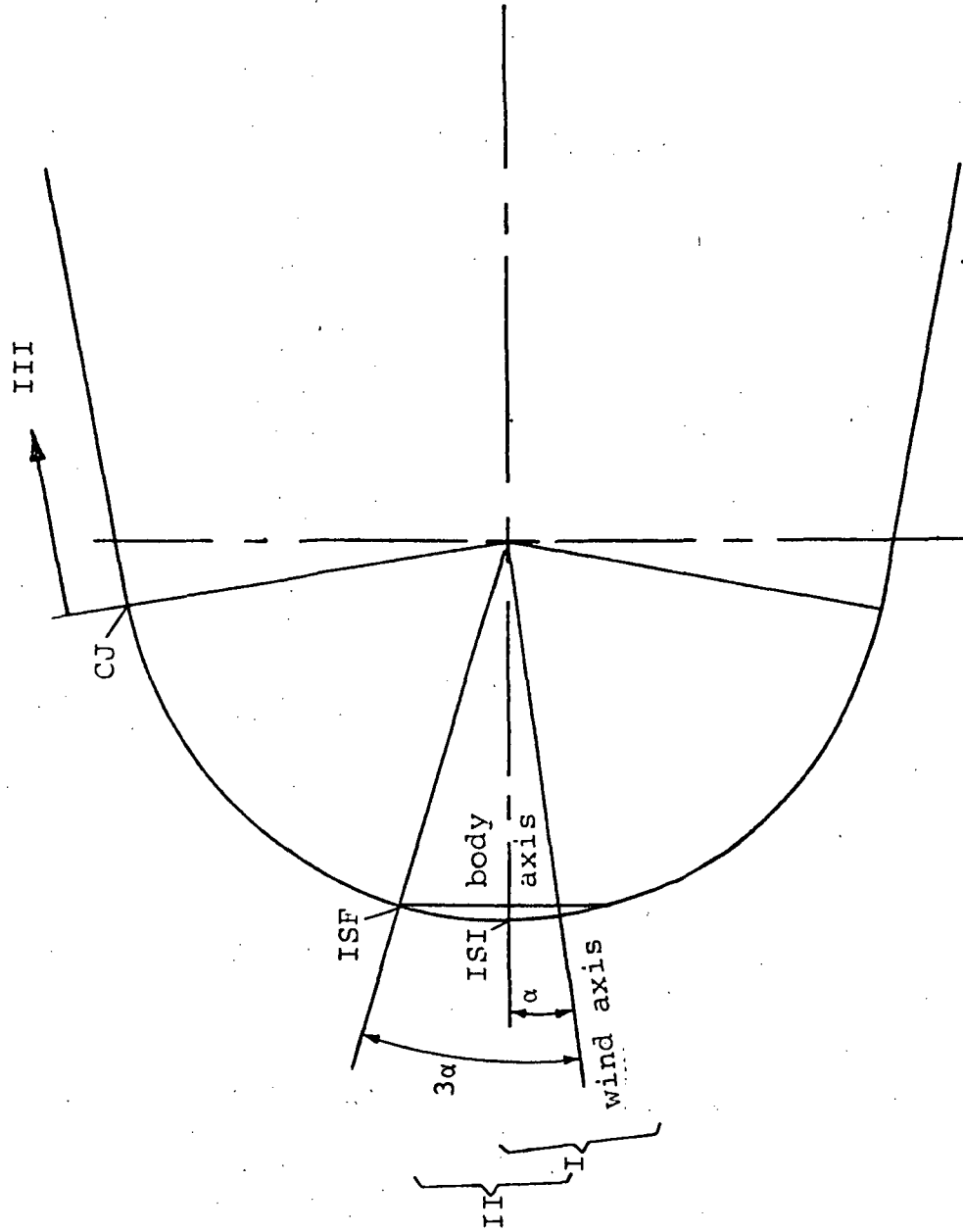


Figure 5.3 Geometry for regions I and II for a sphere

$$\underline{x_K = R_N + (x_O - R_N) \cos \alpha + r_O \sin \alpha \cos \theta}$$

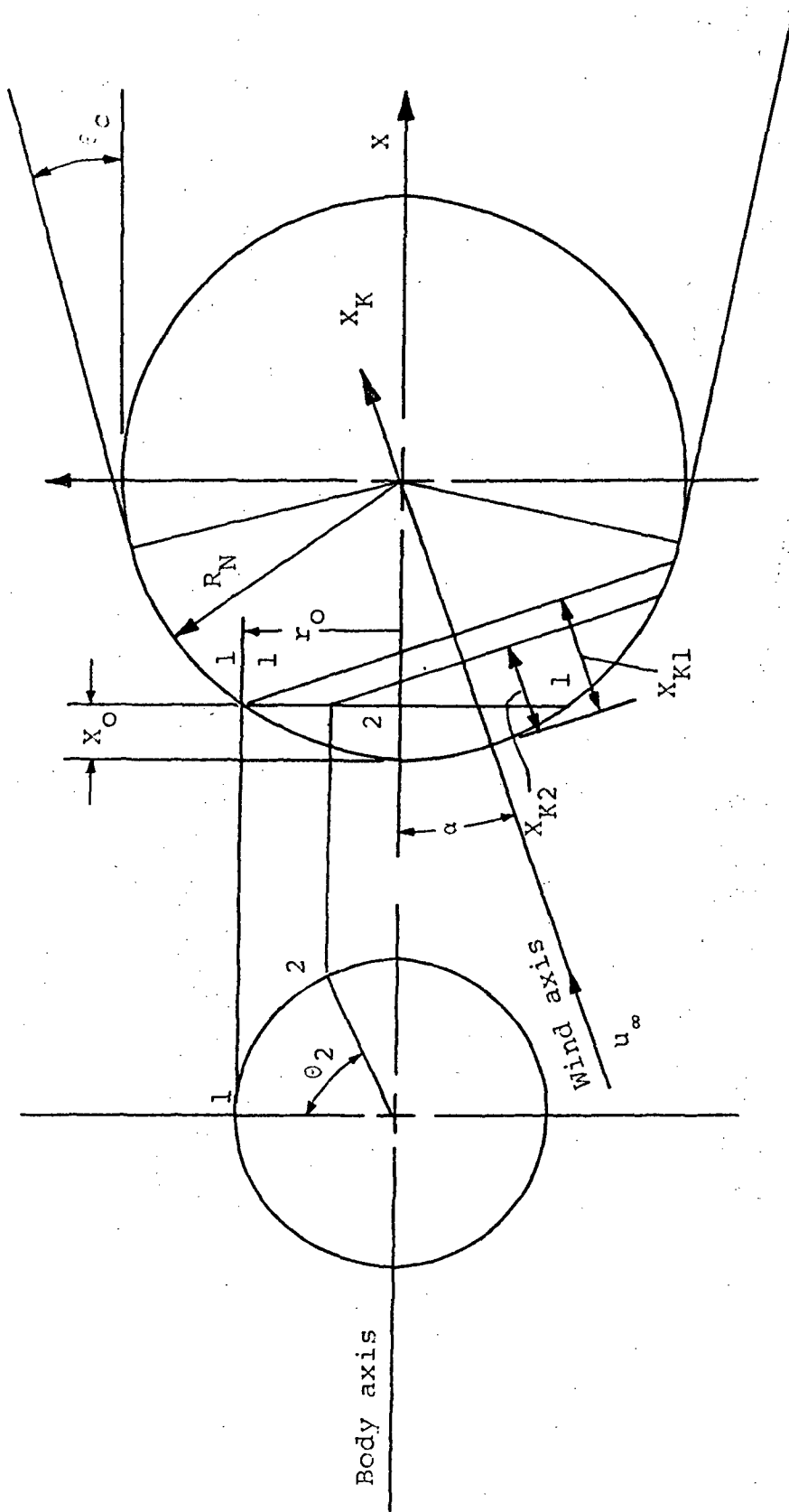


Figure 5.4 Geometrical relations for a sphere in wind and body systems

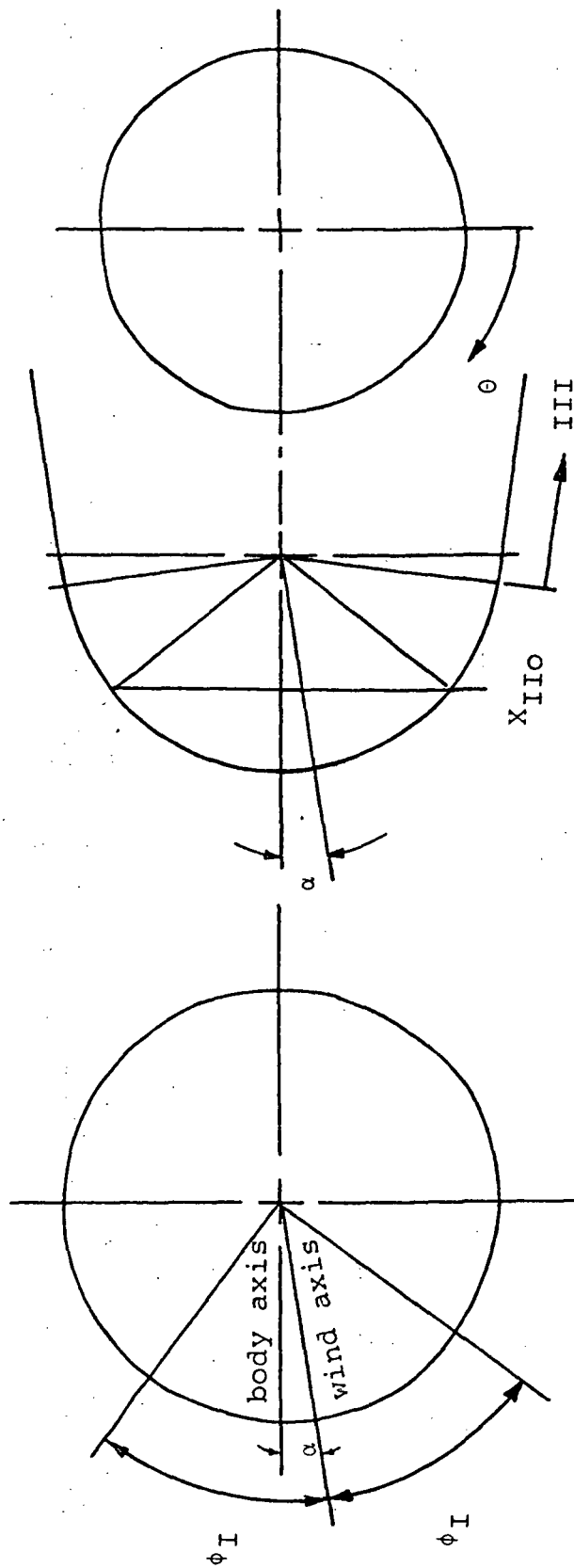


Figure 5.5 Geometry for inviscid data input for region I and II for sphere

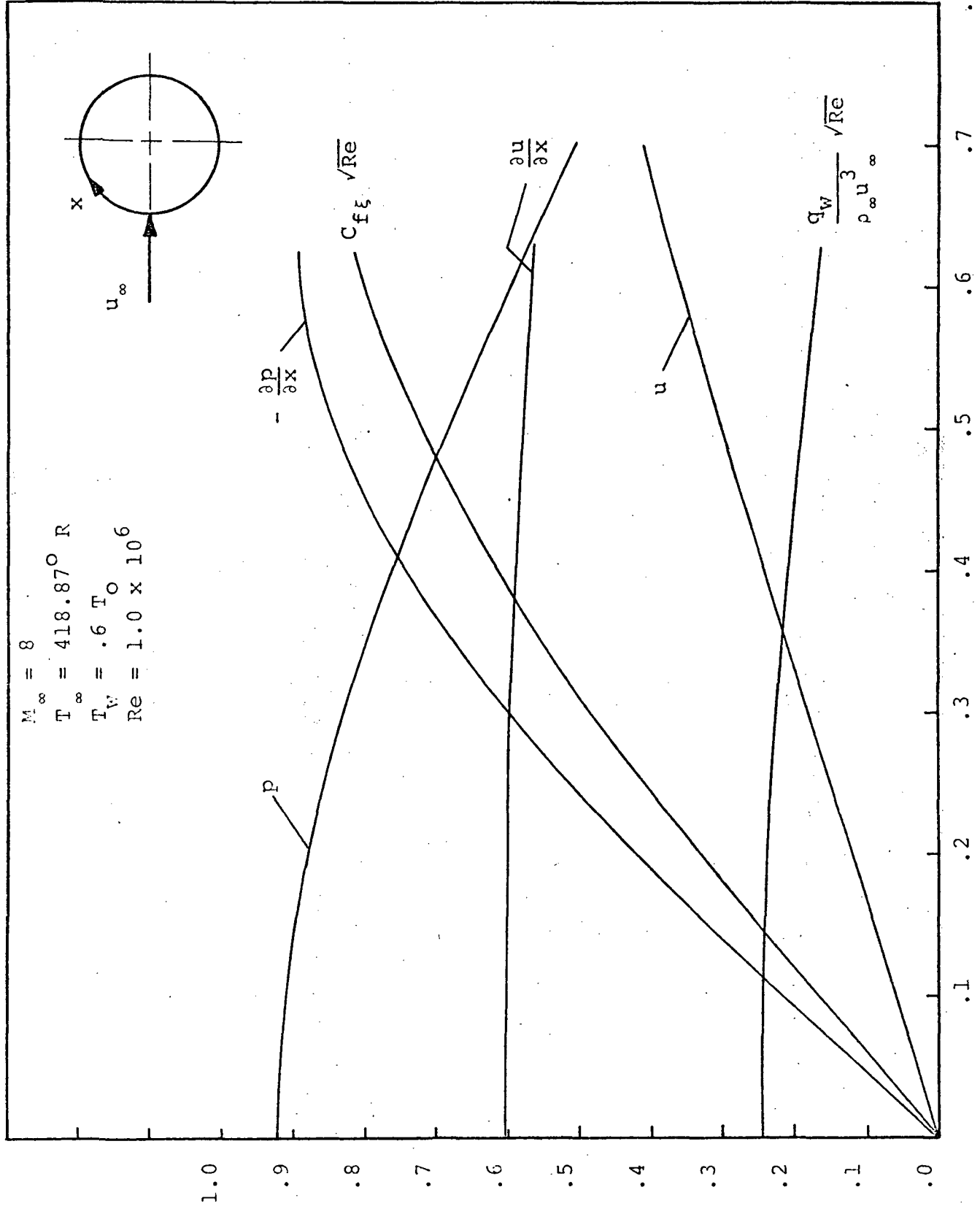


Figure 5.6 Skin friction, heat transfer and flow variables about a sphere

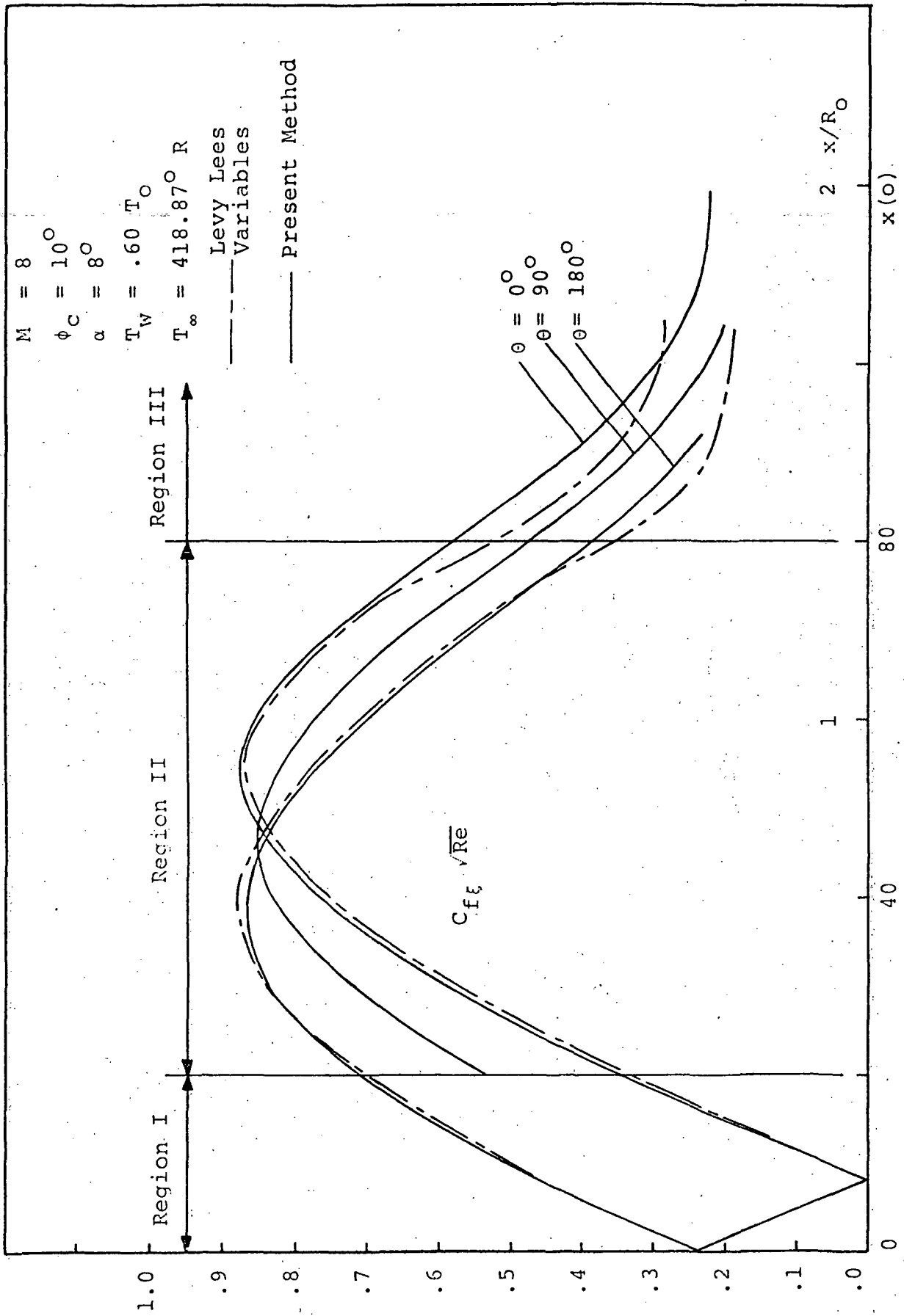


Figure 5.7 Longitudinal skin friction distribution in meridian planes for a sphere cone

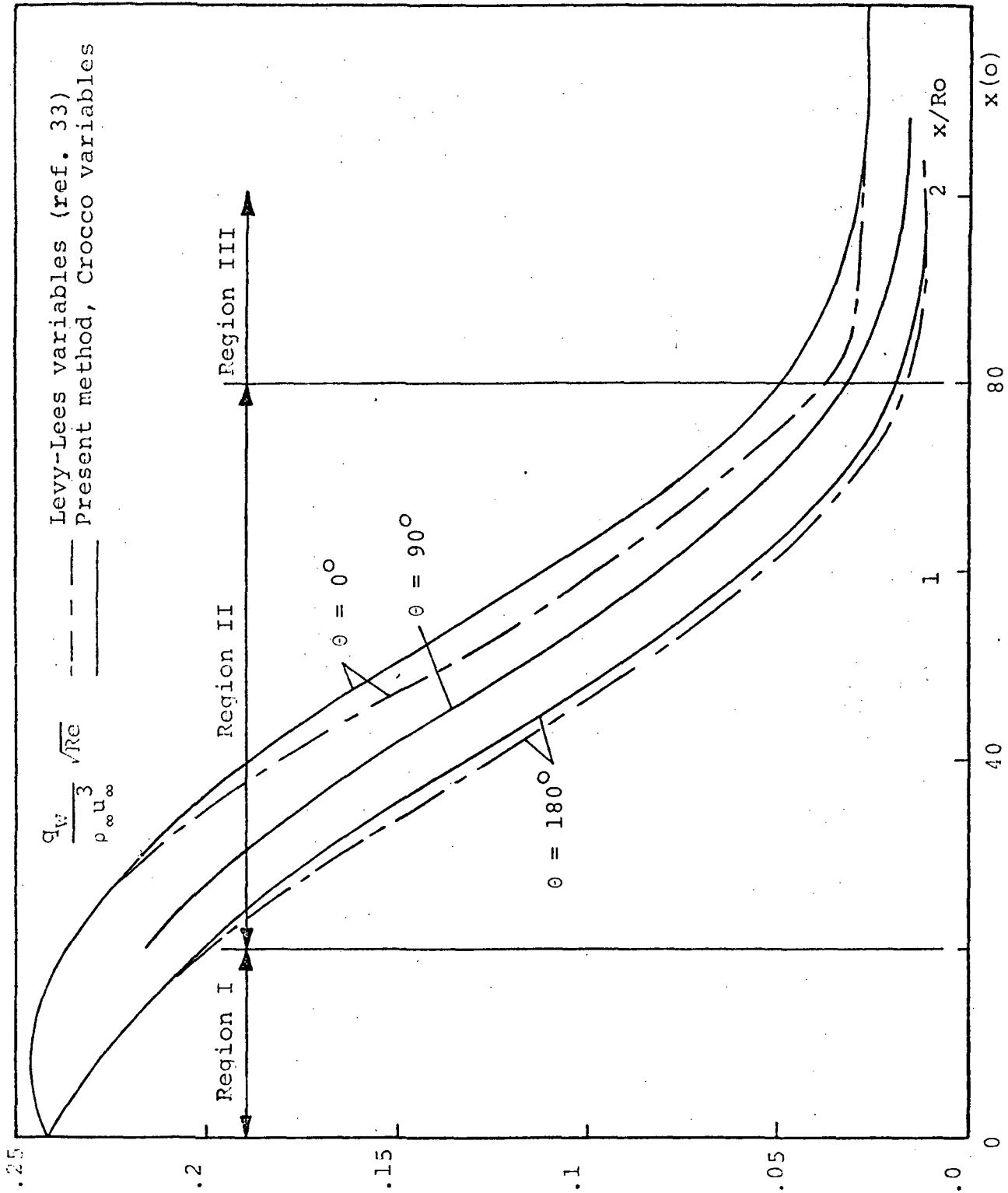


Figure 5.8 Longitudinal heat transfer distribution in meridian planes for a sphere cone

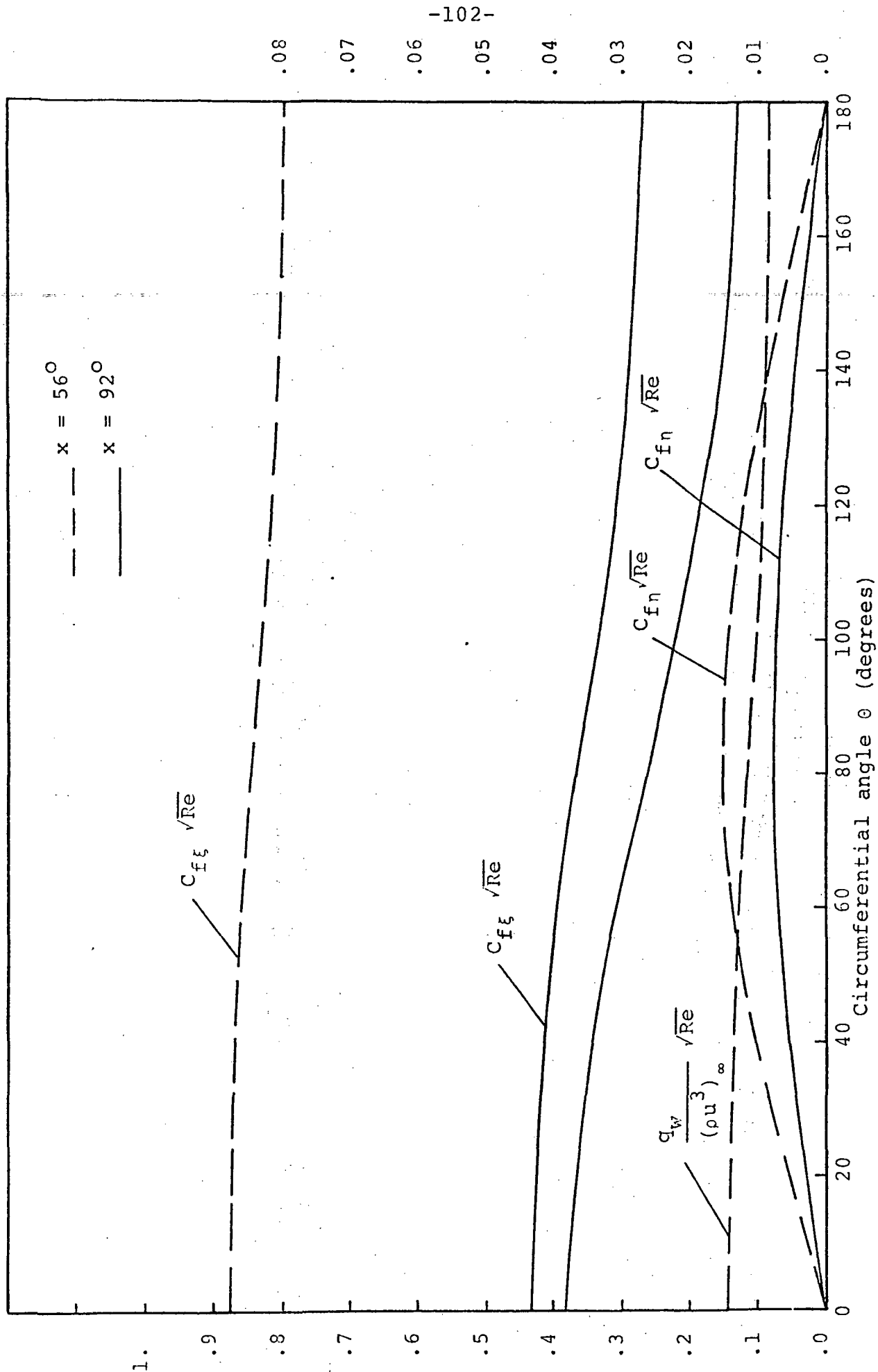


Figure 5.9 Skin friction and heat transfer distribution on a sphere-cone

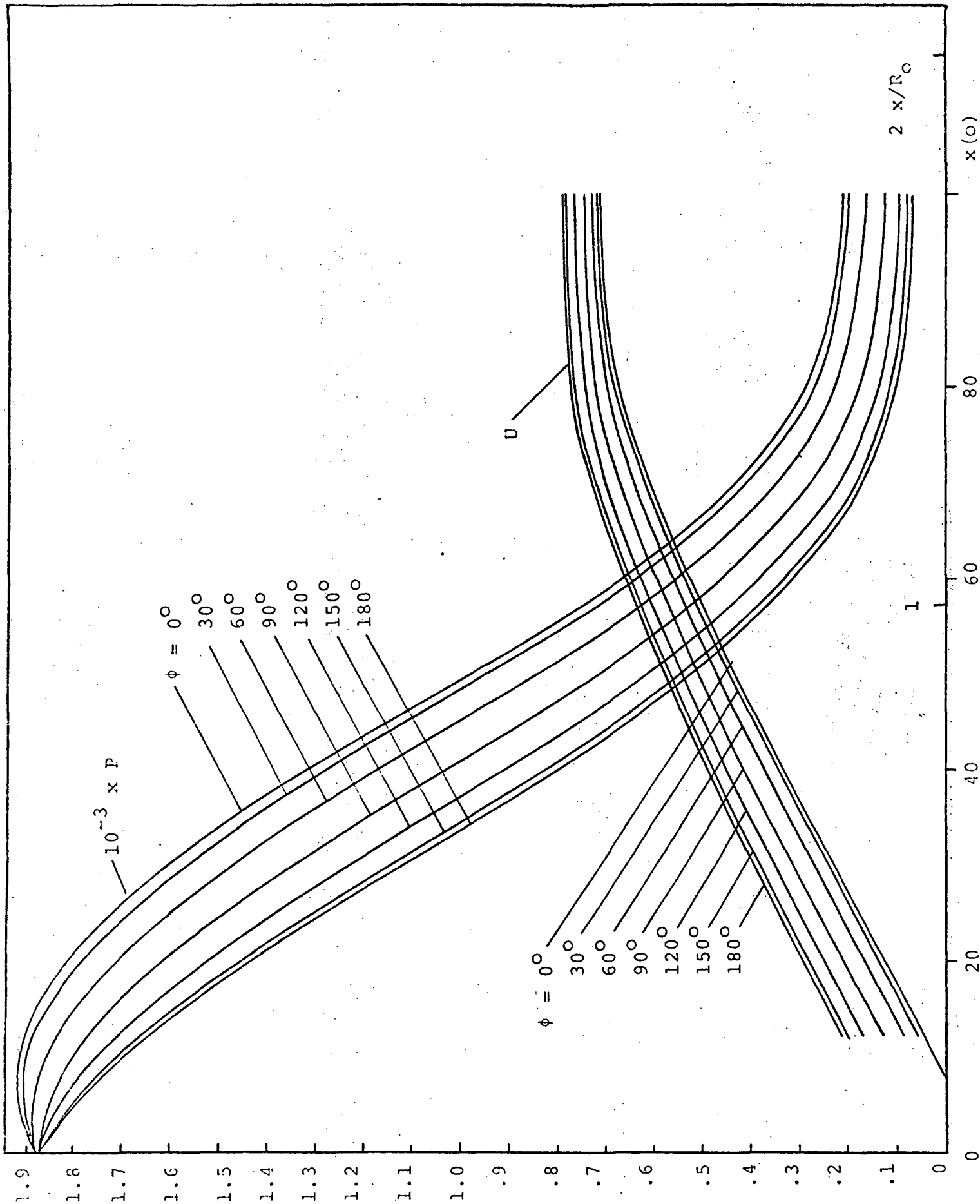
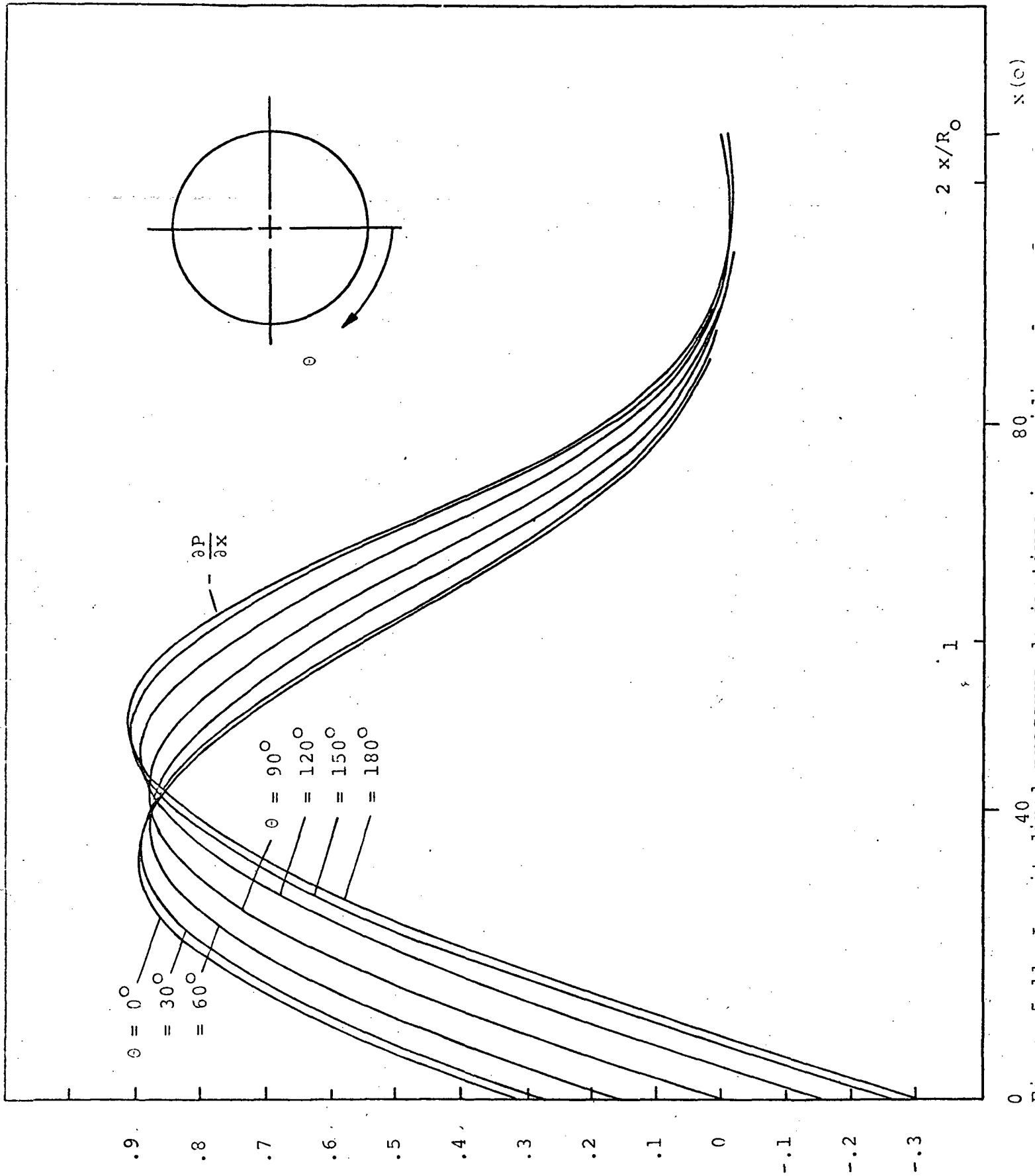


Figure 5.10 Longitudinal pressure and velocity distribution in meridional planes



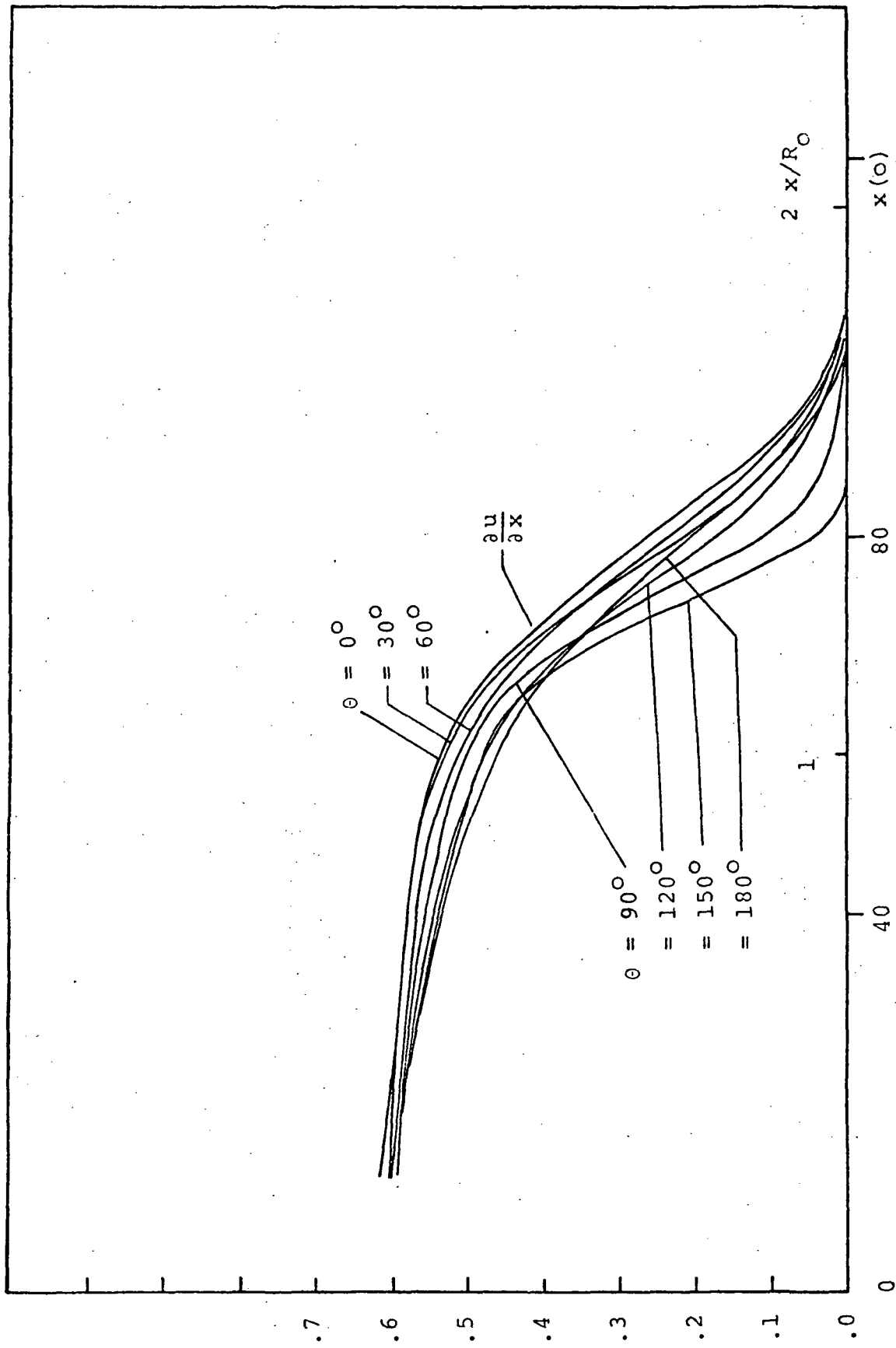


Figure 5.12 Longitudinal velocity derivative in meridian planes for a sphere cone

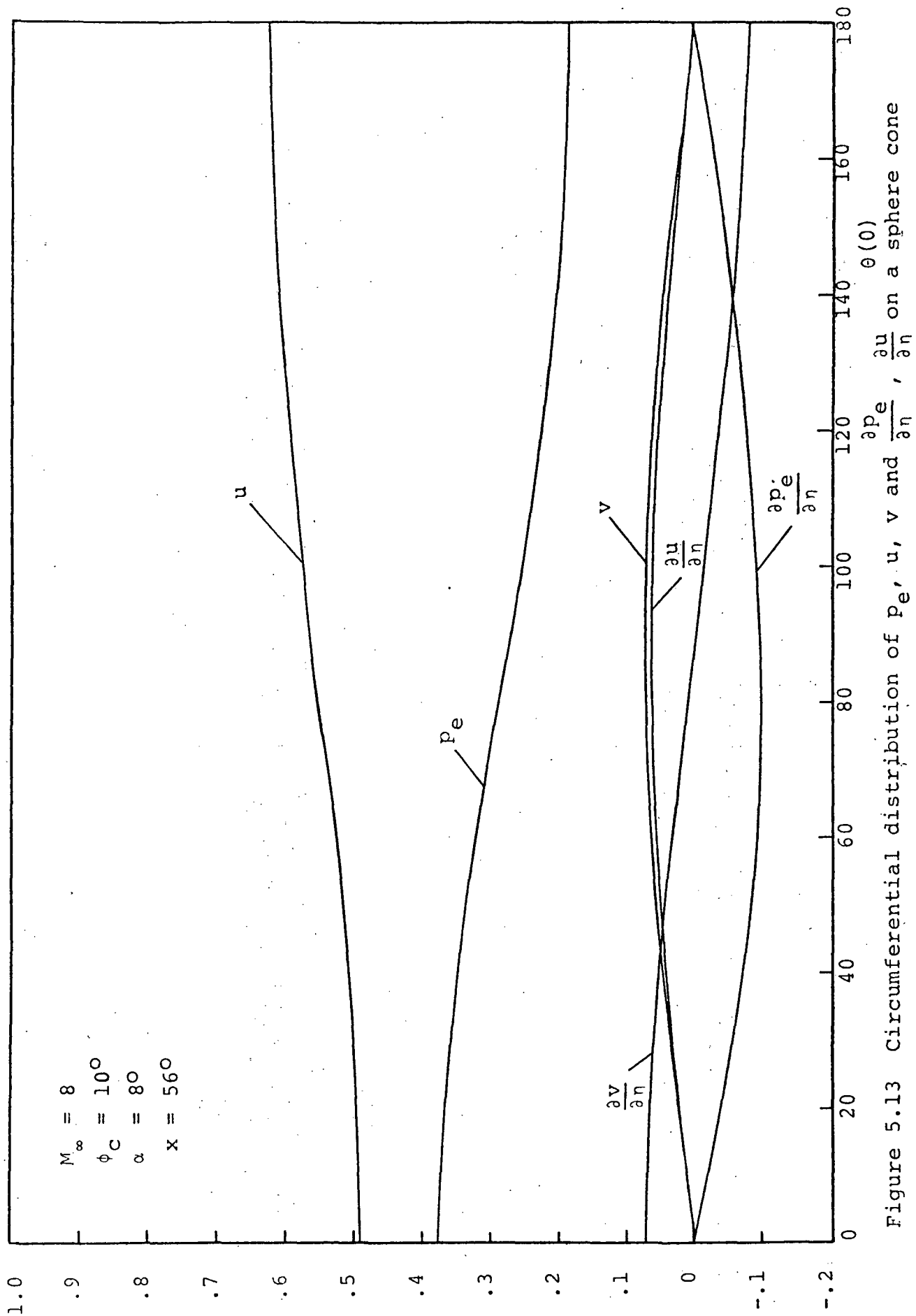


Figure 5.13 Circumferential distribution of p_e , u , v and $\frac{\partial p_e}{\partial \eta}$, $\frac{\partial u}{\partial \eta}$ on a sphere cone

APPENDIX A

Coefficients A_i and B_i

$$A_1 = \frac{\xi^{*2} u_e p_e}{t_e^2}, \quad A_2 = \frac{v_e}{h_2} \xi^{*2} \frac{p_e}{t_e^2}, \quad (A1-A2)$$

$$A_3 = \frac{p_e}{t_e^2} u_e, \quad A_4 = \frac{p_e \xi^{*2}}{2 t_e^2} \frac{\partial u_e}{\partial \xi}, \quad (A3-A4)$$

$$A_5 = \frac{v_e \xi^{*2} p_e}{2 h_2 u_e t_e^2} \frac{\partial u_e}{\partial \eta}, \quad A_6 = \frac{1}{2} \frac{v_e^2 \xi^{*2} p_e}{u_e h_2 t_e^2} \frac{\partial h_2}{\partial \xi}, \quad (A5-A6)$$

$$A_7 = \frac{\xi^{*2}}{2 u_e t_e} \frac{\partial p_e}{\partial \xi}, \quad A_8 = \frac{p_e \xi^{*2} u_e}{t_e^2 v_e h_2} \frac{\partial (v_e h_2)}{\partial \xi}, \quad (A7-A8)$$

$$A_9 = \frac{\xi^{*2} p_e}{t_e^2 h_2} \frac{\partial v_e}{\partial \eta}, \quad A_{10} = \frac{\xi^{*2}}{h_2 v_e t_e} \frac{\partial p_e}{\partial \eta}, \quad (A9-A10)$$

$$A_{11} = \frac{(\gamma-1) u_e \xi^{*2}}{\gamma t_e^2} \frac{\partial p_e}{\partial \xi}, \quad A_{12} = \frac{(\gamma-1) v_e \xi^{*2}}{\gamma h_2 t_e^2} \frac{\partial p_e}{\partial \eta}, \quad (A11-A12)$$

$$A_{13} = \frac{4(\gamma-1) u_e^2}{\gamma t_e}, \quad A_{14} = \frac{(\gamma-1) v_e^2}{\gamma t_e}, \quad (A13-A14)$$

$$A_{15} = \frac{u_e^2 \xi^*}{t_e h_2} \frac{\partial}{\partial \xi} \left[\frac{p_e \xi^* h_2}{t_e u_e} \right], \quad A_{16} = \frac{\xi^* v_e}{t_e h_2} \frac{\partial}{\partial \eta} \left[\frac{p_e \xi^*}{t_e} \right], \quad (A15-A16)$$

$$A_{17} = \frac{p_e \xi^{*2}}{2 t_e^2 h_2} \frac{\partial v_e}{\partial \eta} , \quad A_{18} = \frac{\xi^{*2} u_e p_e}{t_e^3} \frac{\partial t_e}{\partial \xi} , \quad (A17-A18)$$

$$A_{19} = \frac{\xi^{*2} v_e p_e}{h_2 t_e^3} \frac{\partial t_e}{\partial \eta} . \quad (A19)$$

$$B_1 = \frac{-\ell}{\phi^2 \zeta} [A_4 (1-\zeta^2)^2 + A_5 G (1-\zeta^2) - A_6 G^2 + A_7 \theta] , \quad (A20)$$

$$B_2 = \frac{-\ell}{\phi^2} [A_8 (1-\zeta^2) + A_9 G] , \quad (A21)$$

$$B_3 = \frac{-\ell}{\phi^2} A_{10} \theta , \quad (A22)$$

$$B_4 = \frac{-\ell}{\phi^2} A_1 (1-\zeta^2) , \quad (A23)$$

$$B_5 = \frac{-\ell}{\phi^2} A_2 G , \quad (A24)$$

$$B_6 = - \frac{\ell Pr}{\phi^2 \zeta} [A_4 (1-\zeta^2)^2 + A_5 G (1-\zeta^2) - A_6 G^2 + A_7 \theta] , \quad (A25)$$

$$B_7 = \frac{\ell Pr}{\phi^2} [(A_{11} - A_{18}) (1-\zeta^2) + G(A_{12} - A_{19})] , \quad (A26)$$

$$B_8 = \text{Pr} [\zeta^2 A_{13} + A_{14} (\frac{\partial G}{\partial \zeta})^2] ,$$

(A27)

$$B_9 = - \frac{\ell \text{Pr}}{\phi^2} A_1 (1 - \zeta^2) ,$$

(A28)

$$B_{10} = - \frac{\ell \text{Pr}}{\phi^2} A_2 G ,$$

(A29)

$$B_{11} = - \frac{\ell}{\zeta} [A_4 (1 - \zeta^2)^2 + A_5 G (1 - \zeta^2) - A_6 G^2 + A_7 \theta] , \quad (A30)$$

$$B_{12} = - \frac{\ell}{\zeta^2} [A_4 (1 - \zeta^2)^2 + A_5 (1 + \zeta^2) G - A_6 G^2 + A_7 (\theta - \zeta \frac{\partial \theta}{\partial \zeta})] \\ + \ell [(2A_{17} + A_{16}) G + A_{15} (1 - \zeta^2)]$$

$$+ \frac{\ell}{\zeta} [\zeta A_2 \frac{\partial G}{\partial \eta} + [A_5 (1 - \zeta^2) - 2A_6 G] \frac{\partial G}{\partial \zeta}]$$

$$+ \theta \frac{\partial \ell}{\partial t} [A_1 (1 - \zeta^2) \frac{\partial t_e}{\partial \xi} + A_2 G \frac{\partial t_e}{\partial \eta}]$$

$$+ \frac{t_e}{\zeta} \frac{\partial \ell}{\partial t} [A_1 \zeta (1 - \zeta^2) \frac{\partial \theta}{\partial \xi} + A_2 G \frac{\partial \theta}{\partial \eta}]$$

$$+ [A_4 (1 - \zeta^2)^2 + A_5 (1 - \zeta^2) G - A_6 G^2 + A_7 \theta] \frac{\partial \theta}{\partial \zeta} , \quad (A31)$$

$$B_{13} = -2A_1(1-\zeta^2) ,$$

(A32)

and

$$B_{14} = -2A_2G .$$

(A33)